

Properties and dynamics of two-dimensional colloid-polymer mixtures

Michael Adrian Mordan

Christ Church
University of Oxford

Supervisors: Prof. Dirk G. A. L. Aarts and
Prof. Roel. P. A. Dullens

A thesis submitted for the degree of
Doctor of Philosophy

Hilary Term 2019

Abstract

The depletion interaction, aggregation behaviour and network formation in quasi-two-dimensional colloid-polymer solutions are studied using optical microscopy and optical tweezing. First, the polymer used as a depletant throughout this thesis, xanthan gum, is characterised. The intrinsic viscosity, coil overlap concentration and radius of gyration are determined using a novel combination of passive micro-rheology and polyelectrolyte rheology theory. The Mark-Houwink coefficient is also found, which can be used to characterise the molecular weight of future xanthan samples, under the experimental condition described herein. Next, the depletion interaction between two superparamagnetic particles, near to a wall, is measured using a combination of optical tweezer microscopy, statistical analysis and first passage time theory. The interaction strength is measured for two concentrations of polymer in the dilute regime and one in the semi-dilute regime. Due to the particles' superparamagnetic nature, their response to an applied magnetic field is used to probe the semi-dilute regime which would not be possible by passive methods alone. Having characterised the interparticle attraction range and strength, the two-dimensional aggregation behaviour of the same colloid-polymer system is investigated, at three successively increasing concentrations and analysed using established aggregation theory. Past a polymer concentration threshold, the strength of interaction is found to have no measurable effect on the systems aggregation kinetics. Finally, the network formation as a function of polymer concentration is analysed. The network strand thickness and coordination number distributions are found to have a strong dependence on the interparticle interaction strength. The structural dynamics and network coarsening behaviour pre and post network formation is also shown to depend strongly on the polymer concentration. Cluster and network dynamics are quantified using bond-order orientational analysis which shows a competition between inter-cluster particle rearrangements and cluster aggregation at low polymer concentrations that are significantly diminished at higher polymer concentrations.

Declaration

This thesis is submitted for the degree of Doctor of Philosophy in Physical and Theoretical Chemistry at the University of Oxford. No part of this thesis has been accepted or is currently being submitted for any degree, diploma, certificate or other qualification in this University or elsewhere. This thesis is wholly my own work, except where indicated.

Contents

Abstract **i**

Declaration **iii**

1 General introduction **1**

1.1 Introduction 1

1.1.1 Agrochemicals and formulation stability 2

1.1.2 Colloidal model systems 3

1.1.3 Scope of this thesis 4

2 Theoretical background and experimental methods **7**

2.1 Physics of colloidal systems 8

2.1.1 Characteristic length and times scales 8

2.1.2 Interparticle interactions 9

2.1.3 Stability of colloid-polymer mixtures 12

2.1.4 Colloid-polymer mixtures and their arrested states 16

2.2 Methods 19

2.2.1 Two-dimensional model systems 19

2.2.2 Video microscopy 21

2.2.3 Image analysis 21

2.2.4 Optical trapping 21

3 Polymer characterisation via passive microrheology 25

3.1 Introduction 26

3.2 Theory 27

3.2.1 Viscosity, rheology and mean squared displacement 27

3.3 Experimental method 31

3.4 Results and discussion 32

3.5 Conclusions 39

4 Measuring the pair potentials in colloid-polymer solutions 41

4.1 Introduction 42

4.2 Theory 43

4.3 Experimental method 48

4.3.1 Sample preparation 49

4.3.2 Magnetic susceptibility 49

4.3.3 Determination of Brownian time 50

4.3.4 Optical tweezing setup 51

4.3.5 Experimental protocol 52

4.3.6 Image analysis 53

4.4 Results and discussion 54

4.4.1 Separation and diffusion without an applied magnetic field 55

4.4.2 Separation and diffusion with an applied magnetic field 59

4.5 Conclusions 62

5 Cluster formation in quasi-2D colloid-polymer systems 63

5.1 Introduction 64

5.2 Theory 66

5.2.1 Cluster growth 67

5.2.2 Fractal dimension analysis 67

5.2.3 Coordination number theory 68
5.3 Experimental method 70
5.3.1 Sample preparation 70
5.3.2 Cluster identification and coordination number tracking 70
5.4 Results and discussion 71
5.4.1 Cluster growth analysis 72
5.4.2 Fractal dimension analysis 74
5.4.3 Coordination number analysis 76
5.5 Conclusions 78

6 Formation and evolution of networks in quasi-2D colloid-polymer mixtures 81

6.1 Introduction 82
6.2 Experimental method 84
6.2.1 Sample preparation 84
6.2.2 Cluster growth and network formation analysis 84
6.2.3 Bond-orientational order analysis 85
6.3 Results and discussion 86
6.3.1 Cluster growth and network formation analysis 87
6.3.2 Coordination number analysis 91
6.3.3 Bond-order orientational cluster analysis 93
6.4 Conclusions 97

Acknowledgements 111

Chapter 1

General introduction

1.1 Introduction

The Levant region, today better known as the nations of Syria, Israel, Jordan and Turkey, is widely recognised as the birthplace of agriculture and specifically, plant domestication [1]. Around 10,000 years ago a fundamental shift in human behaviour, from hunter gathering to rudimentary farming, enabled the generation of surplus food supplies and establishment of large settlements. Einkorn wheat, emmer wheat, barley, lentil, pea, bitter vetch and chickpeas are considered to be the seven Neolithic founder crops [1]. Only later, with the Columbian exchange [2], did the familiar western staples of potato and maize as well as many familiar fruits, emerge. However, as the inevitable growth in global population size ensued, pressure on improving crop cultivation techniques to produce ever greater yields arose.

Since these early times, numerous advancements in agricultural techniques have led to subsequent increases in crop yields. A notorious example of human ingenuity in overcoming these problems comes from the late Nobel laureate, Norman Borlaug, and the so-called Green Revolution [3–5]. His work led to the development of high-yield, disease resistant wheat varieties, synonymously known as semi-dwarf wheat [6, 7]. The combination of what was, in essence, genetic engineering and early 20th century chemistry, courtesy of another Nobel laureate Fritz Haber [8], resulted in Mexico reversing from a net importer to net exporter of wheat in 1963 [9]. These innovations also had a profound effect on India and Pakistan, both of which almost

doubled their wheat yields after adopting the same farming methods [9]. However, manipulation of plant genetics by hybridisation methods and enhancement of soil nitrogen content alone are only part of a greater picture. Historically, pest control has been an important ongoing battle in maintaining and improving crop yields.

Pesticides are substances used to control or mitigate the effects of pests and is an umbrella term which includes the subsets of herbicides, insecticides and fungicides. Usually, they contain both active ingredients (AIs), which neutralise the pests, and inert ingredients, which improve the performance and usability of the overall product [10]. Whilst contentious, evidence suggests a cessation of their use would drop global crop yields by a significant amount [11–14]. Therefore, they an important part of modern day farming and critical to sustaining global food and population levels as they currently stand [15]. Whilst some active ingredients can be dissolved or emulsified in solution, many remain solid at ambient temperatures and pressures, even when introduced to an aqueous medium. Modern, large scale production of AIs, through the processes of emulsification, encapsulation and milling, often result in the formation of particles, which have a dimensionality on the order of nanometres to micrometers. However, these particles frequently need to be suspended in solution to enable processing, transport, storage and eventual application. This work was sponsored by a leading crop protection and seed manufacturing company. Therefore, the stability and aggregation behaviour of particulate matter in their products and formulations underpins the motivation for conducting this research. However, the topics covered throughout this thesis are of general concern and applicable in many other commercial and industrial sectors as well.

1.1.1 Agrochemicals and formulation stability

The reliable dispersion of AIs in solution can be a challenge in its own right. A density miss matches between particles and the medium they are dispersed in can result in creaming, where particles rise the surface or sedimentation, where they drop to the bottom. Interparticle stabilisation can also be a problem. Flocculation and aggregation of individual particles is not uncommon [16]. To combat these issues, surfactants and thickening agents are frequently used to aid in particle dispersion, stop uncontrolled aggregation and maintain particle suspension whilst avoiding Stokes settling.

In the context of agrochemicals, these mixtures are referred to as formulations and are used to process, transport and store AIs, often for extended periods of time [17]. However, the behaviour of each formulation is governed by the properties of the specific AIs in question, including their surface chemistry, surface charge, density and particle size. Particle size distribution is also a consideration. Two thickening agents commonly used for industrial applications are xanthan gum [18], a naturally occurring anionic polysaccharide [19], and bentonite clay. This thesis is concerned with the former.

When particles, surfactants and polymers are all present at the same time, understanding the interplay between them is critical to predicting and controlling the overall behaviour and stability of the formulation. Whilst the addition of a thickener, like xanthan gum, undoubtedly slows the dynamics of these systems, additional effects also need to be taken into account. The addition of xanthan is known to aid in the suppression of Stokes settling [20, 21] and can also result in the formation of particle gels [17, 22]. However, xanthan alone in aqueous solutions is not considered to form a gel [23]; some argue it can form a weak gel [24, 25], but only upon the addition of secondary component can a strong gel be formed [26]. If xanthan is added and does not adsorb to particle surfaces, an attractive interaction known as the depletion interaction can occur, resulting in the phase separation of particles into colloid rich and colloid poor phases [27]. However, in some circumstances, this process can be arrested and the formation of two continuous phases occurs, resulting in a meta stable state often classified as a gel. The formation of a gel can lead to overall stabilisation of a formulation which in turn negates the various problems outlined above. An important aspect of this process is particle aggregation and network formation.

1.1.2 Colloidal model systems

Whilst many formulations are colloidal systems in their own right, they are often complicated mixtures consisting of multiple components [17]. Therefore, understanding the fundamentals behind their behaviour is a daunting prospect. One paradigm for simplifying their study is the bottom up approach. By using model colloidal systems, which are well characterised, controllable and understood, individual components of their commercial counterparts, like surfactants and thickeners, can be systematically investigated in isolation. The knowledge gained from this approach can be built upon by the subsequent controlled addition of more components and

further experimentation.

Colloids are defined by a length scale. When discontinuous matter with at least one dimension between 10 nm and 10 μm is dispersed in a medium, be it liquid or gas, its behaviour is governed by effects of thermal energy [28]. For colloidal particles in a fluid, this manifests itself as observable Brownian motion, as particles are randomly bombarded by solvent molecules [29,30]. As a result, particles move though real space in a stochastic manner, whilst simultaneously exploring phase space. Model colloidal particles of different shapes [36–39] can be synthesised from a range of materials [31–35]. Their surface chemistry and dispersing mediums can be altered to generate a multitude of tunable interparticle interactions [16, 40–42]. Many can be manipulated in-situ, providing their optical properties allow [43], by means of optical tweezers. Some are responsive to applied magnetic fields [44–46], allowing control of their association and dissociation at will [47].

Many model colloid systems have already been used to investigate the phenomena of phase separation, gel formation and particle aggregation. However, much of this work has concentrated on the implementation and study of three-dimensional (3D) model systems [48, 49]. In comparison, limited experimental work has been conducted on network formation and gelation in two-dimensions (2D). These have predominately considered 2D aggregation and network formation at an interface [50–53] and has focused on interactions other than colloid-polymer depletion interactions.

1.1.3 Scope of this thesis

In this thesis, the aggregation, dynamics and evolution of quasi-two-dimensional colloid-polymer mixtures is investigated using superparamagnetic particles, xanthan gum and optical video-microscopy. Colloidal particles are confined to a monolayer by the effects of gravity and explore 2D space due to Brownian motion. Aggregation is induced by the presence of polymer, which is used to generate a tunable depletion interaction. The strength of this interaction is dependent on the concentration of polymer present in solution. Particles can also be separated with the application of a suitable magnetic field. Using this model system, the xanthan is characterised using passive micro-rheology. Following on from this, the strength of interparticle interaction is measured using a combination of optical microscopy, optical tweezers and applied magnetic

fields. Finally, cluster and network formation is studied as a function of interparticle interaction strength by varying the concentration of polymer present in solution.

Firstly, in Chapter 2, the basic concepts and methods used throughout this thesis are presented. Specifically, a brief introduction into the physics of colloidal systems, factors effecting the stability of colloid-polymer mixtures, and their meta stable states is given. Following this, a description of the experimental details, including sample preparation, images analysis techniques and method of optical tweezing, is provided.

Next, in Chapter 3, the xanthan sample used throughout this work is characterised using a combination of video microscopy, passive micro-rheology and polyelectrolyte rheological theory. The mean squared displacement of tracer particles is measured at several polymer concentrations and used to determine the associated diffusion coefficients. From these, the relative viscosity of each concentration is calculated and their relationship analysed using established and advanced techniques. From these results, the intrinsic viscosity of the xanthan solution is determined. Subsequently, the polymer coil overlap concentration and radius of gyration are calculated. Finally, the relationship between intrinsic viscosity and molecular weight are used to determine the Mark-Houwink prefactor.

A method for determining the strength of the depletion interaction between pairs of superparamagnetic caused by the presence of xanthan polymer in solution is presented in Chapter 4. A combination of bright-field microscopy, optical tweezer manipulation and image analysis techniques are used. Survival probabilities are determined by measuring the time taken for two separating particles to reach a separation distance threshold. By repeating the experiment numerous times, sufficient statistics are obtained to compare experimental survival probability results to theoretical calculations using a simple depletion interaction model.

In Chapter 5, the aggregation behaviour of quasi-two-dimensional colloid-polymer mixtures is studied as a function of polymer concentration. The results are analysed using established cluster growth theory by tracking the weighted mean cluster size as a function of time. A direct link between the weighted mean cluster size and cluster coordination number distributions is presented.

Finally, in Chapter 6, the formation and evolution of quasi-two-dimensional colloid-polymer networks is investigated as a function of polymer concentration. The pre- and post-percolation

growth of clusters is discussed and growth exponents are reported. The dynamics of clusters and networks during and after percolation are examined using a combination of bond-order orientational analysis and coordination number tracking.

Chapter 2

Theoretical background and experimental methods

ABSTRACT

In this thesis, the properties and dynamics of quasi-two-dimensional colloid-polymer systems are investigated. This chapter details a number of concepts and experimental methods which are common throughout. Firstly, the length and time scales of colloidal systems are defined, followed by a brief summary of interparticle interactions, including magnetic interactions. Secondly, an overview of colloid-polymer systems, including a description of the depletion interaction, is presented. Finally, a explanation of the methods used, including sample preparation, video microscopy and optical trapping, is given.

2.1 Physics of colloidal systems

2.1.1 Characteristic length and times scales

The colloidal domain is defined by a length scale in which objects, colloidal particles, have at least one dimension in the nm to μm range [54]. When dispersed in a liquid medium, they are subject to constant bombardment from solvent molecules in all directions. At any point in time, the number of collisions due to thermal motion are unevenly distributed about the colloidal particle. This leads to a stochastic movement characterized by a random walk. This phenomenon is referred to as Brownian motion and was first observed by Robert Brown in 1827 whilst studying particles trapped in pollen grains suspended in water. A theoretical understanding was later developed by Einstein in 1905 [29], which ultimately eluded to the existence of atoms and molecules supported by experimental evidence from work completed by Perrin in 1909 [30].

Brownian motion can be characterized by the mean squared displacement (MSD) $\left\langle \delta r^2(\tau) \right\rangle$ of an ensemble of particles, where $\langle r(\tau) \rangle$ is the mean displacement of particles as a function of time interval τ. The two or three dimensional space explored by a single particle over a time period τ is captured in the MSD. At infinite dilution, for a single particle, the MSD is given by

$$\left\langle \delta r^2(\tau) \right\rangle = 2dD_0\tau. \tag{2.1}$$

Dimensionality is specified by the constant d, while D_0 refers to the diffusion coefficient at infinite dilution. The Stokes-Einstein equation equals

$$D_0 = \frac{kT}{\zeta}, \tag{2.2}$$

where kT is thermal energy with k as the Boltzmann constant and T the temperature. The Stokes equation for the drag coefficient of a sphere in a continuous medium is

$$\zeta = 3\pi\eta\sigma. \tag{2.3}$$

The friction coefficient is determined by the solvent's viscosity η and the particle's radius, $a =$

$\sigma/2$.

A distinctive time scale, referred to as the Brownian time, is used to describe the time taken for a particle to diffuse over a distance equal to its own diameter such that

$$\tau_B = \frac{a^2}{D_0} = \frac{\sigma^2}{4D_0}. \tag{2.4}$$

The gravitational height, h_g, of a colloidal system is determined by the interplay between gravitational and thermal energy. This relationship dictates the degree to which a particle is elevated in a liquid medium due to thermal fluctuations in energy equivalent to kT. A large value of h_g is indicative of a system where particles are dispersed throughout the volume due to thermal agitation. The gravitational height takes the form

$$h_g = \frac{6kT}{\Delta\rho g\pi\sigma^3}, \tag{2.5}$$

and has a strong dependence on the particle's diameter, σ, as well as $\Delta\rho$, the density difference between dispersion medium and particle. If particles are large, g, acceleration due to earth's gravitational field, dominates and sedimentation occurs.

2.1.2 Interparticle interactions

DLVO interaction

Colloidal particles, dispersed in a medium, are subject to a number of different interparticle interactions. Two key interactions are the Van der Waals attraction and electrostatic repulsion. Colloidal dispersions are often subject to both forces, the theoretical framework for which was developed in the 1940's by Derjaguin, Landau, Verway and Overbeek and is referred to as DLVO theory [55, 56]. In this description, interactions are based on a pair potential, $U\left(\vec{r}\right)$, which corresponds to the energy between two particles as a function of their relative position in three-dimensional space $\vec{r}$. For spherically symmetric particles this simplifies to the interparticle distance r, such that

$$U_{DLVO}\left(r\right) = U_{VdW}\left(r\right) + U_{el}\left(r\right), \tag{2.6}$$

where $U_{VdW}(r)$ is the attractive and $U_{el}(r)$ the repulsive term.

Van der Waals forces are present between all atoms and molecules. Their attractive nature is based on momentary oscillations of an atom's electron cloud acting in concert with a neighbour's when in close proximity. The same rational is extended to colloidal particles in a medium by summing all individual interactions between particles and that medium. This treatment results in an attractive potential which can be approximated for two spheres at close separation by

$$U_{VdW}(r) = -\frac{A\sigma}{24h}. \tag{2.7}$$

The potential has an inverse dependence on the interparticle surface separation, h, where $h = (r - \sigma)$ and is proportional to magnitude of the Hamaker constant, A [57], and particle diameter, σ. The Hamaker constant is a property which depends on the material particles are made from and the medium used to dispersed them. It is always positive between two particles of the same material.

The repulsive contribution, $U_{el}(r)$, stems from ions present in a dispersion and their interplay with charged surfaces. The origins of surface charge are numerous, but ionization of surface groups is a common cause. In the bulk, anions and cations are distributed evenly. However, close to surfaces, concentration gradients are present. These decay over a length scale known as the Debye length, l_D [57,58]. The double layer repulsion for a particle pair is given by

$$U_{el}(r) = \begin{cases} +\infty, & \text{if } r \leq \sigma. \\ Z^2 kT\lambda_B \left(\frac{exp(\sigma/l_D)}{1+\sigma/l_D}\right)^2 \frac{exp(-r/l_D)}{r}, & \text{otherwise.} \end{cases} \tag{2.8}$$

The distance at which two elementary charges interact with an energy equal to kT is defined as the Bjerrum length, λ_B [58]. The number of elementary charges at a particle's surface is denoted by Z. At contact, the interaction potential is infinite as particles are modelled as hard spheres. At high salt concentrations, dispersion stability can be lost by effective screening of the surface charge, such that the Debye length reduces to just a few nm. Therefore particles in close proximity aggregate as $U_{VdW}(r)$ dominates interparticle interactions.

Magnetic interaction

Superparamagnetic particles mixed with a depletant were used as a model system throughout this thesis. In conjunction with the interparticle interactions summarised above, superparamagnetic particles also interact via a dipole-dipole interaction when subject to an external magnetic field. In the absence of a magnetic field, they do not. Their cores, which consist of iron oxide nano-domains, are responsible for this phenomenon. In the absence of an applied magnetic field, the dipole moment of each domain is randomised and no overall dipole exists. When exposed to an applied magnetic field, these domains align, resulting in an overall dipole moment. If an applied magnetic field is orientated in an appropriate direction, aggregation processes can be reversed, allowing a system to be re-dispersed at will. Due to their behaviour as dipoles, interparticle interaction energy is dependent on relative particle positions [59]. For an isolated pair, where each dipole moment aligns with the field $\vec{B}$, the potential $U_{mag}(r)$ is given by

$$U_{mag}(r) = \frac{1}{4\pi\mu_0}\frac{v_p^2\chi_v^2B^2}{r^3}\left(1-3\cos^2\theta\right), \tag{2.9}$$

where r is the interparticle distance, B the field magnitude and θ, the interparticle bond angle relative to the field's orientation in three-dimensional space. We redefine this equation in terms of colloidal length and energy scales. The interaction parameter, ξ, is a dimensionless constant for a fixed field strength. Hence,

$$\xi = \frac{U_{mag}(r)\,(\theta=0, r=2a)}{kT} = \frac{\pi a^3\chi_v^2B^2}{9kT\mu_0} \tag{2.10}$$

is consistent for two particles at contact and aligned with the external field. Equation 2.9 can now be rewritten as

$$\frac{U_{mag}(r)}{kT} = \frac{\xi}{2\,(r/2a)^3}\left(1-3\cos^2\theta\right). \tag{2.11}$$

However, in our experiments the field orientation and gravitational length is such that θ remains constant at $\pi/2$. Therefore, Equation 2.11 simplifies further still to

$$\frac{U_{mag}(r)}{kT} = \frac{\xi}{2\,(r/2a)^3}. \tag{2.12}$$

2.1.3 Stability of colloid-polymer mixtures

Effects of polymer on dispersion stability

Mixing colloidal particles with polymer solutions often results in two types of dispersion instability. Flocculation, due to bridging, and de-mixing, due to depletion. Flocculation is caused by an energetically favourable interaction between the segments of a polymer and the surface of a particle. Losses in the polymer's configurational entropy is offset by overall energetic gains. If the concentration of polymer is insufficient to achieve total surface coverage, bridging between particles may occur [27]. However, above a certain polymer concentration, total surface coverage is achieved and steric stabilization [60] can result instead. When polymers are non-adsorbing, aggregation may occur due to depletion [27].

Throughout this thesis, colloid-polymer mixtures are referred to by their colloid concentration, in terms of area fraction, ϕ_a, and relative polymer concentration, ϕ_p. Area fractions are related to sample particle volume fractions, ϕ_c, in the following way

$$N = \frac{3\phi_c V}{4\pi a^3}, \tag{2.13}$$

where N is the number of particles, $V = A_c h_c$ is the volume of the sample cell where A_c is the area and h_c the height. Thus, the area fraction is given by

$$\phi_a = \frac{3\phi_c h_c}{2\sigma}. \tag{2.14}$$

The relative polymer concentration, which reaches unity when polymer coils start to overlap, is considered to be the polymer volume fraction. The relative polymer concentration is

$$\phi_p = \frac{n_b}{n_b^*}. \tag{2.15}$$

The number density of polymer is determined by n_b and the number density at which coils start to overlap as n_b^*. The overlap concentration c^* is equivalent to n_b^* which is defined as

$$n_b^* = \frac{M v_s}{v_p}, \tag{2.16}$$

where the number of polymer segments is M and segment volume is v_s. The coil volume is determined by the polymer's radius of gyration, R_g, such that $v_p = \big(4\pi/3\big)R_g^3$. In an experimental setting, a more practical form of Equation 2.16, determined by the polymer's average molecular weight, $\bar{M}_w$, radius of gyration and Avogadro's number N_A, is used

$$c^* = \frac{3\bar{M}_W}{4\pi R_g^3 N_A}. \tag{2.17}$$

The depletion interaction

The depletion interaction, first proposed during the 1950's by Asakura and Oosawa [61], is an indirect attraction caused by an osmotic pressure imbalance. A layer devoid of polymer exists close to all surfaces. These regions occur due to a loss in configurational entropy if the polymer were to occupy them. When two or more of these depleted zones overlap, the overall volume available to the polymer increases and thus, so too, does the overall entropy of the system [61,62]. A theoretical framework for the depletion interaction was first proposed by Vincent *et al.* [63] and Vrij [62] through systematic investigations of colloid-polymer mixtures. At the dilute limit, well below c^*, the depletion potential for a given system is simply calculated as the product of its osmotic pressure and volume of overlapping depletion zones. For two particles in close proximity

$$W_{dep}\big(r\big) = -PV_{ov}\big(r\big), \tag{2.18}$$

where P is the ideal osmotic pressure and $V_{ov}\big(r\big)$ is the overlap volume at an interparticle distance r. This model is more commonly referred to as the AOV model, after its introduction by Asakura, Oosawa and later more detailed consideration by Vrij.

An elegant example of both depletion and bridging was observed in the work of Feng *et al.* [64] in colloid-polymer systems composed of 3-trimethoxysilyl propyl methacrylate (TPM) particles and polyethylene oxide (PEO) over a temperature range of $60 - 90\,^{\circ}\mathrm{C}$. By changing the temperature of the sample, the adsorption properties of the depletant were altered. At low temperature, polymers were non-adsorbing, with entropic factors dominating interparticle interactions. This led to the formation of close packed 2D crystals. At higher temperatures, the PEO became less soluble causing bridging interactions to occur. It was thought that enthalpic

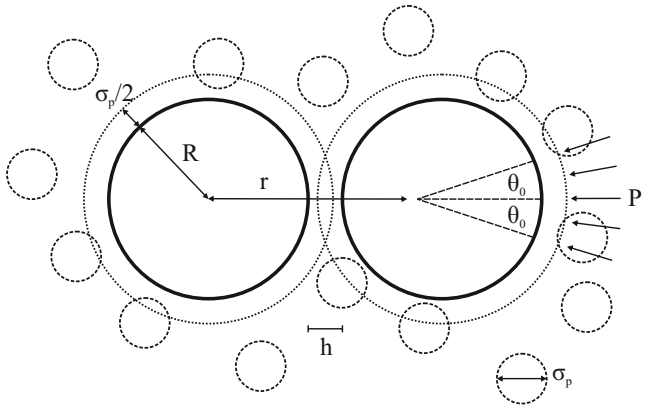


Figure 2.1: A sketch of the penetrable hard sphere volume exclusion arguments used to rationalise an osmotic pressure imbalance which leads to the attractive force between particles referred to as the depletion interaction.

interactions were responsible for this change in flocculation behaviour.

Depletion interaction between two spheres: Force method

First, we consider a hypothetical model system where the depletant is described by a penetrable hard sphere (PHS) with a diameter σ_p and a chemical potential of

$$\mu = k_B T \ln\left(n_b\right). \tag{2.19}$$

In this context, PHS are considered to behave as ideal polymers. These can overlap with each other, but behave as hard spheres of diameter σ_p when interacting with colloids and walls. When we consider the interaction between two spherical colloids, with a radius a, we determine the effective depletion radius as $R_d = a + \sigma_p/2$. When two particles approach each another and their separation r becomes less than R_d, a net force results. At this point, their depletion zones overlap, resulting in an uncompensated osmotic pressure imbalance (see Figure 2.1). This imbalance is due to the absence of any PHS between them, which gives rise to the attractive force. The uncompensated pressure effects the surface of each particle from $\theta = 0$ to $\theta_0 = \arccos\left(r/2R_d\right)$. Symmetry arguments mean only the line between the particle centres counts towards the total attractive force. For an angle θ this component is as $P\cos\left(\theta\right)$, where the pressure is simply $P = n_b kT$. By integrating from θ to θ_0 the total force between the two

spheres can be found

$$\begin{aligned}\frac{K_s(r)}{n_b kT} &= -2\pi\left(a+\sigma/2\right)^2\int_0^{\theta_0}\sin\theta\,\cos\theta\,d\theta \\ &= -\pi R_d^2\left[1-\left(r/2R_d\right)^2\right] \quad 2a \le r < 2R_d \\ &= 0 \qquad\qquad\qquad\qquad\qquad\qquad \ge 2R_d. \end{aligned} \tag{2.20}$$

By integrating the depletion force, the depletion potential can be obtained

$$\begin{aligned}W_s(r) &= \int_r^{2R_d} K_s(r)\,dr \\ &= -n_b kT V_{ov}(r) \qquad 2a \le 2R_d \\ &= 0 \qquad\qquad\qquad\qquad \ge 2R_d, \end{aligned} \tag{2.21}$$

where

$$V_{ov}(r) = \frac{4\pi}{3}R_d^3\left[1-\frac{3}{4}\frac{r}{R_d}+\frac{1}{16}\left(\frac{r}{R_d}\right)^3\right] \tag{2.22}$$

and

$$V_{ov}(h) = \frac{\pi}{6}\left(\sigma-h\right)^2\left(3a+\sigma+h/2\right). \tag{2.23}$$

Depletion interaction between a sphere and wall

The strength of the depletion interaction between a sphere and a flat plate can be calculated using a modified version of the force method. A modified version of the Gibbs adsorption equation can also be used, the result of which is

$$W_{sp}(h) = -n_b kT\pi a(\sigma-h)^2. \tag{2.24}$$

This can be used to calculate the interaction strength when $a >> \sigma$.

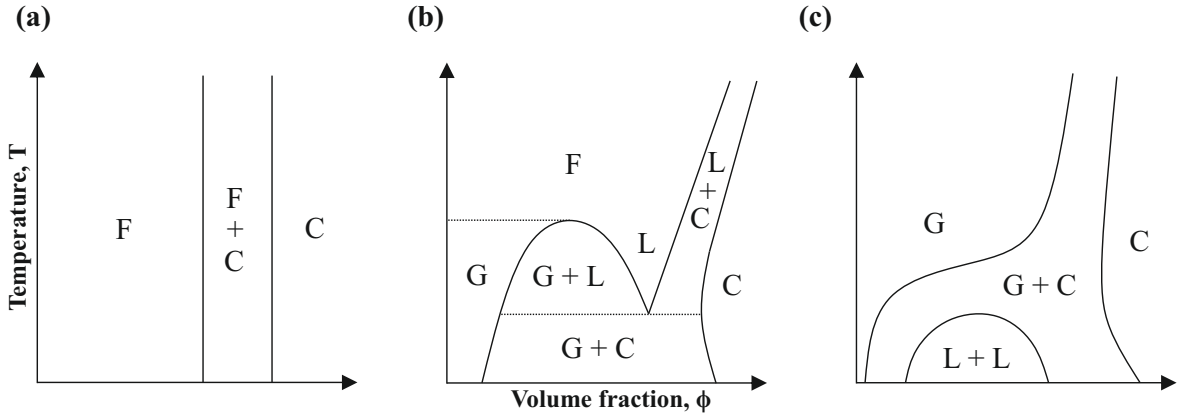


Figure 2.2: Phase diagrams for systems with (a) hard sphere, (b) long ranged and (c) short range interactions. Long ranged interactions, which are equivalent to large values of q, are often used as models for atomic systems due to the presence of solid, liquid and gas phases. Short range interactions, which equate to a smaller values of q, are dominated by a liquid – liquid region. Diagrams (a),(b) and (c) are redrawn from [27].

2.1.4 Colloid-polymer mixtures and their arrested states

Equilibrium phase behaviour of colloid-polymer systems

The monodispersed hard sphere system represents the simplest form of colloidal system. Here, particles cannot overlap and there is no other significant interparticle interaction, giving a pair potential of the form

$$v(r) = \begin{cases} \infty & \text{for} \quad r < \sigma \\ 0 & \text{for} \quad r \geq \sigma, \end{cases} \tag{2.25}$$

where σ is the particle diameter and r the interparticle separation. Phase behaviour is governed purely by packing fraction, ϕ_c. Entropy alone dictates the behaviour of the system, which results in the phase behaviour illustrated in Figure 2.2 (a). Although this type of interaction gives rise to relatively simple phase behaviour, the transition between phases is still a rich and sometimes contested area of research. This is especially true when considering two-dimensional systems of hard disks [65]. However, as longer range interactions are introduced, this rudimentary phase behaviour is altered dramatically.

The introduction of long ranged interactions results in colloidal systems which exhibit phase behaviours comparable to those of atomic and molecular systems [66]. Here all three

phases, liquid, crystal and gas are at equilibrium, synonymous with the triple point of atomic systems such as Argon. However, as the range of interparticle interaction is reduced, phase behaviour unique to short range attraction is observed. The liquid-liquid region (Figure 2.2 (c)) becomes metastable. The addition of non-adsorbing polymer to colloidal dispersions generates this type of interaction while allowing the strength and range to be easily controlled and results in the metastable phase behaviour described above.

Due to the geometric arguments illustrated in Figure 2.1, the range and depth of the interaction potential, and subsequently a system's phase behaviour, is controlled by the size ratio of the polymer coil, characterised by the polymer's radius of gyration, R_g, to particle radius; hence

$$q = \frac{R_g}{a}. \tag{2.26}$$

For a fixed value of q, the strength of interaction is solely determined by the concentration of polymer, ϕ_p. As R_g is increased so too does the range of interaction. A value of $q > 0.3$ implies a long range interaction and a phase behaviour similar to that depicted in Figure 2.2 (b). For a value of q typically > 0.3, and at low ϕ_p, similar phase behaviour to that of a hard sphere system is observed. However, as ϕ_p is increased the colloidal fluid phase (Figure 2.3 (a)) becomes unstable and gas-liquid (GL) phase separation occurs. Increasing ϕ_p further still results in a gas-crystal coexistence region. In between lies the gas-liquid-crystal (GLC) coexistence region. For systems with $q < 0.3$, the GL is not realised and the GL separation becomes metastable with respects to phase separation. However, in experimental systems, this thermodynamically favoured state is not reached due to the formation of a colloidal gel. The value of q is also important when considering if a system is pairwise additive or not.

Meta stable states - gels

Gels can be classified into two major groups as either physical or chemical gels [48]. Chemical gels, like epoxy resins or rubber, are those with an infinite bond lifetime. This is usually the result of covalent bonds being formed. These gel types have been well studied in polymer science and conform to the conventions of percolation theory. Physical gels are those gels which originate from physical interactions approximately equal to one or two orders of magnitude of

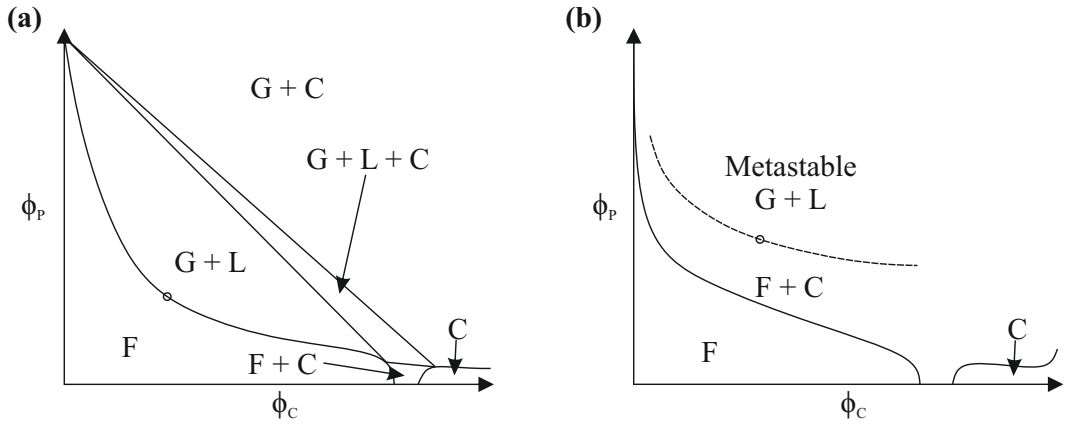


Figure 2.3: Phase diagrams depicting the difference between colloid-polymer systems with a) q > 0.3 and b) q < 0.3. An inverse relationship exists between polymer concentration ϕ_p and temperature, as depicted in figure 2.2(a), which effectively inverts the phase diagrams. As q becomes smaller, the phase diagram simplifies with the loss of the Gas – Liquid – Crystal coexistence region, but is dominated by the Gas – Liquid metastable region. The following legend applies, Fluid (F), Liquid (L), Gas (G) and Crystal (C).

kT. Therefore, connections formed can reversibly break and reform many times during the lifetime of the gel [48].

Physical gels are complex fluids comprised of a discrete solid phase dispersed or dissolved in a fluid phase. The bulk of their mass originates from the fluid phase and yet they exhibit the properties and characteristics typical of a solid, for example they exbibit a non-zero yield stress. Particle gels consist of interacting nm to μm sized particles suspended in a fluid. When inter-particle interactions are strong enough and particle concentrations high enough, space spanning networks can form, composed of individual particles, which gives rise to the aforementioned rheological properties. This thesis is concerned with the interactions, formation and structure which give rise to the phenomenon of particle gelation. The existence of a particle gel regime can be rationalised in the following way. When ϕ_p is large enough, particles which come into contact will stick to one another for a finite length of time. If the particle concentration, ϕ_c, is above a certain threshold, this process will eventually lead to the formation of a space spanning network. This effectively freezes the system via kinetic arrest, at which point gelation has occurred. Whilst it is easy to conceptualise the process of gelation, the pathways which lead to it are more complicated to unravel [48]. This thesis is specifically concerned with investigating those pathways in two-dimensional colloid-polymer systems.

2.2 Methods

2.2.1 Two-dimensional model systems

Colloid-polymer mixtures consisting of superparamagnetic particles, Dynabeads® M-270 [67] manufactured by ThermoFisher Scientific, dispersed in xanthan gum solutions were used exclusively throughout this work. Colloidal dispersions and stock xanthan solutions were mixed at appropriate concentrations, depending on the experimental requirements, immediately before being introduced into an appropriate sample cell. This allowed the formation of quasi-two dimensional model systems, where particles sediment onto the bottom of a sample cell and remain confined in a monolayer due to gravitational forces. The specifics of these model systems are described below.

Superparamagnetic particles

Dynabeads® are composed of iron oxide cores embedded in a highly cross-linked polystyrene matrix resulting in monodispersed spheres with a polydispersity index of (PDI) $< 3\%$ and a mass density of $\rho = 1.6\,g\,cm^{-3}$. The diameter of these particles was measured to be $\sigma = 2.8\,\mu m$ in water and $\sigma = 3.0\,\mu m$ in a 20/80 $wt/wt\%$ ethanol/water solvent mixture. Both of these were determined using radial distribution measurements. The surfaces of these particles were functionalised with carboxylic acids, resulting in a net negative charge. Therefore, these particles were charge-stabilised in both of the aforementioned solvent systems. This prevented interparticle aggregation and particle pinning to glass surfaces. The presence of embedded iron oxide γFe_2O_3 and Fe_3O_4 nano-particles is responsible for the superparamagnetic properties these particles exhibit (Section 2.1.2).

Preparation of xanthan solutions

Xanthan gum was used as the depletant in this work. A highly refined, mean molecular weight $\bar{M}_w = 4.5 * 10^6\ g\ mol^{-1}$ sample of xanthan powder was purchased from Sigma-Aldrich, with a narrow molecular weight distribution. Initially, a stock solution of 0.1% wt/wt was prepared by dissolving xanthan powder into a 20/80 $wt/wt\%$ ethanol/water solution. The mixture was

(a) (b)

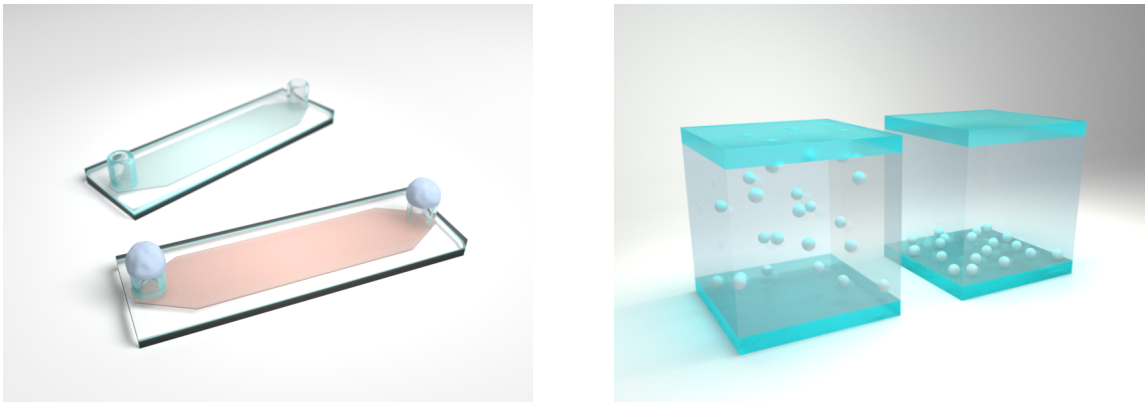


Figure 2.4: (a) shows an empty cell (top) and an injected and sealed cell (bottom). The brown tinge in the bottom cell is due to the iron oxide component of the superparamagnetic particles. (b) shows a rendering of the sedimentation process which occurs once the sample has been injected into the cell. The left cross-section shows particles dispersed throughout the cell immediately after injection and the right cross-section after they have sedimented on to the bottom glass surface. Rendering is not to scale.

stirred for 48 hrs at room temperature, after which all xanthan powder had dissolved. The solution was centrifuged at 4500 *rpm* for 90 minutes to remove any large aggregates or debris. This stock solution was used to make a range of subsequent dilutions of different concentrations. The ϕ_p for all samples were calculated using Equation 2.15.

Sample cell

A custom-made quartz flow cell (Hellma® Cell) with an internal width of 9 mm and length of 20 mm was used for all experiments. The internal height was 200 μm. Prior to use, the cell was cleaned with a 2.0% solution of Hellmanex® III at 50 °C for 10 minutes, flushed through with deionized water and isopropanol, then dried using N_2 gas. It was subsequently plasma cleaned immediately prior to sample injection unless stated otherwise. Once injected, the cell was sealed using Blu − Tack® to prevent solvent evaporation and sample contamination. Figure 2.4 shows an example of both the empty (back) and prepared sample cell (front).

2.2.2 Video microscopy

Throughout this thesis, video microscopy was used for data capture. A Ximea XiQ CMOS camera was utilised in a range of different optical setups. An Olympus CKX41 inverted bright-field microscope was used in Chapters 3, 5 and 6. Depending on the specific experiment, either a Olympus 20× or 40× magnification objective was used. A custom LED light source was used to provide sample illumination. All setups and objectives were checked for residual magnetic fields before being used in experiments.

2.2.3 Image analysis

Individual particle coordinates were extracted using custom image analysis algorithms. Raw images were processed using the following protocol. Initially, a bandpass filter was applied to remove unwanted background noise. This resulted in a smoothed image with a number of radially symmetric, bright, features. Subsequently, a thresholding algorithm was used to covert the image to binary pixel values of 0 and 1. Image components were then selected based on object area and circularity. The centres of these objects was determined using a standard centroid function. A summary of this process is depicted in Figure 2.5. As the features detected are several pixels in diameter, particle positions can be determined with a very small error.

2.2.4 Optical trapping

Optical trapping is a technique which allows matter to be manipulated at the colloidal length scale. Ashkin discovered that a highly focused laser beam can be used to 'trap' and move dielectric particles if the refractive index mismatch between them and the surrounding medium is large enough [68].

Two forces dominate the physics of this technique: the scattering force and the gradient force. For simplicity, we only consider the ray optics regime [69] where the size of the particle is far larger than the wavelength of light used to trap it. As a light ray hits a particle, depending on its angle of incidence, it is refracted. This change in direction is accompanied by a change in momentum. Due to the law of conservation of momentum, an equal and opposite momentum change is imparted to the particle.

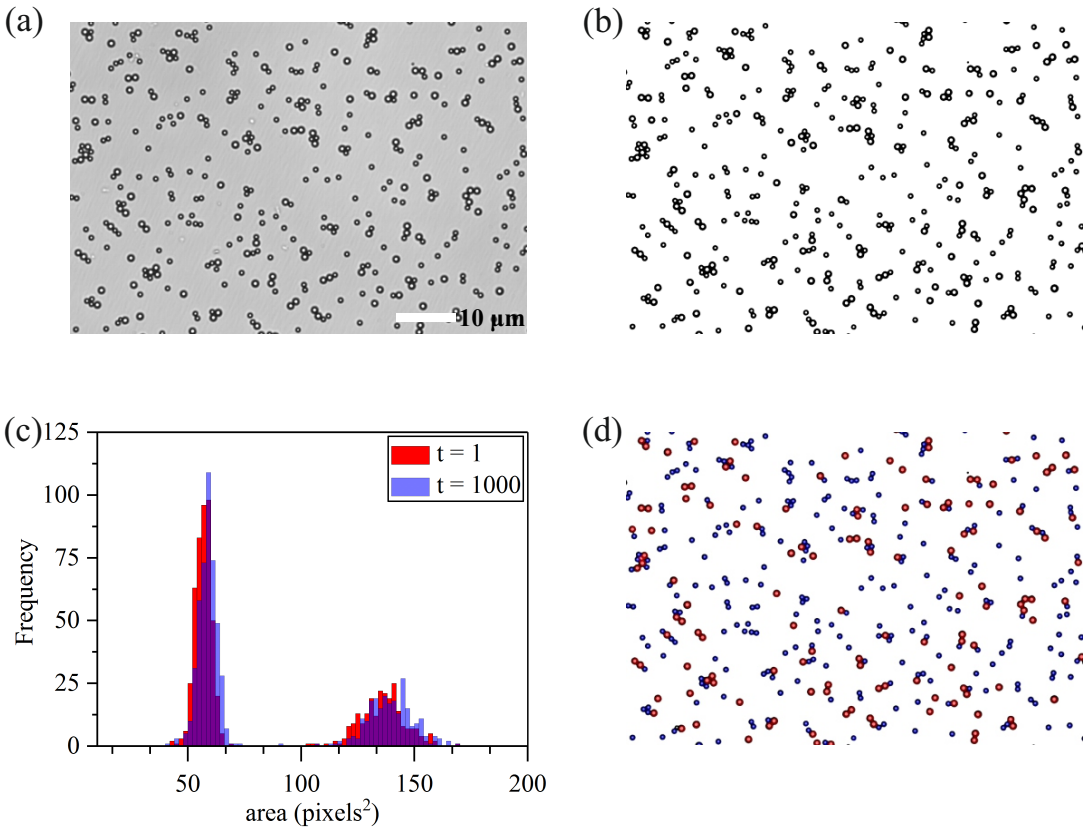


Figure 2.5: Example of the image analysis process for a binary test system: (a) raw image taken with a 40× Olympus objective; (b) the same image after application of a Gaussian filter and binarization using thresholding; (c) an example histogram of detected objects by pixel area showing a clear bimodal distribution allowing effective identification of large, σ_l, and small, σ_s, particles; (d) results of particle detection with σ_l coloured red and σ_s coloured blue.

When the intensity profile of the trapping beam is Gaussian, a net restoring force results if a particle is displaced from the centre of the beam. The magnitude of this force is dependent on the particle's X and Y distance relative to the beam axis. This is referred to as the gradient force (Figure 2.6) and is responsible for fixing the particle's relative X and Y position. However, the particle's position in Z is effectively unbounded. By focusing the beam, the particle's position in Z can also be controlled. This is achieved by utilising the scattering force.

As the same Gaussian beam is focused, scattering forces dominate as light rays are no longer parallel to one another when they approach the particle's surface. Depending on the particle's position, two limiting cases emerge (Figure 2.6). If the particle is higher than the focal

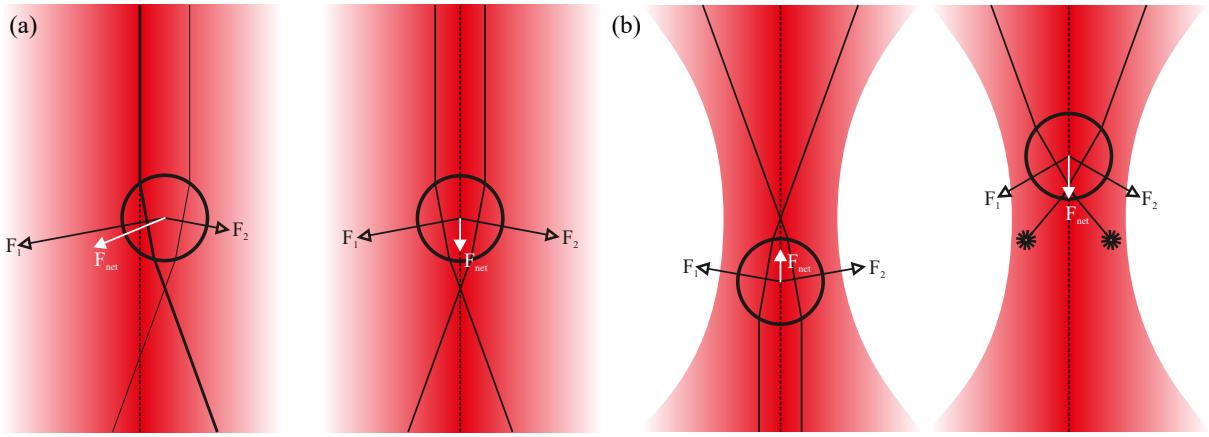


Figure 2.6: Ray diagrams depicting the two forces responsible for holding a particle at a fixed position in real space. The gradient force (a) and the scattering force (b).

point, a net restoring force results driving it back towards it. If it is below the focal point, a net force pushes it the particle back towards the focal point. This behaviour is in part due to the curvature of the particle's surface and change in angle of incidence.

By applying these basic trapping principles, together with either a spatial light modulator (SLM) or acousto-optic deflector (AOD), a trapping beam can be 'steered'. This allows a trapped particle to not only be moved in X, Y and Z, but affords the ability to generate multiple traps simultaneously. By this manner, ensembles of particles can be moved independently of one another in real-time. This technique was used extensively in Chapter 4 and allowed repeat experiments to be performed thousands of times.

Chapter 3

Polymer characterisation via passive microrheology

ABSTRACT

In this chapter, the intrinsic viscosity, polymer coil overlap concentration and radius of gyration of a xanthan sample is determined via the mean squared displacement of tracer particles embedded in the polymer solution. The same polymer and solvent mixture is used to generate the depletion interaction studied throughout this thesis. First, tracer particles are used to measure diffusion coefficients and viscosities for a number of xanthan solutions, of known molecular weight, at different concentrations. The viscosity of the pure solvent is also measured. The intrinsic viscosity is found and compared using a linear, exponential and Wolf (B. A. Wolf 2007) fitting method, from which the overlap concentration and radius of gyration are calculated. By substituting the known molecular weight and measured intrinsic viscosity into the Mark-Houwink equation, the Mark-Houwink coefficient is calculated. This can be used to quantify the molecular weight of an unknown xanthan sample in the future, using the same solvent system and methodology described herein.

3.1 Introduction

In dilute colloid-polymer solutions, the range and strength of the depletion interaction are determined by the polymer's radius of gyration and concentration, respectively [27]. Both of these are affected by the nature of the solvent. The molecular weight and radius of gyration of a polymer in solution are intrinsically linked; if the polymer's molecular weight, M_w, is known, its radius of gyration, R_g, can be estimated using an appropriate theoretical model [70]. However, these models can be limited in their ability to evaluate these quantities accurately, especially if the polymer is structurally complex or particularly sensitive to the solvent conditions, as is the case for polyelectrolytes like xanthan [19, 71–77]. Therefore, in order to quantify the R_g and polymer coil overlap concentration, c^*, of xanthan used throughout this thesis, whilst taking the aforementioned effects into account, we measure these quantities experimentally by probing the diffusion of tracer particles in xanthan solutions as a function of the polymer concentration.

A solution's resistance to flow, its viscosity, can be significantly affected by the addition of only small amounts of polymer. Commonly, the viscoelastic effects induced by the addition of polymer are determined by viscometry [70]. Gravimetric viscometers are used to investigate a solutions resistance to flow for fixed conditions whereas rheometers are used to probe a solutions behaviour as these flow conditions are varied [78]. However, both methods require considerable quantities of sample, on the order of several mL. Measurements using conventional capillary viscometers can suffer from shear thinning effects when used to investigate large molecular weight polymers [79] like xanthan, and rheology, whilst sensitive, can suffer from surface tension effects [80] when measuring dilute polymer solutions of an aqueous nature. Microrheology, where one physically probes the properties of a solution at the microscopic level, provides an alternative approach for characterizing the properties of polymer solutions.

Passive microrheology uses tracer particles to measure small changes in a solution's viscosity by analysing the trajectories of individual particles caused by thermal motion [81]. From these trajectories the mean squared displacement can be calculated and in turn, due to the drag forces acting on each particle, a viscosity can be determined. Whilst only requiring modest quantities of sample, on the order of a few μL, it does not suffer from the same surface tension effects as using a rheometer does. This allows small changes in low polymer concentration aqueous solutions to be quantified and provides an alternative approach for measuring their viscous

behaviour.

By measuring the viscosity at several different polymer concentrations, key dimensions of a polymer can be obtained if the intrinsic viscosity, $[\eta]$, is known. The intrinsic viscosity is a measure of the degree to which the pure solvent's viscosity has changed with the addition of polymer, but in the limit of zero polymer concentration [70]. The reciprocal of this value gives a measure of the polymer coil overlap concentration, c^*, where the concentration of polymer coils is such that they start to touch. From this, the polymer's radius of gyration, R_g, can also be calculated if its M_w is known [79].

In this chapter, c^* and R_g are experimentally determined for a xanthan sample with $M_w = 4.5 * 10^6 g\ mol^{-1}$ by measuring its intrinsic viscosity in a low-salt, water/ethanol solution. The intrinsic viscosity is used to determine the Mark-Houwink coefficient [79], K_w, which can be used to determine the M_w of other xanthan samples with unknown M_w using the same solvent system. Several established experimental techniques are combined in a novel manner to measure these values. Tracer particles are mixed into xanthan solutions of several different concentrations. Due to the small gravitational height of the system, the particles sediment onto the bottom wall of the sample cell and subsequently exhibit a 2D random walk due to thermal fluctuations. By analysing particle trajectories, the mean squared displacement at each polymer concentration is found and from this, the associated diffusion coefficients and viscosities are determined. By fitting to the viscosity data using a linear [70, 79], exponential [82] and Wolf fit [82], the $[\eta]$, c^* and R_g are determined. Finally, the Mark-Houwink coefficient is also found, which can be used in follow on studies to measure the unknown mean molecular weight of future xanthan samples.

3.2 Theory

3.2.1 Viscosity, rheology and mean squared displacement

Viscosities of solutions

The flow characteristics of a solution can be dramatically altered by the small addition of a high-molecular-weight polymer, like xanthan gum [18]. The introduction of only a small amount can cause a significant thickening and thus reduction in flow rate [77]. The ease with which a

solution is able to flow is referred to as its dynamic or absolute viscosity, η, with SI units of pascal seconds, $Pa.s$.

The simplest non-dimensional measure of a solutions viscosity is its relative viscosity, η_r, which is the ratio of solution viscosity to solvent viscosity and is defined as

$$\eta_r = \frac{\eta}{\eta_s}, \tag{3.1}$$

where η_s is the solvent viscosity and η the solution viscosity [79]. Following from this, the specific viscosity

$$\eta_{sp} = \eta_r - 1 = \frac{\eta - \eta_s}{\eta_s}, \tag{3.2}$$

is the difference between the relative viscosity from unity [70]. Here, the numerator accounts for the polymer contribution to the solution viscosity. Therefore, the specific viscosity is an important dimensionless measure of the polymer contribution to the solution viscosity. Finally, the reduced viscosity, $\eta_{red} = \eta_{sp}/c$, is the ratio of the specific viscosity to polymer concentration with units of reciprocal concentration, $dm^3\ g^{-1}$ [79].

A solution's viscosity increases linearly above the pure solvent viscosity, at very low polymer concentrations where individual polymer coils are far from one another, as the contribution of each coil to the solutions viscosity is additive. The effective 'virial expansion' for the viscosity of a solution [79], at low polymer concentration, is

$$\eta = \eta_s(1 + [\eta]c + k_H[\eta]^2c^2 + ...), \tag{3.3}$$

and has the same form as the well known virial expansion for osmotic pressure. Here, the linear term, $[\eta]c$, with respect to polymer concentration contains the intrinsic viscosity, $[\eta]$, and the quadratic term, the Huggins coefficient, k_H [83].

Intrinsic viscosity

The intrinsic viscosity, $[\eta]$, of a polymer in solution, held at constant temperature and pressure, represents the specific hydrodynamic volume of the polymer, in the absence of shear and in the

Conformation	α
Linear flexible chain (theta solvent)	0.5
Linear flexible chain (good solvent)	0.7 - 0.8
Rigid	>1

Table 3.1: Values of the Mark-Houwink exponent with respects to solvent-polymer interactions and polymer conformations [70].

limit of infinite dilution. The $[\eta]$ characterises the volume 1 gram of polymer would occupy, in solution, if it consisted solely of isolated coils. In the case of polymers well below the coil overlap concentration, at the limit of low polymer concentrations, the η_{red} becomes a significant property of the solution and is referred to as the intrinsic viscosity [79],

$$[\eta] = \lim_{c \to 0} \frac{\eta_{sp}}{c}. \tag{3.4}$$

When introducing polymer to a solution, polymers with large dimensions, for example M_w, result in a greater increase in the $[\eta]$. The intrinsic viscosity is related to the size of the polymer coil by the Max-Flory equation [79, 84]

$$[\eta] M_w \sim R^3, \tag{3.5}$$

where R^3 is the size of the polymer chain and is proportional to the volume occupied by the polymer coil in solution. As polymers are fractal, a power law relationship exists between their molecular weight and size where $M_w \sim R^{D_f}$ and D_f is the fractal dimension [79]. Therefore, the intrinsic viscosity of a solution can be expressed via the Mark-Houwink equation [85, 86]

$$[\eta] = K_w M_w^{\alpha}, \tag{3.6}$$

where K_w and α are the Mark-Houwink parameters and M_w is the polymer's average molecular weight. Both the constant K_w and Mark-Houwink exponent $\alpha = (3/D_f) - 1$ are polymer and solvent dependent, with K_w being specific to the polymer-solvent system. Values of α for the three classifications of solvent, poor, theta and good, are summarised in Table 3.1.

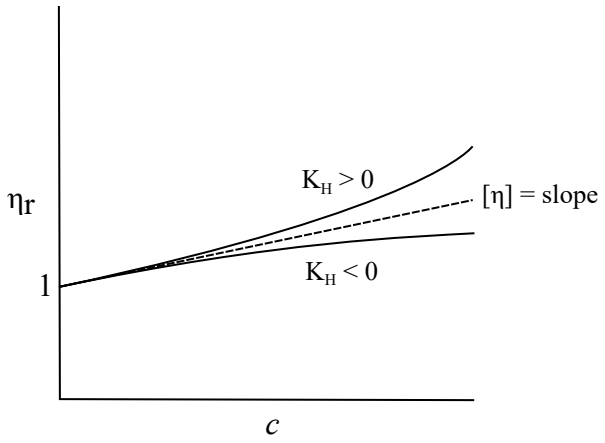


Figure 3.1: Plot of relative viscosity η_r as a function of polymer concentration c. The effects of the second-order coefficient, k_H, results in a positive or negative deviation depending on its sign.

Solvent-polymer interactions

In a good solvent, interactions between polymer segments and solvent molecules are energetically favourable, causing polymer coils to expand. In poor solvents, polymer-polymer interactions are favoured over polymer-solvent interactions, which leads to a contraction of polymer coils. In a theta solvent, which is between these two extreme cases, the polymer chain is imagined to act as an ideal polymer. For a given solvent-polymer combination, this normally occurs at a specific temperature. Under these conditions, measurements of a polymer's characteristics, for example its R_g, become independent of solvent effects. Generally, however, any polymer characterisation is highly dependent on the solvent it is dispersed in [87].

Determination of intrinsic viscosity

The intrinsic viscosity of a polymer can be experimentally determined by measuring the relative viscosity, η_r, of a solution as function of polymer concentration, c, using Equation 3.3 in the following form [79]

$$\eta_r = \frac{\eta_{meas}}{\eta_s} = 1 + [\eta]c + k_H c^2 + ..., \tag{3.7}$$

where $\eta_{meas} = \eta$ is the measured viscosity and η_s the pure solvent viscosity. Figure 3.1 illustrates

the relationship of η_r as a function of c. By obtaining the slope in the low concentration limit, the linear coefficient $[\eta]$, from Equation 3.7, can be found. The polymer coil overlap concentration, c^*, can also be calculated from the $[\eta]$ as $c^* = 1/[\eta]$ [79]. Both η_s and η_{meas} can be measured experimentally by analysing the mean squared displacement of embedded tracer particles. In this instance, the Stokes-Einstein Equation 2.2 rearranges to

$$\eta_{meas} = \frac{kT}{3\pi D_0 \sigma}, \tag{3.8}$$

and hence a solution's measured viscosity, η_{meas}, can be determined if the diffusion coefficient, D_0, is known. By tracking an ensemble of particles, D_0 can be calculated from tracer particle trajectories and their MSD $\left\langle \delta r^2(\tau) \right\rangle$ using

$$\left\langle \delta r^2(\tau) \right\rangle = 2dD_0\tau, \tag{3.9}$$

with d the dimensionality and τ the lag time. At $c = 0$, $\eta_{meas} = \eta_s$ and $\eta_r = 1$. However, when $c \neq 0$, typically $\eta_{meas} \neq \eta_s$ and $\eta_r \neq 1$.

3.3 Experimental method

A stock solution of 80/20 % (wt/wt) deionised water/ethanol was prepared and used as the solvent mixture for all experiments in this thesis. Superparamagnetic particles (Dynabeads©) with a diameter of $\sigma = 3.0\ \mu m$ were purchased from the manufacturer in deionised water. They were re-dispersed in the water/ethanol solvent mixture by a process of centrifugation and supernatant removal. Once the supernatant was removed, the particles were re-dispersed in the solvent mixture. This protocol was repeated three times in order to ensure the solvent mixture of the particle dispersion matched that of the stock ethanol/water solution.

A 0.1% (wt/wt) stock xanthan solution was prepared using the solvent mixture. The stock xanthan solution was diluted to prepare eight further xanthan dilutions with concentrations of 0.019, 0.036, 0.071, 0.131, 0.190, 0.379, 0.476 and 0.942 $g\ dm^{-3}$. For each sample, a xanthan dilution was selected and 80 μL of solution was pipetted into a microcentrifuge tube, the mass of which was recorded using an analytical balance. To this, 1 μL of the superparamagnetic tracer particle dispersion was added resulting in an $\phi_a < 0.001$, and the total mass recorded.

Next, the sample was mixed thoroughly and injected into a Hellma Cell©. This was left until all particles had sedimented to the bottom of the cell wall. During the sedimentation period, the sample was placed in a magnetic field of strength 4.5 mT. The field was orientated orthogonal to cell's lower surface inducing a repulsive interparticle interaction, U_{mag} (see Equation 2.9). This procedure separated any pairs or clusters which formed due to the depletion interaction.

Immediately prior to measurement, the sample was removed from the field and imaged using an Olympus CKX41 inverted microscope and UCPlanFLN 40× magnification 0.70 infinity/0-1.6/FN22 Olympus objective. Images were captured at a frame rate of 10 fps for a period of $\approx$ 15 minutes. Once this time had elapsed, the sample was removed from the microscope and placed back into the applied magnetic field. For some samples (see Table 3.2), repeat experiments were performed by imaging several different regions of the same cell. For certain concentrations (see Table 3.2) several samples with the same concentration were prepared and imaged. Once a sample had been imaged the desired number of times, the sample cell was flushed with deionised water, followed by isopropanol and finally dried with N_2 gas before being re-injected with a new sample. Plasma cleaning of the cell was omitted between each sample to avoid any unwanted temporary charging of the cell's internal surfaces. The degree of magnetization of the objective used in these experiments was characterised using a gaussmeter and found to have no significant residual field likely to effect the experiments. It was also checked that the microscope did not have a residual field either.

3.4 Results and discussion

First, particle trajectories were analysed to calculate the mean squared displacement (MSD) for every experiment performed. Where repeat experiments were conducted on the same sample, the average of the mean squared displacements (MSDs) was calculated. For different samples prepared at equivalent polymer concentration, a subsequent average of the mean squared displacements was used, as was the average polymer concentration. These results are shown in Figure 3.2 (a) and summarised in Table 3.2. As expected, a clear decrease of the MSDs was observed as the concentration of polymer increased. For all concentrations, the MSDs appeared to be linear at both short and long times, typical of short and long-time diffusive behaviour. By fitting Equation 3.9 to the data shown in Figure 3.2 (b), using a least squares fit, D_0 was

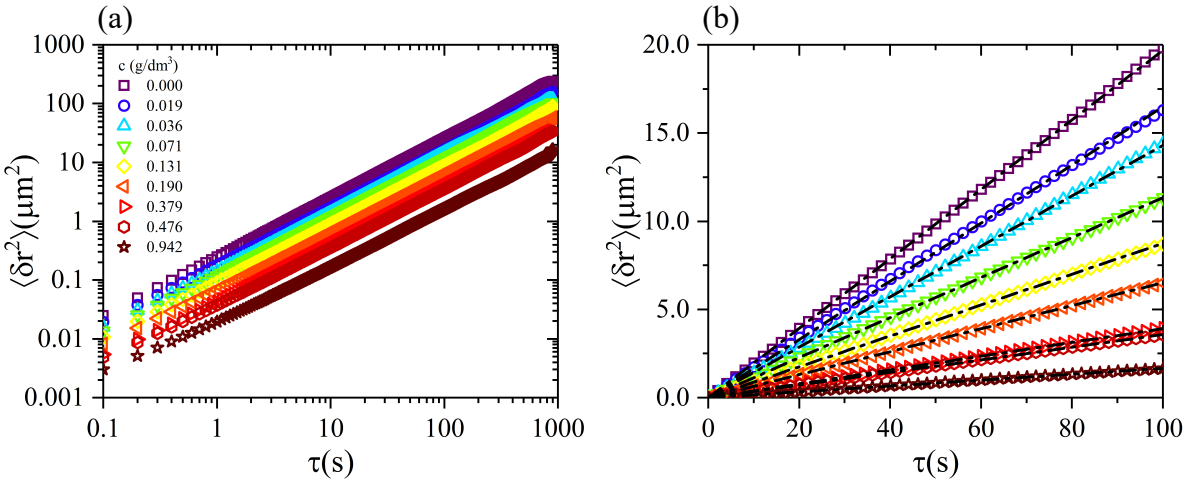


Figure 3.2: (a) A log-log plot of mean squared displacement for all xanthan concentrations as a function of time. (b) A linear-linear plot of the mean squared displacement for all xanthan concentrations investigated. Symbols are experimental results, dashed lines are linear fits used to determine each diffusion coefficient.

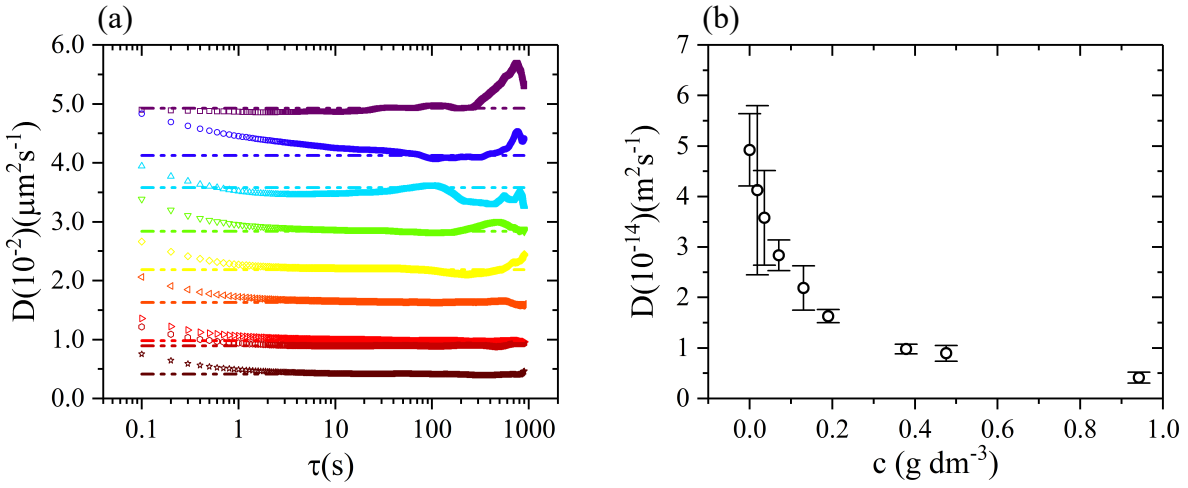


Figure 3.3: (a) The measured diffusion coefficient (symbols) plotted as a function of lag time. Dashed lines represent the diffusion coefficients calculated by fitting to the data shown in Figure 3.2 (a). The same legend is used as in Figure 3.2 (a). (b) A plot of the measured diffusion coefficient as a function of polymer concentration with the associated error of the dependant variable. The diffusion coefficient decreases as a function of increasing polymer concentration.

determined for each polymer concentration (see Table 3.2). All fits included data from $\tau = 0.1$ to $\tau = 100$ s and were fixed through the origin. At zero lag time a particle's displacement will be zero, therefore, when fitting to these data, we fit to the origin. We note however in some instances this is not considered appropriate, as there will always be an associated error in determining an object's, in this case colloid particle's, position. However, due to the length

Reference	C_0	C_1	C_2	C_3	C_4	C_5	C_6	C_7	C_8
no. samples	3	1	1	3	3	3	2	2	1
no. experiments	6	1	1	9	5	14	9	7	2
$c\ (g\ dm^{-3})$	0.000	0.019	0.036	0.071	0.131	0.190	0.379	0.476	0.942
$D_0\ (10^{-2})(\mu m^2 s^{-1})$	4.92	4.12	3.58	2.84	2.19	1.63	0.98	0.89	0.41
$\eta_{meas}\ (mPa.s)$	2.91	3.53	4.07	5.13	6.66	8.93	14.9	16.3	35.1
$\tau_b\ (s)$	45.70	54.56	62.86	79.30	102.90	138.04	229.66	251.61	543.09

Table 3.2: A summary of results and experimental details. Where more than one experiment was conducted, the average measurement is reported.

scales in colloidal systems, particularly at the length scales considered here, this error is small. This is due to the large size difference between the particle, at 3000 um diameter, and tracking error, which is well established in the literature to be sub nm.

To ensure the best estimation of each D_0, fitting results were superimposed (see Figure 3.3 (a)) on a plot of $\left\langle \delta r^2(\tau) \right\rangle / 4\tau$, for each polymer concentration as a function of τ. This allowed the time dependence of the diffusion coefficient to be examined, which for $c = 0$, is expected to result in a constant, flat, function with respects to τ. For the solvent mixture, with no added polymer, the expected flat behaviour was indeed observed. However, for all solutions containing polymer, an increase in the diffusion coefficient was found as $\tau \to 0$. Possibly, this is caused by a depletion effect, where a small volume around the particle is free from polymer, such that the particle can effectively move through the solvent unhindered whilst within this void [88–90]. At longer times, and therefore larger distances, this effect was not apparent as the particle moved through the bulk of the polymer coils. However, as we are interested in the polymer properties, i.e. M_w and $[\eta]$, we are only concerned with D_0, where $\tau \to \infty$. The noticeable variation in D_0 at long lag times is due to the typically poor statistics encountered at these times.

The effects of polymer concentration on D_0 are shown more clearly in Figure 3.3 (b). As the concentration of polymer was increased, the solution became more viscous and particles diffused over increasingly smaller distances, for a fixed period of time, resulting in the observed decrease in D_0. At low polymer concentrations, from $c = 0.00 - 0.2\ g\ dm^{-3}$, the largest differences in D_0 were observed, with only small changes appearing at higher polymer concentrations, from $c = 0.25 - 1.0\ g\ dm^{-3}$. Extrapolating to higher concentrations still, the diffusion coefficient approach zero, as the tracer particles become trapped in a polymer gel network and cease to

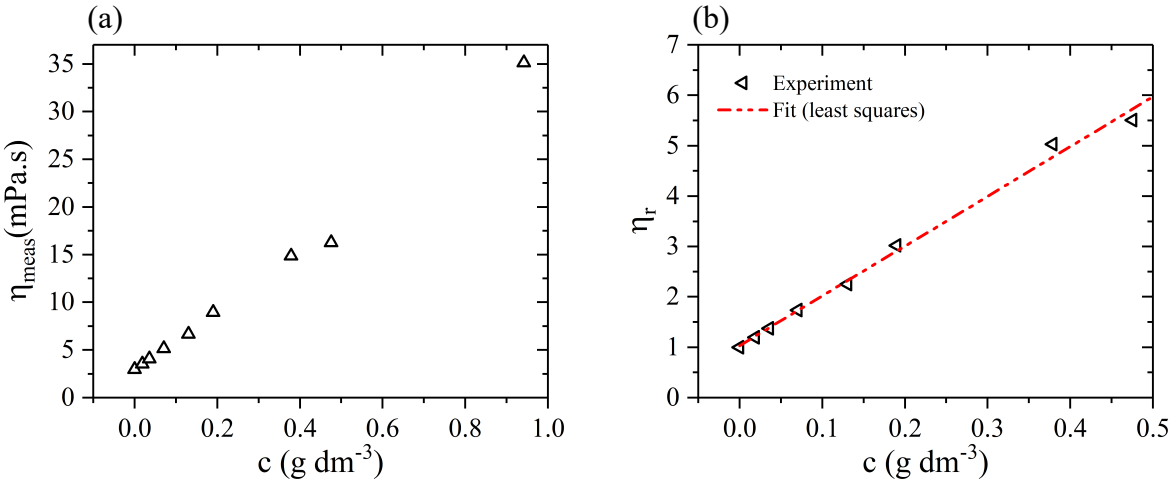


Figure 3.4: (a) The measured viscosity as a function of polymer concentration in comparison to the relative viscosity (b).

move any measurable distance on an experimental time scale.

The diffusion coefficients recorded in Figure 3.3 (b) were converted to measured viscosities, η_{meas}, using Equation 3.8. Here, the temperature and particle diameter were fixed and all other parameters are constant. These results are summarised in Table 3.2 along with the associated Brownian time, τ_B, which shows the expected increase as a function of polymer concentration. The relationship between polymer concentration and measured viscosity is shown in Figure 3.4 (a). At a xanthan concentration of 0.00 $g\ dm^{-3}$, the measured viscosity, $\eta_{meas} = \eta_s = 2.91\ mPa.s$, is that of the pure solvent mixture and is the same order of magnitude as reports in the literature of 1.74 $mPa.s$ [91] for this solvent mixture, at the composition ratio used in these experiments. Whilst the absolute value does differ from the literature, an increase of η_{meas} was expected due to particle-wall effects, hydrodynamic considerations and Faxén's correction [92]. Particles diffusing close to a surface slow down due to hydrodynamic interactions and an increase in the drag coefficient results. In order to confirm this, we calculate these effect using Faxén's correction for the translation drag coefficient in the parallel direction to the bottom cell wall

$$\zeta^{||} = \frac{\zeta}{1 - (9/8)(a/h) + (1/8)(a/h)^3}, \tag{3.10}$$

where ζ is the Stokes' drag coefficient, h is the particle's distance from the bottom cell wall and a the particle's radius. Here we estimate the particle height from the cell wall to be 100 nm, the approximate Debye length for this system, and a particle radius of 3 μm. We use the literature

value of 1.74 $mPa.s$ for the solvent viscosity. This results in a adjusted solvent viscosity of $\eta_s = 3.00\ mPa.s$ which is in good agreement with our measured value of $\eta_s = 2.91\ mPa.s$. If the height is taken to be 250 nm, then a corrected value of $\eta_s = 2.91\ mPa.s$ is found, which is in excellent agreement with our experimental observations. However, as the $\eta_r = \eta_{meas}/\eta_s$ is used for further calculations these hydrodynamic effects can be neglected anyway. Whilst the results in Figure 3.4 (a) show the relationship between polymer concentration and absolute viscosity, the relative viscosity, 3.4 (b), provides a dimensionless measure of the polymer's effect on the solution's viscosity.

By fitting to the data shown in Figure 3.4 (b), the intrinsic viscosity was determined by using a least squares fit, represented by the dashed red line. In the low concentration limit, the relative viscosity is expected to show a linear relationship with respects to the polymer concentration in accordance with Equation 3.7 and our results appear to agree with this prediction. We note the omission of polymer concentration C8 (see Table 3.2), due to the significant jump in concentration between it and C7 as well as its poor statistics due to the low number of experimental repeats. From this fit, we find an intercept value of 1.03 and a slope, which corresponds to the intrinsic viscosity, of $[\eta] = 9.88\ dm^3\ g^{-1}$. However, whilst this traditional approach is considered effective for non-polyelectrolytes and screened polyelectrolytes in high concentration salt solutions, reports of polymer-polymer effects in low salt solutions have been reported in the literature [72, 82] leading to inaccurate measurements when using this method. As the polymer solvent mixture presented here had no additional salt added, it is considered to be in this low salt regime.

In order to determine the $[\eta]$ of a polyelectrolyte i.e. xanthan in low concentration salt solutions, the reduced viscosity, $\eta_{red} = \eta_{sp}/c$, is often investigated as a function of polymer concentration. As the concentration of polyelectrolyte is reduced, an apparent increase in η_{red} should result as $c \to 0$. This is thought to occur as a reduction in electrostatic screening of polymer chains results from a significant drop in concentration of dissociated ions from the polymers themselves. This leads to an expansion of the polymer coils and a longer isolated polymer coil to polymer coil interaction range [82]. In our studies, we did not observe this behaviour and a linear relationship between η_{red} and c was found. However, the results presented here include a concentration range far larger than those previously reported, but with limited data sets C_0, C_1 and C_2 falling within the polymer concentration domain considered in those

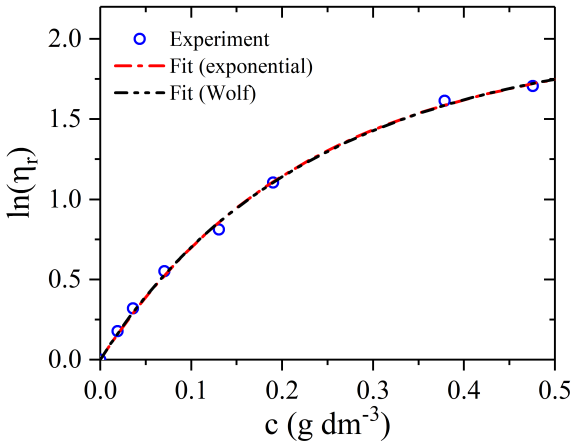


Figure 3.5: The log of the relative viscosity plotted as a function of polymer concentration. Experimental results are open blue symbols and fits using the Equation 3.11 and Equation 3.12 are the dashed black and red lines, respectively.

studies [72]. As such, better statics and more measurements in this low concentration region may be required before these effects become apparent. The results presented here are also for a xanthan sample with a different molecular weight, dissolved in a different solvent mixture.

Therefore, we continue on the basis that we are studying a polyelectrolyte at low salt concentrations and analyse the results using an advanced technique proposed by Bernhard A. Wolf [82], which takes into account the unique behaviour often observed in this type of low salt polyelectrolyte solution. We perform two different fits to our data (Equation 3.11 and Equation 3.12) using this method in order to compare and contrast these results to those determined using traditional methods (Figure 3.4 (b)). All results are summarised in Table 3.3.

Due to the charge effects described above, the use of only two parameters in traditional methods to describe the relationship between η and c is thought to be insufficient. Therefore, an additional parameter, $[\eta]^{++}$, is introduced which accounts for the contraction of polymer coils once the ionic strength of the solution increases sufficiently and effective screening occurs. At this point $[\eta]$, which varies at low polymer concentrations, becomes constant and is subsequently represented by $[\eta]^{++}$. An exponential transition between these two limiting values is assumed where $P = ([\eta] - [\eta]^{++}/[\eta])$ is introduced to represent the magnitude of this transition as well as, A, which defines the composition range over which it occurs. The solution to this yields the

Fit method	Least squares		Exponential		Wolf	
Fit range	$c >> c^*$	$c < c^*$	$c >> c^*$	$c < c^*$	$c >> c^*$	$c < c^*$
$[\eta](dm^3\ g^{-1})$	9.88	10.44	8.98	9.96	8.71	9.95
$c^*(g\ dm^{-3})$	0.101	0.096	0.111	0.100	0.115	0.101
$R_g(nm)$	260	265	252	260	249	260

Table 3.3: A summary of polymer properties and dimensions determined by the three fitting methods, Least squares, Exponential and Wolf. Each fit was performed over the dilute and semi-dilute polymer regimes, as well as the dilute only.

expression

$$\ln(\eta_r) = A(1 - e^{\frac{Pc[\eta]}{A}}) + (1 - P)c[\eta] \tag{3.11}$$

and we refer to this as the Exponential fit. Although Equation 3.11 is known to describe experimental results well [72, 82], its physical significance is limited, whereas

$$\ln(\eta_r) = \frac{c[\eta] + Bc^2[\eta][\eta]^*}{1 + Bc[\eta]}, \tag{3.12}$$

which results from integrating an expansion of the Huggins equation (a form of Equation 3.3), does have physical significance. Here, B is a fitting parameter and $[\eta]^*$ is the specific characteristic hydrodynamic volume. We refer to this as the Wolf fit. As both methods have been reported to work well, each is applied to our work. Both fits were performed over two polymer concentration regimes to compare and contrast the results. The first encompass all data points shown in Figure 3.5 and correspond to the dashed red line, Equation 3.12, and dashed black line, Equation 3.11. These fits included the dilute and semi-dilute polymer regimes. The second fits were performed from C_0 - C_3 and constitutes only the dilute regime. In this instance fit lines have been omitted from Figure 3.5 for clarity, but the results are reported in Table 3.3,

As described in Section 3.2.1, the concentration at which polymer coils start to touch and reach their maximum packing fraction is referred to as the overlap concentration, c^*. From $[\eta]$, via the relationship $c^* = 1/[\eta]$, the overlap concentration for this polymer under the experimental conditions described was calculated for each set of fit results. From this, the polymers R_g was determined using Equation 2.17, where $c^* = 3\bar{M}_W/4\pi R_g^3 N_A$ and provides a rough estimate. This was possible as the M_w for this analytical grade xanthan sample, supplied by Sigma-Aldrich, was quoted to be $4.5 * 10^6 g\ mol^{-1}$ and advertised as having a narrow M_w distribution.

Table 3.3 summarise these results. To our surprise, the three methodologies described here yielded almost identical results, with variations on the order of 10 nm when considering the polymer's R_g. The least squares fit, over the entire concentration range, resulted in lower c^* than either of the advanced Wolf methods and therefore a larger R_g, by approximately 10 nm. Both the Exponential and Wolf fits differed from one another by far less, on the order of 3 nm. When considering only the dilute concentration regime, all methods resulted in a reduction of c^* and in increase in R_g. In the case of the least squares fit, this change was on the order of 5 nm, where as a change of approximately 10 nm was found for both of the advanced Wolf methods. In the dilute regime, both of advanced Wolf methods appear to converge, with a $c^* = 0.10\ g\ dm^{-3}$ and $R_g = 260\ nm$ both of which agree with the results of the least squares method when considering the full concentration range. However, we caution that in the Zimm model, the relationship between intrinsic viscosity and the radius of gyration is $[\eta] = 0.425 N_A R_g^3 / M_w$ which would change the value of the radius of the measured gyration by a factor of two. But, in the case of polyelectrolytes, whether this treatment should be applied or is valid, is unclear. Assuming the xanthan in this solvent mixture, which is not a theta solvent but a good solvent, is in a rigid chain conformation, a Mark-Houwink exponent of $\alpha = 1.14$ is used [72]. Therefore, the Mark-Houwink prefactor, K_w, was found to be $1.7 * 10^{-7}\ dm^3\ g^{-1}$, by rearranging Equation 3.6 and inserting an averaged value of the Exponential and Wolf fit of $[\eta] = 9.96\ dm^3\ g^{-1}$ and known molecular weight of $4.5 * 10^6 g\ mol^{-1}$. This agrees well with previous reports in the literature [72]. In future work, this value of K_w can be used to determine the molecular weight of previously uncharacterised xanthan samples, by way of Equation 3.6, in the same solvent system, using the methods reported here.

3.5 Conclusions

In conclusion, the intrinsic viscosity of a low salt xanthan solution has been measured using a combination of passive microrheology and low concentration polyelectrolyte rheological theory. Analysis of the rheological data was completed using both a traditional and advanced Wolf method. From this, the overlap concentration and radius of gyration for this solvent mixture and xanthan sample have been calculated. The reported increase in reduced viscosity was not found at low polymer concentrations, using our approach, as previously reported in the literature. However, the reasons for this difference have been proposed. Finally, the Mark-

Houwink prefactor, K_w, for this solvent mixture was found which will allow a xanthan sample of unknown molecular weight to be characterised using the same solvent system and methodology in the future.

Chapter 4

Measuring the pair potentials in colloid-polymer solutions

ABSTRACT

In this chapter, the depletion interaction between pairs of superparamagnetic colloidal particles is measured by combining bright-field microscopy, optical tweezing and custom image analysis techniques. Optical tweezers are used to bring two particles into contact and once switched off, particle trajectories are recorded as a function of time. From these data, a survival probability is determined by measuring the time taken for particles to reach a separation distance threshold. The depletion interaction is tuned by adjusting the concentration of non-adsorbing polymer. At high polymer concentrations, the Brownian time and interaction strength of these systems is such that particles no longer separate and diffuse on an experimental time scale. Therefore, several experiments are conducted with an applied magnetic field, inducing an interparticle repulsion, which allows this regime to be probed. The experimentally determined survival probabilities are compared to theory. We find that at low polymer concentrations, the AOV model describes the experimental results well. At higher polymer concentrations, where a separate magnetic interaction has been used, the escape probabilities are not as well described.

4.1 Introduction

Understanding the type and strength of interparticle interactions present in colloidal systems is fundamental to predicting their stability, dynamics and phase behaviour. As discussed in Section 2.1.3, the presence of polymer in colloidal systems can result in several outcomes depending on the characteristics and traits of the specific system in question. A polymer's affinity for surface adsorption underlies the macroscopic behaviours of these systems. If the polymer is non-adsorbing, a depletion interaction results. Historically, determining the range and strength of the depletion interaction has been challenging due to a combination of the technical limitations of previous experimental techniques, the short range nature and large domain of interaction strengths possible. However, several approaches are reported in the literature, each with their own strengths and weaknesses.

Surface Force Apparatus [93], Atomic Force Microscopy [94] and Total Internal Reflection Microscopy [95, 96] have all been implemented in order to measure the strength and range of depletion interactions. However, these approaches tend to necessitate artificial model systems, which differ considerably from the real world colloidal conditions found in nature or commerce. Optical tweezers [97–100] have also been used, but direct measurements of short range interactions have historically been problematic due to beam interference and image analysis errors. Compelling evidence of the latter has been discussed at length in the literature [101, 102] and highlights the importance of taking these considerations into account [103]. All of the approaches mentioned are considered to be direct measurements of depletion forces. As such, indirect measurements may provide an alternative approach to overcoming the aforementioned issues in depletion potential measurements.

Here we present an indirect method for measuring pair potentials in depletion systems. We measure the survival probability of two superparamagnetic particles, which start in contact, separate and subsequently diffuse until a cut-off distance is reached, for three polymer concentrations. These include two in the dilute and one in the semi-dilute regime. For both regimes we characterise the effects of interparticle separation, with and without an applied magnetic field. Controlled application of this magnetic field causes a repulsive interaction between particles and leads to their separation. Results from the dilute system without a field are directly compared to those where a field has been applied. In the case of the semi-dilute system, application of

an external magnetic field is necessary, as passive particle separation has a low probability of occurring over any sensible experimental time scale. This is due to the depth of the potential energy well in the semi-dilute polymer regime. All results are compared to theoretical calculations from survival probability theory, where we have used the simplest type of depletion model, namely the AOV potential. This novel approach has several advantages over previous methods, including its generality. It has the potential to be applied to other types of colloidal systems with differing interparticle interactions and is not solely limited to investigation of the depletion interaction.

This chapter is presented in the following manner. Section 4.2 describes the survival probability theory for two particles, initially in contact, separating and diffusing away from each other until a distance threshold is reached. The link between survival probability and interaction potentials is also established. In Section 4.3, the experimental method is described, including sample preparation, experimental protocol and image analysis techniques. Finally, Section 4.4 examines and discusses the experimental results for all polymer concentrations investigated and draws comparisons between these results and those calculated using survival probability theory. The results and discussion section is broken down into two parts. First, experiments with a systematic increase in polymer concentration, but without an applied magnetic field, are considered, followed by results where an applied magnetic field has also been used. We end with a conclusion in Section 4.5.

4.2 Theory

The theory in this chapter was contributed by Adam Edward Stones, a DPhil student in the Aarts and Dullens groups at the Physical and Theoretical Chemistry Laboratory, the University of Oxford.

The time evolution of the radial separation $r(t)$ of two particles interacting with a potential energy $U(r)$ is given by the Langevin equation [104]

$$\zeta \frac{dr(t)}{dt} = -2\frac{dU(r)}{dr} + f_r(t). \tag{4.1}$$

Both the frictional and random forces acting on a Brownian particle are accounted for by the

drift,

$$\vec{F} = -\nabla U, \tag{4.2}$$

and noise terms, $f_r(t)$, respectively. The factor of 2 in Equation 4.1 appears as we are considering not one but two particles interacting with one another. The drag coefficient, $\zeta = 3\pi\eta\sigma$, arises due the viscous effects of the medium they are dispersed in. The noise term, $f_r(t)$, is a Gaussian random variable and captures the effects of random collisions of solvent molecules, with the following properties

$$\langle f_r(t) \rangle = 0 \tag{4.3}$$

and

$$\left\langle f_r(t) f n_r(t^{'}) \right\rangle = 2D\delta(t - t^{'}). \tag{4.4}$$

The diffusion coefficient is denoted as D and the delta function, δ, indicates the lack of correlation between solvent impacts on the particles at any one time when compared to another. In this instance, we are in the over-damped limit, so the inertia term does not appear in the Langevin equation.

The Fokker-Planck equation describes the time evolution of the probability density for a Brownian particle. In principle, the time dependence given by the Langevin Equation 4.1 could be used to derive the corresponding Fokker-Planck equation [105] for the scenario described above. If solved, subject to the initial conditions that two particles are at $r = r_0$ at $t = 0$, it would yield the full spatio-temporal probability distribution, $P(r, t|r_0)$, which could provide a full description of the particles' stochastic motion. However, measuring $P(r, t|r_0)$ experimentally is challenging, as it requires a large number of individual trajectories to obtain sufficient statistics. Furthermore, spatial resolution is limited, since measuring the probability of two particles having a separation r at time t would require a binning procedure. An attempt to increase the spatial resolution using smaller bin sizes would lead to poorer statistics.

An alternative approach is to consider the probability that the particles remain separated by a distance smaller than a predetermined maximum separation distance defined here as the

cut-off distance, d, for up to and including a time t. This approach draws parallels with a 'mean first passage' problem or 'Kramer's escape' problem [106]. We refer to this as the survival probability, $G(r_0, t)$, and it is given by

$$G(r_0, t) = \int_{r_0}^{d} P(r, t \mid r_0)\, dr, \tag{4.5}$$

where r_0 is the initial interparticle separation. In this instance, $r_0 = \sigma$, i.e. the initial separation is a particle diameter and the particles are in contact. Such a description leads to the additional boundary condition

$$P(d, t \mid r_0) = 0, \tag{4.6}$$

required to solve the Fokker-Planck equation. This condition removes trajectories which have reached the cut-off distance.

We instead note that $G(r_0, t)$ satisfies the Kolmogorov backward diffusion equation [107] such that

$$\frac{\partial G}{\partial t} = -\frac{2}{\zeta}\frac{dU}{dr_0} \bigtriangledown_{r_0} G + D \bigtriangledown^2 G. \tag{4.7}$$

We assume that the particles only translate in two dimensions and therefore G only depends on their separation. Hence,

$$\bigtriangledown^2 G = \frac{1}{r_0}\, \frac{\partial}{\partial r_0} \left(r_0\, \frac{\partial G}{\partial r_0} \right), \tag{4.8}$$

such that

$$\frac{\partial G}{\partial t} = \left(\frac{D}{r_0} - \frac{2}{\xi}\frac{dU}{dr_0} \right) \frac{\partial G}{\partial r_0} + D\frac{\partial^2 G}{\partial r_0^2}. \tag{4.9}$$

To enable comparison of data from different experiments, where D is an intrinsic property of the system under study, this equation is rewritten in terms of the following dimensionless variables

$$r_0^* = \frac{r_0}{\sigma}, \quad r^* = \frac{r}{\sigma}, \quad d^* = \frac{d}{\sigma}, \quad t^* = \frac{Dt}{\sigma^2}, \quad U^* = \frac{U}{k_B T}. \tag{4.10}$$

In colloidal systems, the variables, D, r and t, are easily determined. The partial differential

equation (PDE) thus becomes

$$\frac{\partial G}{\partial t^*} = \left(\frac{1}{r_0^*} - 2\frac{dU^*}{dr_0^*}\right)\frac{\partial G}{\partial r_0^*} + \frac{\partial^2 G}{\partial r_0^{*2}}. \tag{4.11}$$

Equation 4.11 is then solved subject to the initial conditions

$$G(r_0^*, 0) = \begin{cases} 1 & r_0^* < d^* \\ 0 & r_0^* \geq d^* \end{cases} \quad \text{and} \quad G\left(d^*, t^*\right) = 0, \tag{4.12}$$

and the reflective boundary condition

$$\frac{\partial G}{\partial {r_0}^*}\Big|_{{r_0}^* = 1} = 0, \tag{4.13}$$

which is due to the description of the particles as hard disks with a contact separation of σ. The experimental pair potential is modelled as

$$U^*(r) = U^*_{HS}(r;\sigma) + U^*_{dep} + U^*_{mag}, \tag{4.14}$$

where the hard-sphere interaction is accounted for by the reflective boundary condition in Equation 4.13. Therefore, only $U^*_{dep} + U^*_{mag} = U^*_{ex}$ needs to be considered when solving the PDE, Equation 4.11. From Section 2.1.2, Equation 2.12, the magnetic interaction potential is given by

$$U^*_{mag}(r^*) = \frac{\zeta}{2(r^*)^3} = \frac{m_c}{r^{*3}}. \tag{4.15}$$

When the particles are in contact, the non-dimensional interaction parameter, m_c, is given by

$$m_c = \frac{\pi\sigma^3\chi^2 B^2}{144 k_B T \mu_0}, \tag{4.16}$$

where $2a = \sigma$. The AOV model from Section 2.1.2 is used to model the attractive depletion interaction such that

$$U^*_{dep}(r^*) = \begin{cases} -d_c\left[\frac{(1+q-r^*)^2(2+2q+r^*)}{q^2(3+2q)}\right], & 1 \leq r^* \leq 1+q, \\ 0 \qquad\qquad\qquad , & r^* > 1+q, \end{cases} \tag{4.17}$$

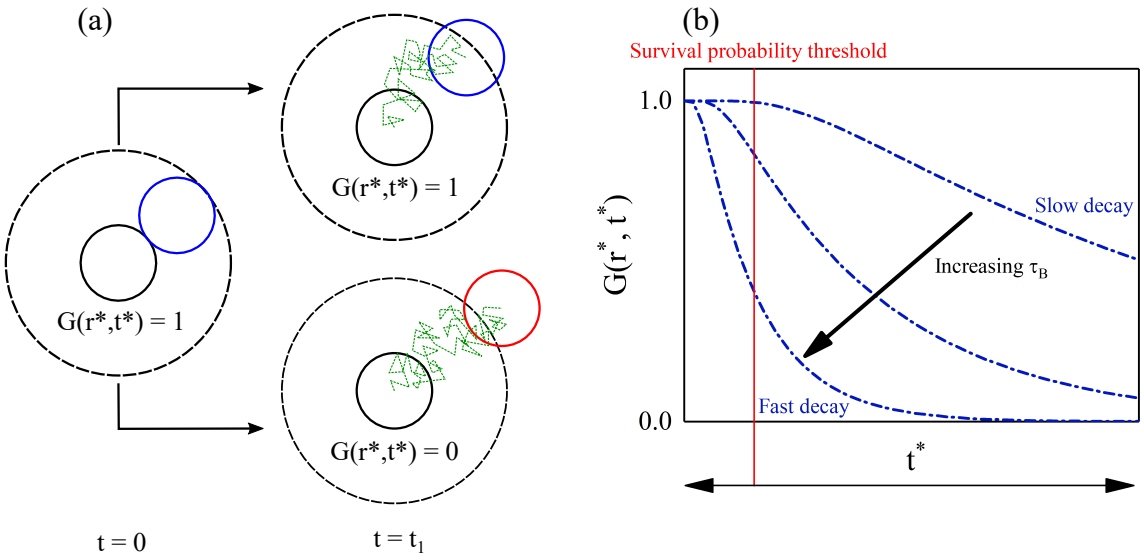


Figure 4.1: (a) shows the two possible outcomes at the end of the experiment. Particles have either separated and diffused past the cut-off distance threshold or they have not. The schematic is valid for one experiment, but in reality, $G(r^*, t^*)$ is determined by an ensemble of experiments. (b) Illustrates a typical survival probability plot using theoretical calculations for a hard sphere system where $U(r > \sigma) = 0$. The survival probability threshold is the point at which the first pair of (theoretical) particles have split and reached a separation equal to a specified cut-off distance, d.

where the colloid polymer size ratio $q = R_g/\sigma$ and the depletion well-depth, d_c, is given by

$$d_c = \frac{\pi}{12} n_b \sigma^3 q^2 (3 + 2q). \tag{4.18}$$

The expressions for U^*_{mag} and U^*_{dep} are then differentiated and substituted into Equation 4.11, which can in turn be solved numerically.

Experimentally, the survival probability, $G(r^*, t^*)$, is determined in the following way. Two particles are trapped and brought into contact (see Figure 4.1 (a) $t = 0$). They are held in position for 10 s, after which the traps are switched off. The particle are then left to diffuse away from each other for a fixed period of time equal to $2\tau_B$, where τ_B is the Brownian time. During this time, the particle positions are recorded and their trajectories determined using a post-experiment image analysis method discussed below. During analysis, a cut-off distance is defined. In this example we used a single cut-off distance, but in reality multiple cut-off distances are used. Once the diffusion time of $2\tau_B$ has elapsed, one of two outcomes are realised. Either the particles separated and diffused apart crossing the cut-off distance threshold (see Figure 4.1 (a) bottom), or they do not (see Figure 4.1 (a) top). The time at which the particles first

cross the cut-off distance threshold is recorded and their contribution to $G(r^*, t^*)$ calculated. The experiment is repeated numerous times. The exact technical details of the experimental protocol are described below. Once the desired number of experiments has been performed, all times at which particles cross the cut-off distance threshold are collated and the final $G(r^*, t^*)$ is calculated. Figure 4.1 (b) shows an example plot of $G(r^*, t^*)$ using theoretical calculations for a hard sphere system where $U(r > \sigma) = 0$. The survival probability threshold is the point at which the first pair of (theoretical) particles have split and reached a separation equal to a specified cut-off distance, d.

When measuring the depletion interaction in this manner, the particle-surface depletion interaction can be neglected as the downward force generated can be considered equivalent for all particles. Therefore, this effect is uniform throughout the sample. In this respect, it can be considered analogous to the downward force the particles experience due to gravity. Therefore, only the orthogonal component of the depletion interaction between two particles need be considered as the value of q for this colloid-polymer mixture means it is essentially a pair wise additive system.

4.3 Experimental method

Glossary of terms

Specific technical terminology is used throughout the following sections and are defined as follows.

Cycle One entire sequence of the experimental protocol including tracking and trapping of the particles, bringing them into contact, holding them in position for a specified time and the specific time they were free to diffuse before the next cycle was repeated.

Run The specific cycle step where particles were allowed to diffuse. Image analysis was performed on these image frames to determine the particle trajectories and subsequently their separation distance.

Sample A specific colloid-polymer or colloid-solvent mixture.

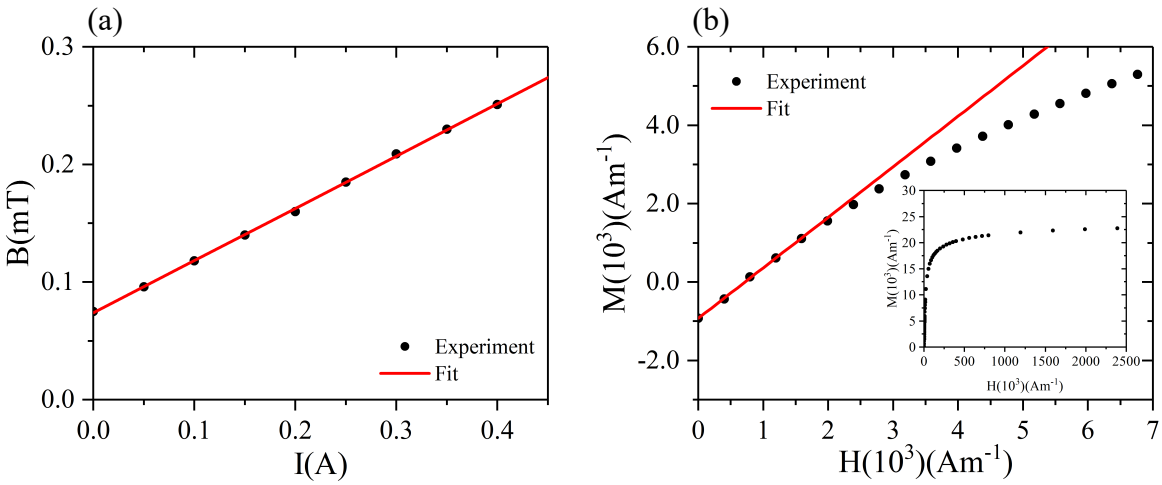


Figure 4.2: (a) Magnetic field strengths recorded at the sample cell's location on the optical tweezing setup. Symbols are measured values and the solid red line is a fit to these data. (b) SQUID measurements used to determine the volume magnetic susceptibility of the superparamagnetic particles. Symbols are measured values and the solid red line is a fit to these data. The inset (b) shows their response over the entire domain of applied field strengths.

System Collective term used for all colloid-solvent and colloid-polymer mixtures at a specific polymer concentration.

4.3.1 Sample preparation

Quasi-2D colloid-polymer mixtures were prepared with particle area fractions of < 0.01 using superparamagnetic particles with a diameter of $\sigma = 3.0\ \mu m$, as described in Chapter 2, Section 2.2. The polymer concentrations investigated were prepared using the xanthan solutions described in Section 2.2.1, the details of which are summarised in Table 4.1. A non-polymer system was also prepared using the same superparamagnetic particles dispersed in the stock deionised water/ethanol solvent mixture.

4.3.2 Magnetic susceptibility

The applied magnetic field and bulk magnetic susceptibility of superparamagnetic particles were measured in order to evaluate the magnetic component, $U_{mag}(r)$, of the overall interaction potential. These results are shown in Figure 4.2 (a) and (b) respectively.

The results shown in Figure 4.2 (a) show an increase in measured field strength as a function

of supplied current to the field generating coil. By fitting to these data, it was determined the optical trapping setup had a residual magnetic field of $0.078 = mT$ when the probe was placed at the centre of microscope stage where the sample cell was located during experiments. The field was orientated orthogonal to sample cell's xy plane.

This residual field was due to experiments performed by previous DPhil students whose work was the primary purpose for constructing the setup. As there was neither the time or resources to build a dedicated optical tweezing setup for this work, the presence of a residual field was unavoidable. In an ideal world, a dedicated setup would have been constructed to avoid such field effects. However, as the residual field was measured and characterised any effects were subsequently considered in the analysis of all results.

Plot (b) shows the results from superconducting quantum inference device (SQUID) measurements which were used to determine the volume magnetic susceptibility of the particles over the region of linear response. By fitting these data (solid red line), it was determined that the dimensionless volume susceptibility constant, χ, was 1.29. The inset of Figure 4.2 (b) show the particles' response over the entire range of applied fields. The plateau at high field strengths indicates saturation was achieved.

4.3.3 Determination of Brownian time

To determine the Brownian time of each sample, bulk MSD experiments were conducted using a UCPlanFLN 40× magnification 0.70 infinity/0-1.6/FN22 Olympus objective mounted on an Olympus CKX41 inverted microscope. Images were captured at 100 ms intervals using a Ximea MQ042MG-CM camera. Particle coordinates were determined using the methods described in Chapter 2 Section 2.2.3. The MSD for each sample was measured a maximum of 7 times, in different locations of the sample cell, for 15 minutes at a time. For each polymer concentration, the diffusion coefficient was determined using a least squares fit to the averaged mean squared displacement data for all experiments at the specified concentration. The fits were performed over a range of 1000 data points, equivalent to 100 s, starting at $t = 0$. Each sample's Brownian time was calculated using Equation 2.1. The Brownian time for each polymer concentration is reported in Table 4.1.

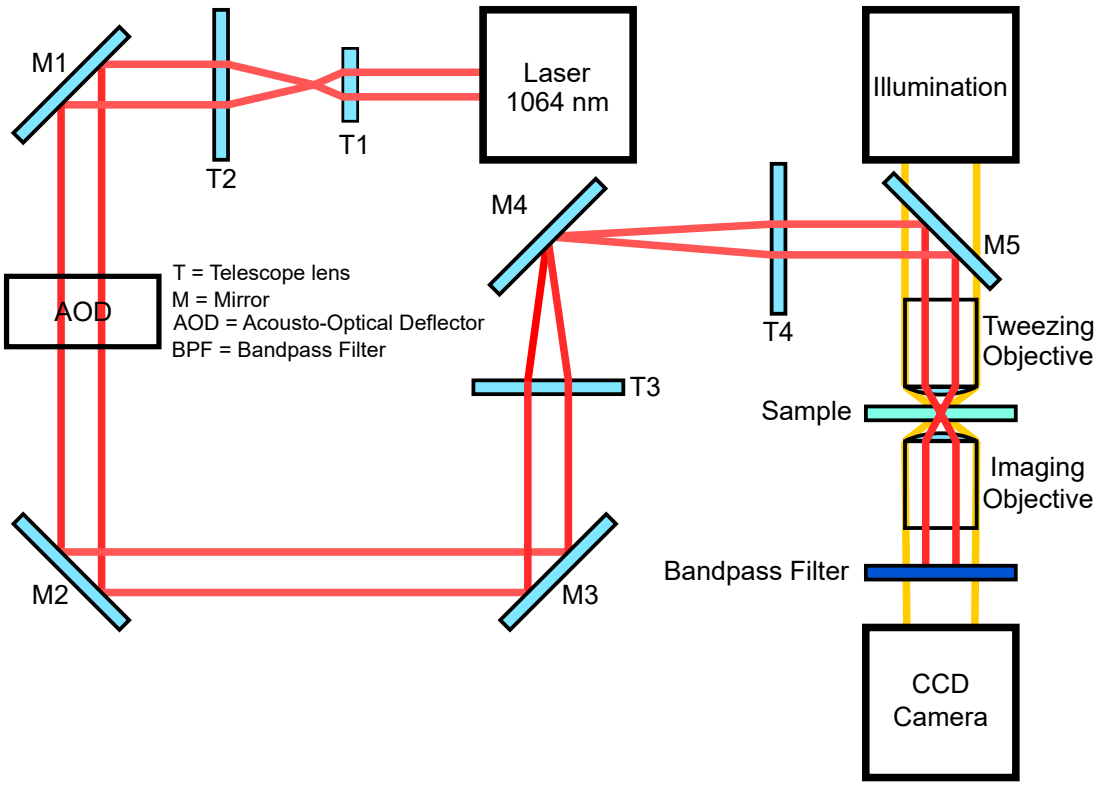


Figure 4.3: Schematic of the optical tweezing setup used to perform experiments redrawn from [108]. The coil modification is omitted and the diagram is not to scale.

4.3.4 Optical tweezing setup

An existing optical tweezing set up was used to perform experiments [108]. A schematic is shown in Figure 4.3. Optical traps were generated and controlled using a acousto-optical deflector (AOD) coupled to a 1064 nm laser beam. After passing through the AOD, the beam was guided through telescopic lenses into the back aperture of a vertically mounted Leica 50× magnification (NA = 0.50) objective. An illumination light source was also passed through and focused by the same objective. The transmitted light was then refocused by a second vertically mounted imaging objective, 40× magnification (NA = 0.50) and directed onto a Ximea MQ042MG-CM camera. A bandpass filter was used to protect the camera from exposure to the laser light. The AOD was controlled using a combination of LabVIEW and Aresis software.

Small modifications were made to the existing hardware in order to allow experiments with an applied magnetic field to be performed. A wire coil was inserted just above the sample stage and connected to a power supply unit. This was in turn attached to a function generator to

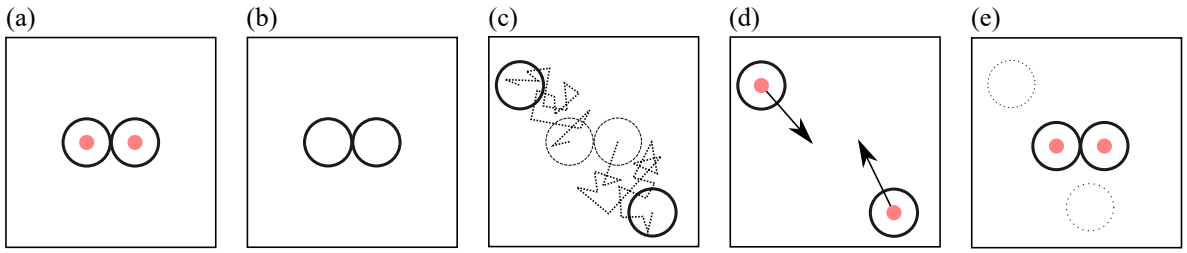


Figure 4.4: A summary of the experimental protocol for diffusion experiments with and without an applied magnetic field. Red dots signify the position and state (on or off) of optical traps, solid circles represent particle positions and dotted circles their previous position.

which a USB connection could be made between it and a control computer running LabVIEW software. Extensive modifications were made to the tweezing software in order to create an semi-autonomous experiment, the details of which are described below. This allowed identical experimental cycles to be run in order to build up sufficiently large data sets. A gaussmeter was used to characterize the field strengths used in each experiment. The results of these measurements are shown in Figure 4.2 (a).

4.3.5 Experimental protocol

Specialised code, written in LabVIEW, was used to automate the experimental protocol. Automation included real-time tacking of particles using an inbuilt circle tracking algorithm, control of the trap positions, their states (on or off), the applied magnetic field strength and the frame rate at which images were recorded. Figure 4.4 shows each of these instances in sequence for a single experimental cycle. The cycle was broken down into successive steps as follows; (a) particles were brought into contact and positioned at pre-determined starting coordinates using two optical traps. Particles were held at this position for 10 s to allow relaxation of the polymer solution. (b) traps were switched off. If applied magnetic field experiments were being performed, the applied field was switched on for $2\tau_B$ and particles were allowed to diffuse (c). For experiments without an applied magnetic field, particles were simply allowed to diffuse for $2\tau_B$ (c). In applied field experiments, after $2\tau_B$ the field was switched off and the particle tracking switched on. In experiments without an applied magnetic field, after $2\tau_B$, (c) the particle tracking was switched on. (d) two optical traps were created at the coordinates determined by particle tracking algorithm and used to return both particles to their starting positions (e). At

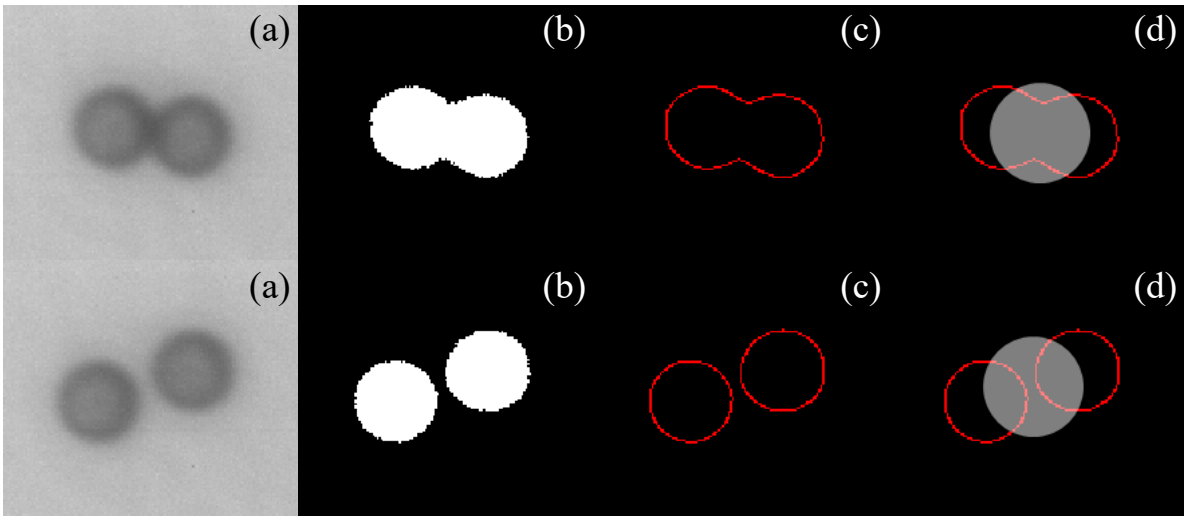


Figure 4.5: Example of the image analysis processing used for a particle pair in contact (top) and when separated (bottom). (a) captured raw image, (b) binarization using thresholding, (c) edge detection and (d) cropping of data points.

this point, the cycle was repeated, starting at step (a). Post-experiment image analysis was used to determine the particle coordinates in steps (b) and (c). All steps of the cycle were synchronized to within 0.1 ms ± 0.01 ms using the CPU's Kernel as a reference time. For each polymer concentration and field strength, the experimental cycle was run 250 times or more (except where stated otherwise) in blocks of 50 cycles ± 20, with a change of particles for each block to ensure no bias resulting from an anomalous particle pair.

4.3.6 Image analysis

The intrinsic optical limitations of the optical tweezing setup used necessitated the development of a custom post-experiment image analysis algorithm in order to determine each particle's xy coordinates as a function of time. Centre of mass calculations at short interparticle distances are notorious for resulting in an undesired bias in each particle's position [101, 102], resulting in an apparent interparticle distance smaller than their actual separation. Therefore, particle positions were determined using an algorithm based on edged detection similar to methods previously reported in the literature [109, 110]. Figure 4.5 shows the main steps of this process. The top row (a) - (d) shows the method applied to two particles in contact and the bottom row (a) - (d) for two particles that have separated. The following was performed at each step: the raw image data was imported (a) and binarized (b) using a thresholding function; next an

Sample name	concentration ($g\ dm^{-3}$)	ϕ_p	D (10^{-2})($\mu m^2 s^{-1}$)	$\tau_B(s)$
C_p0	0.000	0.00	5.29	42.52
C_p1	0.019	0.25	4.12	53.66
C_p2	0.037	0.48	3.58	70.48
C_p3	0.190	2.44	0.98	229.66

Table 4.1: Summary of the polymer concentrations used in each experiment and their associated properties.

edge detection algorithm was applied (c) and the centre point between each particle determined; using the centre point, a disk with a fix size equivalent to one particle diameter was created (d) and subtracted from (c). This resulted in two sets of pixel coordinates equivalent to two arcs, one for each particle. A fit was subsequently performed to each arc which provided the centre point of each particle in Euclidean space.

4.4 Results and discussion

This section is split into two parts. First, diffusion experiments without an applied magnetic field (Section 4.4.1) are discussed, followed by those with an applied magnetic field (Section 4.4.2). In both cases, systems with and without polymer were investigated. A total of four systems were studied, the specific details of which are summarised in Table 4.1. These included one system without polymer, referred to throughout as $C_p0 = 0.000\ g\ cm^{-3}$, and three systems with polymer. The three systems with polymer consisted of two at concentrations below the coil overlap concentration, c^*, and were considered to be in the dilute regime. These are referred to as $C_p1 = 0.019\ g\ cm^{-3}$ and $C_p2 = 0.037\ g\ cm^{-3}$. A final system, referred to as $C_p3 = 0.190\ g\ cm^{-3}$, was in the semi-dilute regime, where polymer coils are considered to overlap with one another. The coil overlap concentration reported in Chapter 3 was used to determine these two regimes. To compare results from different systems, particle trajectories were scaled according to two parameters; distances are in particle diameters, $\sigma = 3.0\ \mu m$, and t is expressed in units of Brownian time (see Section 4.3.3 and Table 4.1). As illustrated in Figure 4.1, we stress that scaling t by τ_B is important due to the shift it causes in measured survival probabilities.

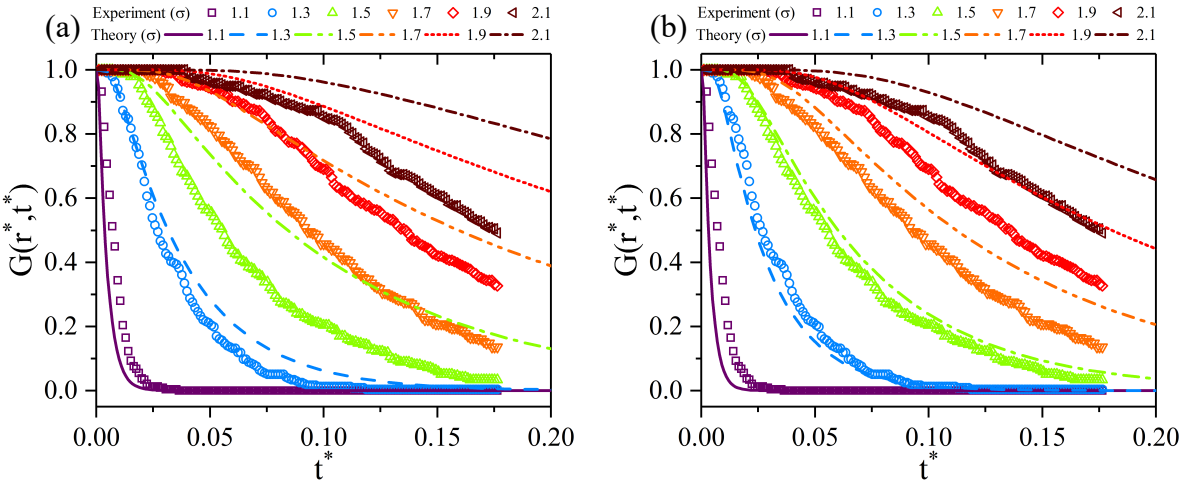


Figure 4.6: (a) Survival probability results for the experimental system, C_p0, (symbols) with no added polymer or applied magnetic field for different cut-off distances, d, as indicated in the graph. Superimposed lines are theoretical results assuming a HS interaction. (b) the same experimental results as shown in plot (a) with superimposed theoretical results (dashed lines) for a weakly repulsive pair interaction.

4.4.1 Separation and diffusion without an applied magnetic field

No polymer

First, we consider the simplest theoretical and experimental system, i.e. one without added polymer, C_p0 (see Table 4.1), and with no applied magnetic field. Figure 4.6 (a) shows the experimentally determined survival probabilities (SPs), $G(r^*, t^*)$, (symbols) and theoretical calculations (lines). The data set was composed of trajectories recorded from two different experimental samples, prepared several weeks apart. These two data sets were combined to create a single data set consisting of 236 individual runs. The independently measured τ_B for this system was 42.52 s. Experimental results were scaled accordingly.

In the first instance, particles were assumed to behave as hard spheres (HS) with an interaction potential $U(r > d) = 0$. The theoretically determined SPs for a HS system are plotted as dashed lines in Figure 4.6 (a). Cut-off distances of 1.1, 1.3, 1.5, 1.7, 1.9 and 2.1 were considered. Larger cut-off distances were not considered due to the lack of statistics (very low event frequency). While the data in Figure 4.6 (a) showed agreement with theory for the shortest cut-off distance of 1.1, deviations grew as the cut-off distance was increased. This was due to the presence of a residual magnetic field (see Figure 4.2 (a)) inherent in the optical tweezing

setup. To account for this, Figure 4.6 (b) shows the theoretical results (dashed lines) for a weak repulsive interaction, $U_{mag}(r)$, superimposed on the same experimental results. Once this repulsive term was introduced into the theoretical SP calculations, using the residual field value determined in Figure 4.2 (a), good agreement between experiment and theory was found for $d \leq 1.5$. At longer cut-off distances, the theoretical predictions overestimated the experimental results. The cause of this overestimation is not known, but hydrodynamic interactions could be responsible. All further theoretical calculations, unless stated otherwise, include the repulsive term caused by the optical tweezing setup's residual field.

With polymer

Next, we consider the effects of systematically introducing small amounts of polymer to the solvent mixture. The depletion interaction strength is estimated by comparing the experimental results with theoretical calculations for the SP using the AOV model and polymer concentration by mass. The experimental results (symbols) for two colloid-polymer mixtures with polymer concentrations of 0.019 $g\ dm^{-3}$ (C_p1) and 0.037 $g\ dm^{-3}$ (C_p2) are shown in Figure 4.7 (a)(b) and (c)(d) respectively. The experimental results of (a) and (b) were scaled using the sample's independently measured τ_B of 53.66 s. This scaling is in excellent agreement with the previously reported results summarised in Chapter 3, Table 3.2, for the same polymer concentration. The experimental results shown in (c) and (d) were scaled using a τ_B of 70.48 s, also in agreement with previous measurements for this concentration of polymer (see Table 3.2).

As before, the theoretical SPs are superimposed as dashed lines for the cut-off distances of 1.1 through to 2.1. For both (a)(b) and (c)(d) two sets of theoretical results were calculated. The first used a value of 250 nm as the polymer's R_g. This value was selected due to the conclusions drawn from Chapter 3. However, poor agreement between experiment and theory was found in (a) and to a greater extent in (c). Here, the calculated SPs appeared to overestimate the experimental SPs. When a value of 225 nm was used for both polymer concentrations C_p1 and C_p2, the theoretical results showed better correlation with the experimental results and good agreement was found. A R_g of 225 nm was chosen due to the results of a Monte Carlo fitting algorithm developed in-house. This smaller R_g value could be explained by the discussion highlighted in Chapter 3, whereby the R_g determined using mean squared displacement measurements is equivalent to measuring the hydrodynamic radius of the polymer and not its

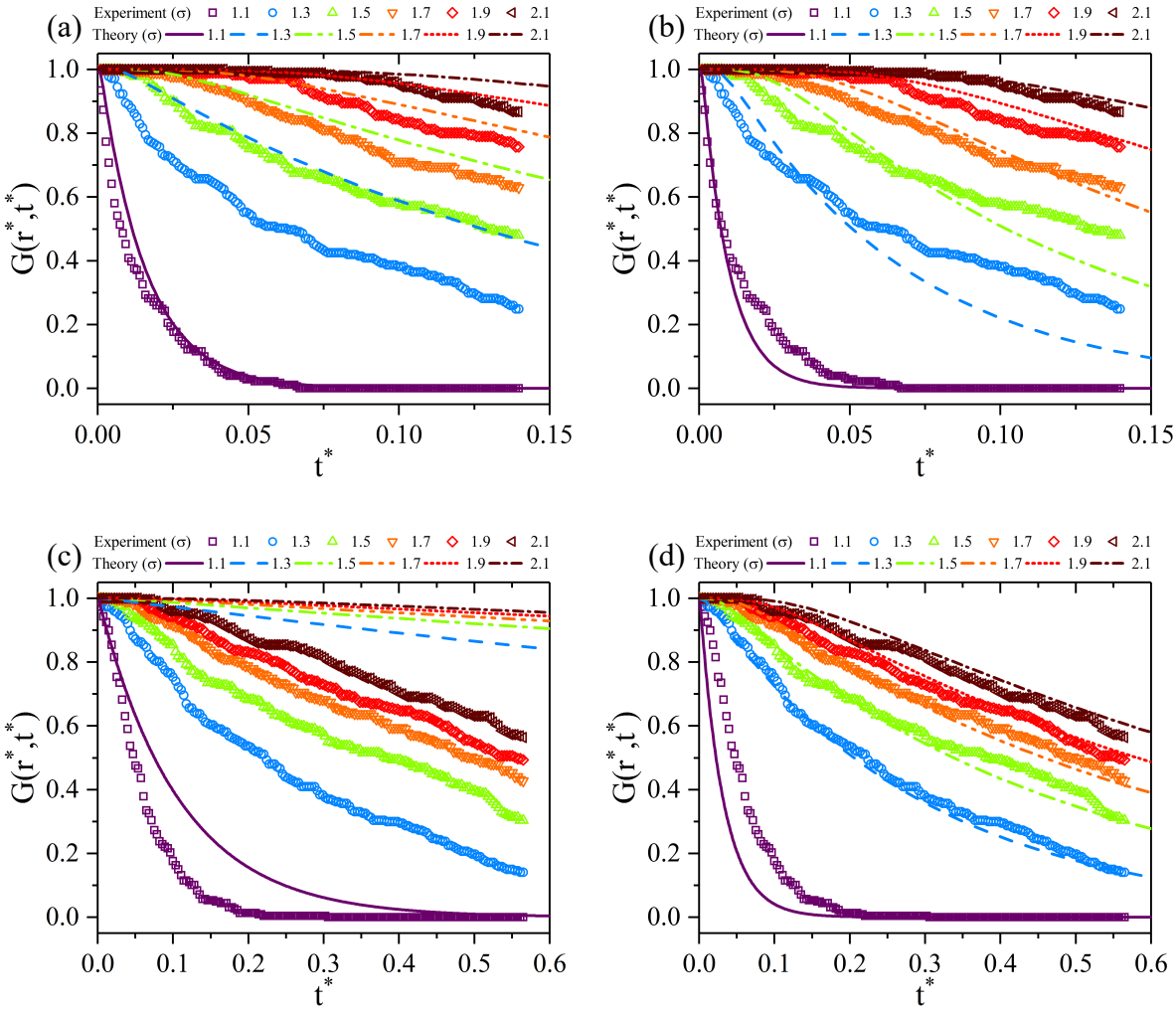


Figure 4.7: Plots (a)(b) and (c)(d) show the experimental SPs (symbols) for polymer concentrations of 0.0191 $g\ dm^{-3}$ and 0.0370 $g\ dm^{-3}$, respectively. Theoretical results are superimposed as solid lines. The theoretical results show in plots (a) and (c) were calculated using a polymer R_g of 250 nm where as for (b) and (d) a value of 225 nm was used.

true R_g. It is noted that whilst good agreement at all cut-off distances is apparent, the shape of the theoretical curves does differ somewhat from those seen in experiment. All calculated SPs included the weak repulsion term identified in Figure 4.6. In these calculations, the AOV model (Equation 4.17) was utilised to account for the attractive term of the interaction potential caused by the presence of polymer and the depletion interaction. The measured polymer concentrations and stated R_g values were incorporated into these calculations.

By comparing the experimental SP results of C_p0, C_p1 and C_p2 to those from theory, pair potentials for all three systems were estimated. The magnetic pair potential, $U_{mag}(r)$, caused by the presence of a residual field, was obtained via Equation 4.15 using the same values of χ and B

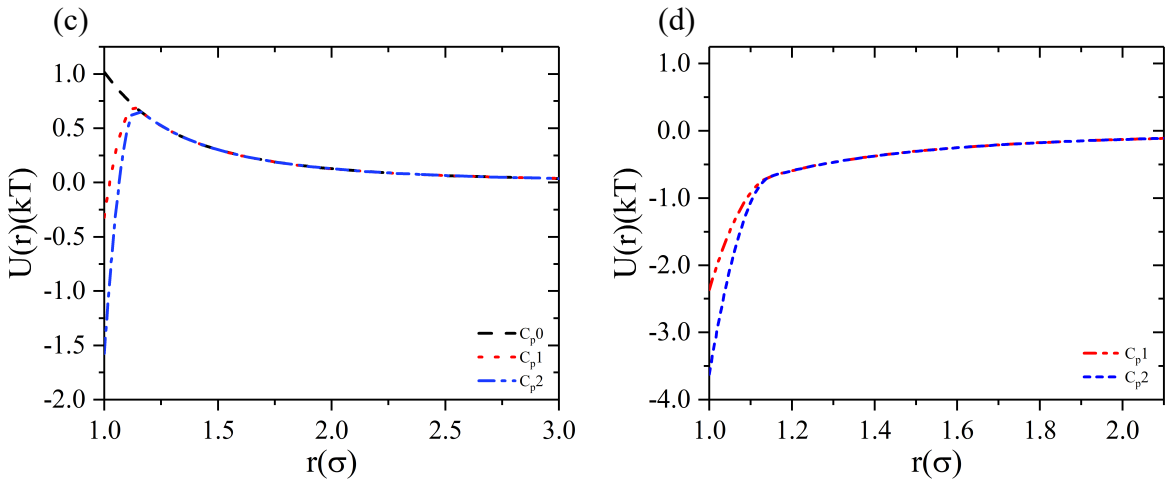


Figure 4.8: Figure 4.8 (a) shows the pair potentials (dashed lines) for C_p0, C_p1 and C_p2. The potentials of both C_p1 and C_p2 include the repulsive term determined from C_p0. (b) shows the total of both the repulsive and attractive terms.

used to calculate the theoretical SP results in Figure 4.6 (b). The net attractive potentials of C_p1 and C_p2 were then calculated using a combination of the repulsive term $U_{mag}(r)$ and depletion term $U_{dep}(r)$. The depletion term was obtained using the same AOV parameters determined by the theoretical SP results in Figure 4.7 (b) and (d), using a R_g of 225 nm and each sample's respective polymer concentrations. Adding the $U_{mag}(r)$ and $U_{dep}(r)$ terms for each polymer concentration, C_p1 and C_p2, resulted in the total interaction potentials, $U(r)$, shown in Figure 4.8. At contact, an interaction potential well depth of $-2.36\ kT$ was determined for C_p1 and $-3.62\ kT$ for C_p2.

Several known factors could have caused the relatively small disparities between SP experiments and theory. The AOV model is a simple approximation of the depletion interaction which does not take into the account polymer conformations or polymer-polymer interactions. Polymers are treated as ideal, but in reality polymer chains may not be in a random coil conformation and electrostatic repulsions, in conjunction with excluded volume effects, could cause significant differences between experimental results and those calculated using the AOV model. Secondly, the AOV model assumes particles are suspended in the bulk, surround by penetrable hard spheres, but in these experiments particles and polymer are close to a wall. Therefore, hydrodynamic interactions and other associated effects may also contribute to the observed deviations.

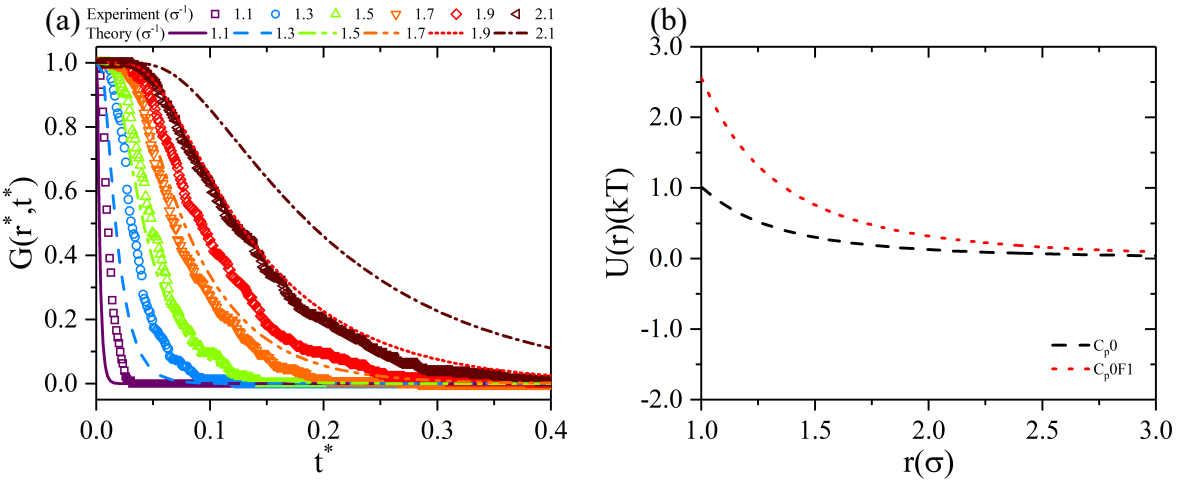


Figure 4.9: (a) experimental SP results of a system (C_p0F1) with no added polymer but with an applied magnetic field of 0.117 mT. Superimposed dashed lines are theoretical results. Plot (b) compares the pair potential determined from the residual field measurements against that of the applied magnetic field using the results shown in (a).

4.4.2 Separation and diffusion with an applied magnetic field

No polymer

Figure 4.9 (a) shows the SPs for a system with no added polymer and an applied magnetic field of 0.117 mT (C_p0F1). Symbols are experimental results and dashed lines are results from theory. As before, cut-off distances of 1.1, 1.3, 1.5, 1.7, 1.9 and 2.1 were considered. Excellent agreement between theory and experiment was found at a cut-off distance of 1.5. However, at cut-off distances < 1.5, the theoretical results appeared to underestimate the experimental SPs whereas at distances > 1.5 it overestimated them. Varying the field strength when calculating the theoretical SPs did not resolve these differences. However, as χ and B were known, $U_{mag}(r)$ for this experiment was still estimated and Figure 4.9 (b) compares the estimated pair potentials for C_p0 and C_p0F1. As expected, both the residual and applied magnetic field caused a repulsive interaction on the order of kT. Aside from the differences at short and long cut-off distances, both experiment and theory agree well with one another. The increase in interparticle repulsion is shown in Figure 4.9 (b) and provides a measure of the interaction strength caused by the residual and applied magnetic fields.

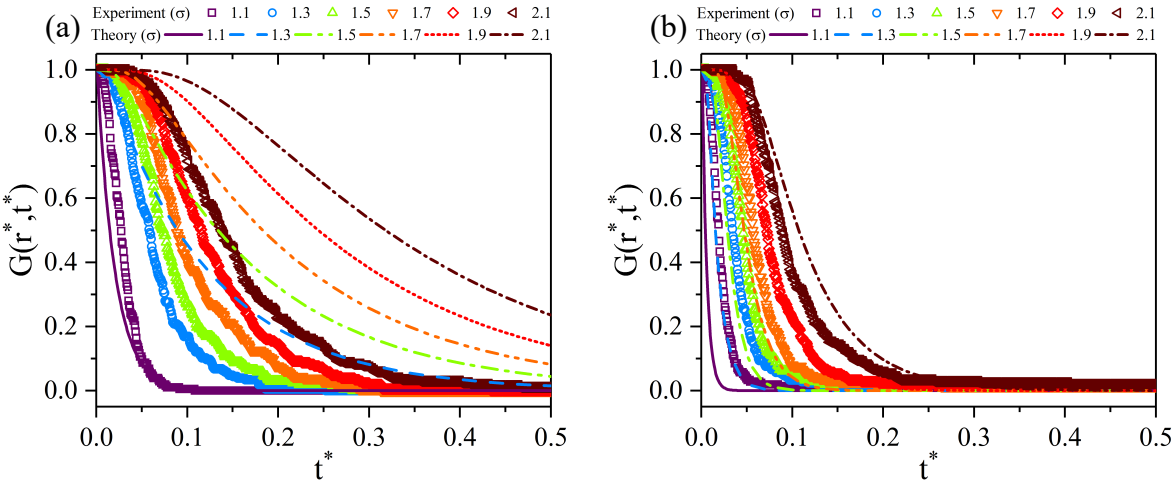


Figure 4.10: Plot (a) and (b) show the theoretical results (dashed lines) for a applied field strength of 0.117 mT and 0.207 mT respectively, superimposed on experimental results (symbols). A polymer concentration of 0.0370 $g\ dm^{-3}$ and R_g of 225 nm were used for both theoretical calculations.

With polymer

In order to determine the effects of an applied magnetic field on interparticle separation in the polymer solutions, field strengths of 0.117 mT and 0.207 mT were chosen to probe C_p2. These experiments are referred to as C_p2F1 and C_p2F2, respectively. The first field strength was chosen in order to make comparisons with C_p0F1. As a $R_g = 225\ nm$ appeared to show good agreement for C_p1 and C_p2, the same parameter was used when calculating the theoretical SPs for $C2F1$ and C_p2F2. Also, the same temporal scaling was applied as in C_p2. Figure 4.10 (a) and (b) show the experimental (symbols) and theoretical results (dashed lines) for C_p2F1 and C_p2F2, respectively. In the case of C_p2F1, the SPs for each cut-off distance are significantly overestimated, though agreement between theory and experiment was observed at the shortest cut-off distance of 1.1. Whilst it is not known what caused this, a simple temporal scaling using the system's measured τ_B may not be sufficient to model the real world behaviour of these polymer systems. It is well known solutions of xanthan are shear thinning (see Chapter 1). Because the force imparted by particles on the surrounding medium varies as a function of interparticle separation, driving particles through a polymer solution (see Figure 4.11 (a)) may lead to more complicated particle dynamics than our model accounts for. However, as the field strength was increased, better agreement between experiment and theory was found, with the general trends seen in experiments reflected in theoretical results. At a cut-off distance of 1.9,

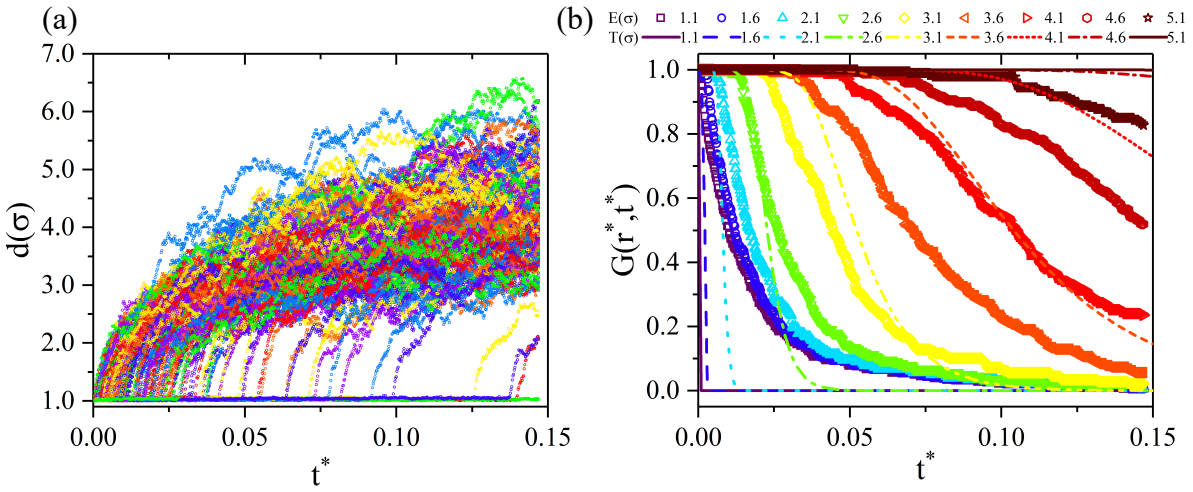


Figure 4.11: Plot (a) shows interparticle separations as a function of time. The driving effects of the applied field are clearly noticeable. (b) experimental (symbols) and theoretical results (superimposed dashed lines) for a applied field strength of 1.9 mT at a polymer concentration of 0.190 $g\ dm^{-3}$.

experiment and theory are in excellent agreement.

In order to test the limits of this technique, a polymer concentration of 0.190 $g\ dm^{-3}$ in combination with an applied field strength of 1.9 mT was investigated. The polymer concentration of this system, C_p3, was well above c^* at $\phi_p = 2.44$. At this concentration, the system can no longer be approximated using the AOV model as it lies in the semi-dilute regime. In this situation, the range and behaviour of the depletion interaction is related to the polymer blob size and can no longer be approximated as the polymer's R_g. On an experimental time scale, without exposure to an applied magnetic field, particles would rarely separate due to the significant depth of the attractive potential energy well ($>> kT$) caused by the depletion interaction. Therefore, a high magnetic field strength was required in order to separate particles in contact. Regardless of these issues, Figure 4.11 shows the experimental (symbols) and theoretical (dashed lines) results using the AOV model with a $R_g = 225\ nm$. Although, as expected, the observed behaviour in experiments differs considerably from those of theory, agreement at a cut-off distance of $d = 3.1$ is still noted. Whilst no interaction potential could be evaluated, these results show promise if a better approximate model could be determined for high polymer concentrations and high field cases.

4.5 Conclusions

In conclusion, the pair potentials for a series of colloid-polymer mixtures have been measured by considering the separation probabilities of particle pairs. Both the attractive and repulsive contributions to the overall pair interaction have been studied and characterised. At low polymer concentrations, those within the dilute regime, good agreement between experiment and theory was found for experiments without an applied magnetic field. The AOV model, although simplistic, provided a good description of the experimental results. In the case of colloid-polymer systems with an applied magnetic field, discrepancies between experiment and theory were found, indicating the theory, as yet, does not accurately describe these situations. For the extreme instance, where the concentration of polymer was well above c^*, the AOV model broke down as expected. However, experiment and theory still showed qualitative correlation. This work should therefore provide a basis for further studies and will benefit from the inclusion of more appropriate and accurate theoretical depletion interaction models.

Acknowledgements

This work was performed in collaboration with Adam Edward Stones and Arran Curran.

Chapter 5

Cluster formation in quasi-2D colloid-polymer systems

ABSTRACT

In this chapter, the effects of polymer concentration on the formation and growth of clusters is investigated using a quasi-2D colloid-polymer mixture. Initially, the mechanisms by which clusters form and grow is assessed at each polymer concentration and subsequently characterised by measuring the weighted mean cluster size as a function of time. In conjunction with this, fractal growth theory of cluster formation in the dilute limit is used to asses whether a change in mechanism occurs as the polymer concentration is increased. The results from this analysis are compared to those of the weighted mean cluster size. Finally, a direct link between the mean cluster size and particle coordination number distributions is established. Experimental results are compared to a simple model developed using basic statistics and probability theory which shows good agreement when irreversible aggregation occurs.

5.1 Introduction

Aggregation is an important phenomenon ubiquitous in nature and common in many commercial manufacturing processes. Ice crystal aggregation is known to determine the reflective properties of clouds, important in countering the effects of global warming [111–113]. Protein aggregation can cause serious problems in biotechnology and pharmaceutical products if uncontrolled, as well as resulting in debilitating illnesses like Alzheimer's and Amyloidosis [114–116]. Flocculation is fundamental to the production of many dairy products including cheese [117, 118]. In agrochemical formulations, unwanted aggregation or flocculation can cause sedimentation of active ingredients which would otherwise remain dispersed. Together with their impact on technological applications, aggregation processes are also of fundamental interest in their own right. If such processes can be controlled and their kinetics understood, new materials and manufacturing processes may result. Many of the aggregation processes highlighted above arise with particles on the order of 10 nm to 10 μm and therefore fall into purview of the colloidal domain. Whilst these real world occurrences are often complex, model colloidal systems can be far simpler and provide an excellent avenue to understanding the underlying physics of their real world counterparts.

Aggregation in colloidal systems has been studied extensively [119–126]. Two distinct, limiting regimes, have been identified and are commonly referred to as diffusion limited cluster aggregation (DLCA) and reaction limited cluster aggregation (RLCA) [127,128]. In both DLCA and RLCA, particles undergo diffusive motion. Reaction limited cluster aggregation occurs when an energy barrier or mechanistic equivalent exists to the formation of permanent bonds between diffusive particles. This results in a probability of cluster formation, on contact, of significantly less than unity. In fact, particles or clusters may meet several times before a permanent bond is established between them. This type of behaviour can be attributed to the physical or chemical properties of a system. Hence, it is sometimes referred to as chemical limited cluster-cluster aggregation, but here we refer to it as reaction limited cluster aggregation.

In 1983, Meakin and Kolb independently developed theory for diffusion limited cluster aggregation and its relationship to concepts of fractal theory [129–131]. Individual particles and clusters of particles move though d-dimensional Euclidean space in a stochastic manner until collision with another particle or cluster occurs. These collisions are considered to be binary

and irreversible. Once a collision has occurred the resulting aggregate continues to explore d-dimensional space until a second collision occurs, upon which the process is repeated infinitely or until all particles have formed a single cluster.

Unlike the majority of aggregating colloidal systems reported in the literature, depletion systems are unique, due to the geometric considerations of the depletion interaction itself (see Chapter 2, Section 2.1.3). When two radially symmetric particles meet and stick, their geometry at the moment of contact is not fixed. This is where depletion systems differ from other aggregating colloidal systems. Indeed, once bound, there exists no significant energy barrier to stop particles orbiting around one another. For pairs of particles, this is inconsequential, as a single ground state configuration exists, but for clusters consisting of more than two particles, these effects start to become an important factor in overall cluster morphology [132]. For instance, in 2D, a cluster consisting of three particles effectively has a single close packed ground state and linear excited states. In the linear conformation, particles will freely orbit one another until the ground state configuration is reached. This is true whether the system is pairwise additive or not. However, for non-pairwise additive systems, an even deeper potential energy well exists for the ground state configuration due to the overlap of all the excluded polymer depletion zones [27].

In depletion systems, the cross over between pairwise and non-pairwise additivity is determined by the relative size of non-adsorbing polymer and colloid particle. Hence, $q = (R_g/a)$, where R_g is the polymer's radius of gyration and a the colloid particle radius. Depletion systems are only considered pairwise additive if $q < 0.15$. For the system presented here $q = 0.17$ and is therefore just over the boundary of the pairwise additive regime. Because of this and the aforementioned conformational considerations, it is not known whether the application of growth theory and fractal analysis to our system will result in the same agreements between experiments and theory previously reported in the literature [128]. It is also not known whether it will shed light on the specific aggregation processes which occur in our 2D depletion system.

In this chapter, we investigate whether the limiting cases of DLCA and RLCA theory can be applied to an experimental quasi-2D colloid-polymer system which differs from those 2D systems already reported in the literature. Three polymer concentrations were chosen to probe the effects of polymer concentration, and hence interparticle interaction strength, on cluster formation and growth. The weighted mean cluster size is used to determine the growth mechanism of each

system using established growth laws. These results are compared to those determined using fractal dimension analysis, which also utilises the mean cluster size. Finally, we draw a direct link between the mean cluster size and particle coordination number distributions using simple statistics and probability theory. Coordination number results are compared to a theoretical model based on hexagonal shell growth.

5.2 Theory

The time dependent evolution of aggregating clusters can be considered as a non-equilibrium process, starting with individual particles and ending with the formation of large clusters. Our understanding of the kinetics governing these processes originates from the work of Smoluchowski in the early 1900s [133]. Smoluchowski described the reaction kinetics in terms of reaction probabilities known as kernels, K. In a physical sense, each kernel accounts for the collision and sticking frequency between clusters of different sizes. The following expression models the process of irreversible aggregation in the dilute limit [133]

$$\frac{dn_k}{dt} = \frac{1}{2}\sum_{i=1}^{k-1} K_{(i,k-i)} n_i n_{k-i} - n_k \sum_{i=1}^{\infty} K_{(k,i)} n_i. \tag{5.1}$$

The two terms in Equation 5.1 correspond to the formation of clusters of size k by the association of smaller clusters (left) and the loss of clusters of size k due to continued aggregation (right) [134]. The reaction kernel, $K_{(i,k-i)}$, provides the mean rate of aggregation between clusters of size i (number of monomers) and clusters of size j to create clusters of size $k = i + j$. The kernel, $K_{(k,i)}$, accounts for the mean rate at which clusters of size n_k are lost due to subsequent aggregation. The number of clusters of each different size are denoted as n_i, n_{k-i} and n_k. The overall rate of change, dn_k/dt, in clusters of size k, is dependent on these kernels.

In physical situations, the reaction kernel K is written as a power of the average cluster size, N, $K \sim N^{\lambda}$. In the case of homogeneous kernels, where particles and clusters are considered to be distributed uniformly, λ is the degree of homogeneity. The Smoluchowski model makes several assumptions. Firstly, collisions are binary, only consisting of two clusters, therefore limiting the theory to dilute systems. Secondly, clusters are distributed homogeneously. At any point in time, local fluctuations in cluster and particle densities are not taken into account. And

finally, once a cluster of size k has formed, it is assumed it will never disassociate or break apart into smaller clusters.

5.2.1 Cluster growth

The kinetics of cluster growth is often studied by tracking the distribution of cluster sizes, $s(t)$, as a function of time. In particular, the weighted average cluster size

$$\langle s(t) \rangle \;=\; \frac{\sum s^2 n_s(t)}{\sum s n_s(t)}, \tag{5.2}$$

where s is the cluster size and n_s the number of clusters of size s, is characterised by a growth law [135] of the form

$$\langle s(t) \rangle \;\sim t^z. \tag{5.3}$$

Here, z is the growth exponent and depends on the aggregation regime and underlying growth mechanism. The growth exponent

$$z \;=\; (1-\lambda)^{-1}, \tag{5.4}$$

is related to the fractal dimension, D_f, via $\lambda \;=\; -1/D_f$. The generally accepted values for D_f in two dimensions are 1.45 and 1.55 for DLCA and RLCA, respectively [136]. This results in theoretical values of the growth exponent to be $z = 0.59$ and $z = 0.61$, respectively. However, a wide range of values has been reported in the literature for experimentally determined values [137].

5.2.2 Fractal dimension analysis

Cluster size distributions alone do not reveal the full details of an aggregation process. Cluster morphology and spatial densities are not directly accounted for. However, links between the two can still be drawn. The diffusive paths and subsequent collisions of net attractive particles lead to ramified structures, the local densities of which depend on the type of interparticle interaction present and mechanisms by which they are formed. By studying the fractal dimension of these

structures, information on their morphology and reaction mechanism leading to their formation can be found.

Although two dimensional systems are poorly understood and experimental evidence is limited [136], it is assumed that cluster diffusion is still inversely proportional to cluster size. Hence,

$$D_c \sim \frac{1}{R_g}, \tag{5.5}$$

where D_c is the diffusion coefficient for a cluster composed of i particles and R_g its radius of gyration. As previously establish in the literature [128, 129, 138], the irreversible aggregation of diffusive particles leads to the formation of fractal aggregates with a power law relationship

$$s_i = k_0 \left(\frac{R_g}{a}\right)^{D_f}, \tag{5.6}$$

between a cluster's R_g and size s_i, where k_0 is a proportionality constant usually on the order of unity.

5.2.3 Coordination number theory

Previous work reported in the literature [139] has found cluster growth can also be characterized by a discrete probability distribution $P(s)$ if the cluster size distribution is tracked as a function of time. From this, in conjunction with knowledge of the cluster structures, the distribution of particle coordination numbers (CN) as a function of time may be found.

A functional form of cluster size distribution, $P(s)$, is described by shifted geometric distribution [139] of the form

$$P(s) = \frac{1}{\mu}\left(1 - \frac{1}{\mu}\right)^{s-1}. \tag{5.7}$$

Here, s is the cluster size, specifically the number of particles in a cluster, and μ the mean of the distribution, $\mu = \Sigma_{s=1}^{\infty} sP(s)$. This provides the probability of selecting a cluster of size s when randomly sampling the system and $\Sigma_{s=1}^{\infty} P(s) = 1$. The probability that a selected particle, i, has a coordination number of c is related to the cluster's size. This probability is denoted as

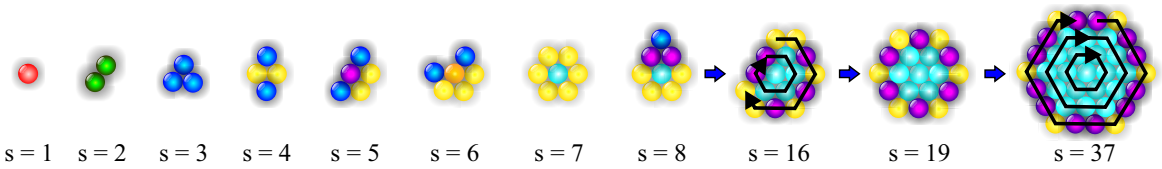


Figure 5.1: Geometric shell growth for clusters of size 1 - 37 with colours representing individual particle coordination numbers, CN. Individual particle coordination numbers are coloured according to the following, CN = 0 = Red, CN = 1 = Green, CN = 2 = Blue, CN = 3 = Yellow, CN = 4 = Purple, CN = 5 = Orange and CN = 6 = Cyan.

$P(c \mid i;s)$ and the probability of a particle i being a member of a cluster of size s as $P(i;s)$. The probability of randomly selecting a particle with a coordination number c belonging to a cluster size s is equal to the product of $P(i;s)P(c \mid i;s)$= $P(c \cap i;s)$ where $\cap$ is the union of two events. Thus, the probability that a particle, selected at random, has a coordination number c is given by

$$Pc = \sum_{s=1}^{\infty} P\left(c \cap i;s\right) = \sum_{s=1}^{\infty} P(c \mid i;s)P(i;s). \tag{5.8}$$

It has been shown [139] that the probability of selecting a particle i belonging to a cluster of size s, $P(i;s)$, may be evolved from the probability distribution, $P(s)$, by the normalized probability distribution

$$P(i;s) = \frac{sP(s)}{\sum_{s=1}^{\infty} sP(s)} = \frac{s}{\mu^2}\left(1 - \frac{1}{\mu}\right)^{s-1}. \tag{5.9}$$

Here, $P(i;s)$ is related to the weighed mean cluster size by $\Sigma_{s=1}^{\infty} sP(i;s) = \langle s \rangle$. Although initially developed for the analysis of the linear cluster chains, this theory may be extended to the evolution of compact radial clusters.

For compact clusters like those observed in the experiments described here, a hexagonal shell growth model can be applied. Starting with a single particle, clusters are grown as illustrated in Figure 5.1. For each increment in cluster size, an additional particle is added which alters the coordination number distribution for that cluster. Via this process of successive shell growth, clusters are generated algorithmically using specifically developed Mathematica code. Subsequently, the data is evaluated numerically using Equation 5.8 from cluster sizes of $s = 1 - 500$. Generating all possible cluster sizes from $s = 1$ to ∞ is not feasible, but cluster

sizes of $s = 500$ are far larger than those likely to form in the systems presented here within the field of view (FOV). The values of $P(c \mid i; s)$ are determined from these clusters.

5.3 Experimental method

5.3.1 Sample preparation

Three different polymer concentrations of quasi-2D colloid-polymer system were investigated. Superparamagnetic particles with a diameter of $\sigma = 3.0\ \mu m$ were mixed with appropriate xanthan dilutions as described in Section 3.3 and imaged using a UCPlanFLN 40× magnification 0.70 infinity/0-1.6/FN22 Olympus objective mounted on an Olympus CKX41 inverted microscope. Between experiments, samples were re-dispersed using an electric coil and applied magnetic field independent from the imaging setup. Images were captured at intervals of 1 s and particle coordinates of each frame identified using the techniques described in Section 2.2.3. The imaging setup was characterised before experiments using a gaussmeter, to ensure no residual magnetic field was present. The details of all systems investigated are summarised in Table 5.1, including the polymer concentration, diffusion coefficient and Brownian time of each system. The diffusion coefficient of each system was determined using the techniques described in Chapter 3. The experimental time for each polymer concentration is subsequently expressed in units of Brownian time, τ_B. Due to the particle area fractions needed to form clusters, only limited data could be gathered on individual particles before clustering occurred, therefore Brownian times are approximate.

5.3.2 Cluster identification and coordination number tracking

Individual particle coordinates for each frame of microscopy data were determined using the methods described in Section 2.2.3. Custom Mathematica code was developed to classify the number and size of clusters present in each frame. Each particle's CN was also assigned using the same program. Both were established by utilising an inbuilt nearest function available within the Mathematica software. A cut off parameter of $1.1(\sigma)$ was used to determine the limit of nearest neighbour distance.

Sample name	concentration ($g\ dm^{-3}$)	ϕ_p	ϕ_a	D (10^{-2})($\mu m^2 s^{-1}$)	$\tau_B(s)$
$P1$	0.028	0.003	0.11	3.08	73.01
$P2$	0.054	0.006	0.14	2.35	95.75
$P3$	0.099	0.010	0.12	1.84	122.34

Table 5.1: A summary of each system's properties including its reference label, polymer concentration, particle area fraction and Brownian time.

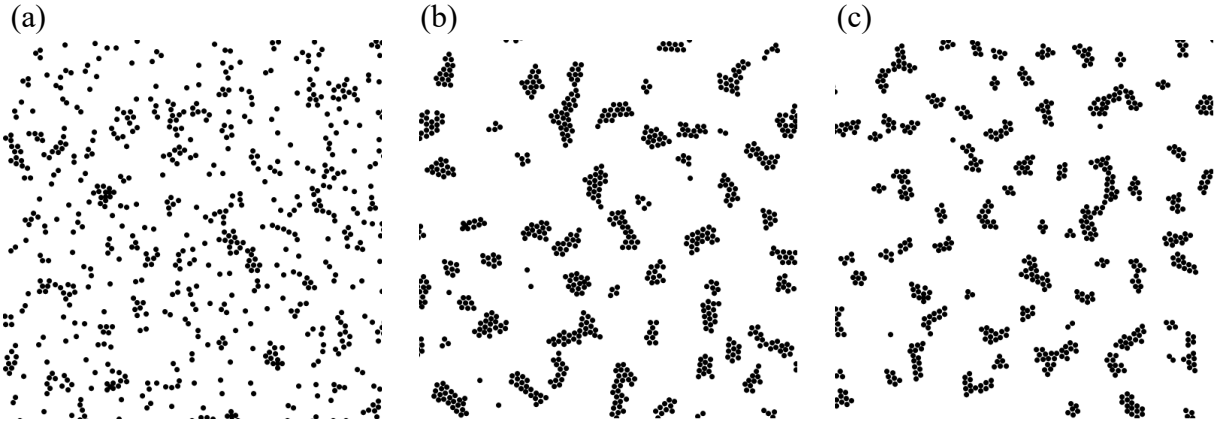


Figure 5.2: Experimental snapshots showing the cluster size distribution and cluster morphology of (a) P1, (b) P2 and (c) P3 at a scaled time of $49\tau_B$.

5.4 Results and discussion

This section is split up into three parts. First, we considered the cluster growth in all three systems as a function of time. Next, fractal growth analysis was applied to each system and compared to results from the cluster growth analysis. Finally, the coordination number distributions as a function of weighted mean cluster size was studied and compared to the results from Section 5.4.1 and 5.4.2. The details of each system are summarised in Table 5.1. The area fractions of all three systems were in the dilute regime and closely matched one another. Therefore, direct comparisons between all three systems could be made as the growth kinetics was considered to be decoupled from the particle density and solely related to the polymer concentration.

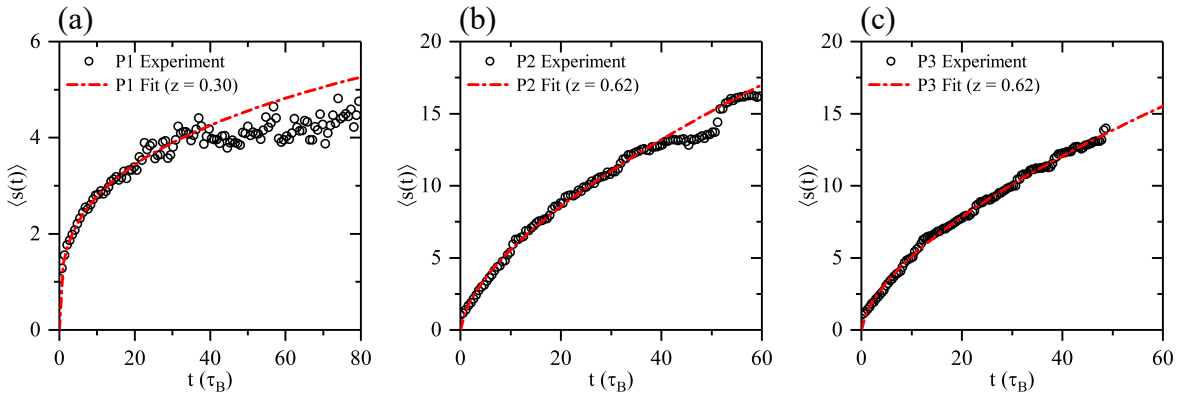


Figure 5.3: The weighted mean cluster growth as a function of scaled time for P1(a), P2(b) and P3(c). Symbols represent experimental results and dashed lines are fits to the data using Equation 5.3.

5.4.1 Cluster growth analysis

First, the cluster growth for each polymer concentration was considered. Figure 5.2 shows a snapshot of each system, P1, P2 and P3, at the scaled time of $49\tau_B$. Initially all three systems consisted of homogeneously dispersed, discrete particles. This starting configuration was achieved by exposing each sample to an applied magnetic field before experiments were performed. Figure 5.2 (a) shows the formation of transient clusters in P1, at a polymer concentration of 0.028 $g\ dm^{-3}$, after the system had reached equilibrium. As the concentration of polymer was increased, the formation of permanent, close packed clusters was observed in P2 and P3 as shown in Figure 5.2 (a) and (b). No discernable differences in cluster morphologies were apparent, apart from a slight variation in the mean cluster size, with the clusters of P2 appearing slightly larger than those of P3. This was probably due to the initial area fraction, ϕ_a (see Table 5.1), of P2 which was slightly higher than that of P3.

Figure 5.3 shows the change in weighted mean cluster size as a function of the scaled time for samples P1, P2 and P3. Figure 5.3 (a) shows cluster growth occurring in P1 between times of $0\tau_B$ and $30\tau_B$. From $30\tau_B$ onwards, the system came to equilibrium and fluctuated about a mean cluster size of 4 particles. Although this system lies outside the bounds of growth and fractal theory discussed in Section 5.2, a fit (dashed line) to the data (symbols) was performed between $0\tau_B$ and $30\tau_B$ where cluster growth was observed (Figure 5.3 (a)) using Equation 5.3. A growth exponent of $z = 0.30$ was found.

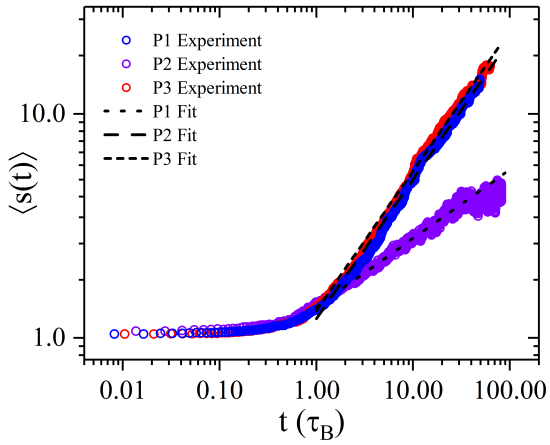


Figure 5.4: The growth behaviour of all three colloid-polymer systems using a log log scale. The long time power law growth regime is apparent. Symbols are experimental results and dashed lines are fits.

At polymer concentrations of 0.054 $g\ dm^{-3}$ and 0.099 $g\ dm^{-3}$, irreversible cluster formation occurred in P2 and P3, respectively. In both cases, a power law growth behaviour was observed. By fitting Equation 5.3 to the data for the entire experimental time domain, a growth exponent of $z = 0.62$ was found for each polymer concentration. This is close to the theoretical value for a RLCA mechanism of $z = 0.61$ as opposed to a DLCA mechanism which should have a growth exponent of $z = 0.59$.

Using Equation 5.4 and $\lambda = -D_f^{-1}$, the fractal dimension of both P2 and P3 was found to be $D_f = 1.63$. This is noticeably higher than the theoretically determined values of 1.55 and 1.45 for RLCA and DLCA mechanisms respectively. It is noted that the cluster morphologies of P1 and P2 are hexagonal close packed. Therefore, one would expect to find a fractal dimension greater than those associated with either RLCA or DLCA mechanisms. Both DLCA and RLCA are known to result in cluster morphologies less densely packed than those observed in our experiments. It can also be argued that the difference between growth exponents and thus the fractal dimensions associated with DLCA and RLCA mechanisms is inherently hard to measure experimentally. The difference between the two, $\Delta z = 0.04$, is small when compared to the possible range, $1.0 - 2.0$, of theoretical fractal dimension values when considering structures in 2D. Therefore, we contend that it is difficult to determine the growth mechanism of an aggregating system with an experimentally determined growth exponent alone, especially when considering the depletion systems presented here.

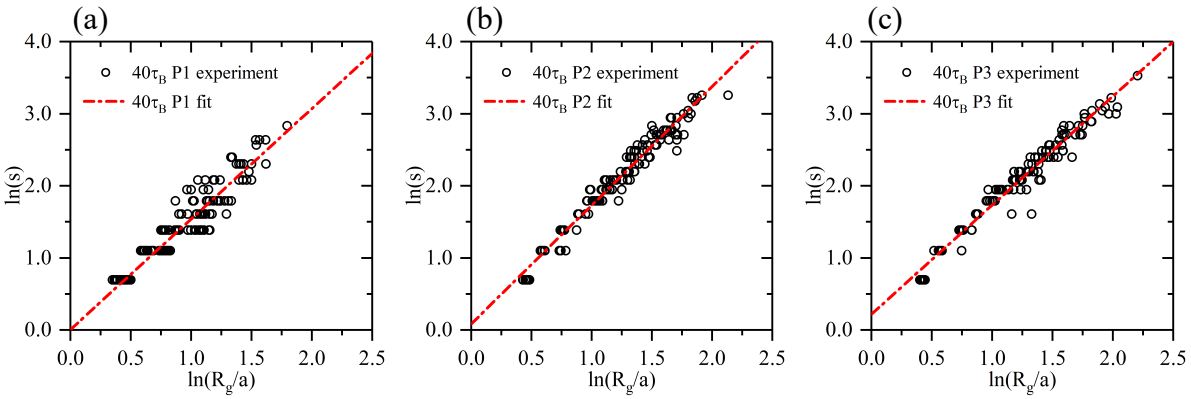


Figure 5.5: Plots (a), (b) and (c) show the relationship between cluster size and radius of gyration. Each plot represents a single equivalent instance in time for all three systems. A long time of $40\tau_B$ is compared. The slope of the fit (dashed lines) to experimental data (symbols) provides each system's fractal dimension.

Figure 5.4 compares and contrasts the experimental results (symbols) and power law fits (dashed lines) of all three systems in log-log form. The expected long time power law growth regimes are apparent from the data with P2 and P3 collapsing onto one another. A power law growth regime is also seen for P1, but with a slower rate of cluster formation. The plateau caused by the system reaching an equilibrium state is also apparent at later times.

5.4.2 Fractal dimension analysis

Next, fractal dimension analysis (Section 5.2.2) was applied to the experimental results and compared to the findings of Section 5.4.1. First, the log of Equation 5.6 was taken and subsequently rearranged to the form

$$\ln(s) \;=\; D_f \ln(R_g/a) + \ln(k_0). \tag{5.10}$$

Figure 5.5 shows the experimental results (symbols) and least square fits (dashed lines) for each system (P1, P2 and P3) at a equivalent late time of $40\tau_B$. The slope of each fit is equal to the fractal dimension at this instant in time. The same analysis was applied to all frames of data for each system. Figure 5.6 shows the results of this analysis, for the fractal dimension as a function of the scaled time. At early times, the fractal dimension rapidly increases for all systems until a plateau is reached at approximately $15\tau_B$. At this point, the fractal dimension remains constant for all systems. The average D_f for each system is calculated by excluding

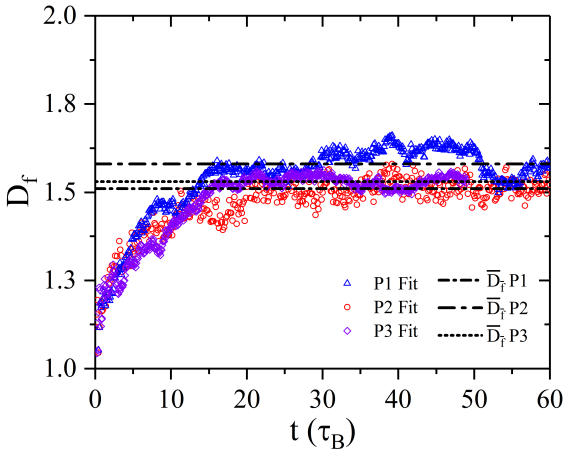


Figure 5.6: Results of the analysis method shown in Figure 5.5 for all frames, of each system, in scaled time. Symbols represent the fractal dimension measured for each frame and lines represent the mean fractal dimension using results from the plateau region.

early time data $< 15\tau_B$. The fractal dimension for P1, P2 and P3 were found to be $P1 = 1.51$ $P2 = 1.58$ and $P3 = 1.53$ and corresponding growth exponents were calculated as $P1 = 0.60$ $P2 = 0.61$ and $P3 = 0.60$, respectively. The lowest polymer concentration, P1, showed a fractal dimension similar to that of a reaction limited system and subsequently a corresponding calculated growth exponent, however, the calculated growth exponent from fractal analysis, $z = 0.60$, and the measured growth exponent of $z = 0.30$ show little correlation. These disagreements were expected as equilibrium systems are not encompassed in the aggregation theory applied here. From these results, excellent agreement between the calculated growth exponents of P2 and P3 from fractal analysis and those of Section 5.4.1 is found. All fractal dimensions are approximately 1.55, typical of a RLCA mechanism.

The initial temporal dependency of the D_f has been reported by others in the literature [140] studying the aggregation of colloidal systems, but the origin remains unclear. In our work, the initial rise in the D_f at early times can be attributed to the morphology of clusters which initially adopt linear conformations, only to collapse into denser close packed structures as the systems evolve. The overall higher fractal dimension measured here and in Section 5.4.1 is attributed to the compact nature of the cluster morphology observed in our system and is shown in Figure 5.2 (b) and (c).

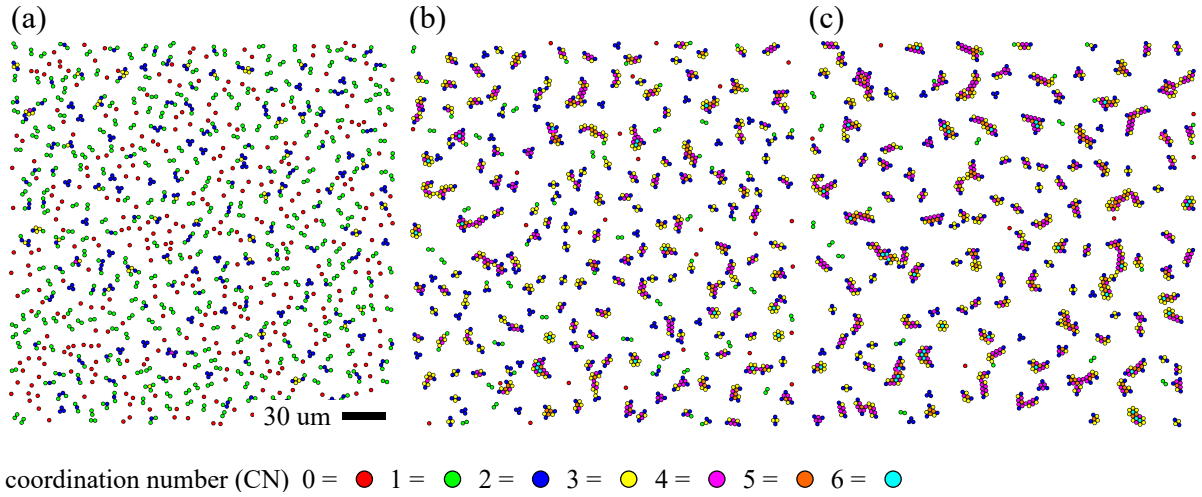


Figure 5.7: Example of cluster tracking and coordination number identification for P3 at t = 4.1, 24.5 and 49.0 τ_B. Individual particle coordination numbers are coloured according to the following, CN = 0 = Red, CN = 1 = Green, CN = 2 = Blue, CN = 3 = Yellow, CN = 4 = Purple, CN = 5 = Orange and CN = 6 = Cyan.

5.4.3 Coordination number analysis

Finally, we tracked the coordination number, CN, and clusters size distributions as a function of time for all three systems, P1, P2 and P3. As we were primarily interested in analysing the formation and morphology of clusters in the non-equilibrium systems of P2 and P3, an example of the coordination number identification and cluster tracking analysis results are shown in Figure 5.7 for P3, using the image processing algorithm described in Section 5.3.2. The results of image analysis are shown for three different times. These were 4.1, 24.5 and 49.0 τ_B, corresponding to the images (a), (b) and (c). As expected, due to the formation of clusters through irreversible aggregation, the coordination number distribution evolved as a function of time, with lower coordination numbers diminishing and higher coordination numbers becoming more common. From the results, it is clear clusters adopt a close packed structural conformation, as opposed to open chain or branch like structures. This accounts for the high occurrence of CN = 6 at late times. The image analysis results for P2 showed similar change in CN and cluster size distributions as P3.

All results from coordination number tracking and cluster size distributions were scaled by the mean cluster size to create coordination number probability distributions as a function of the mean cluster size. This decoupled the time dependence of the coordination number distributions from the temporal domain. Figure 5.8 (a) and (b) shows the probability distributions for P2 and

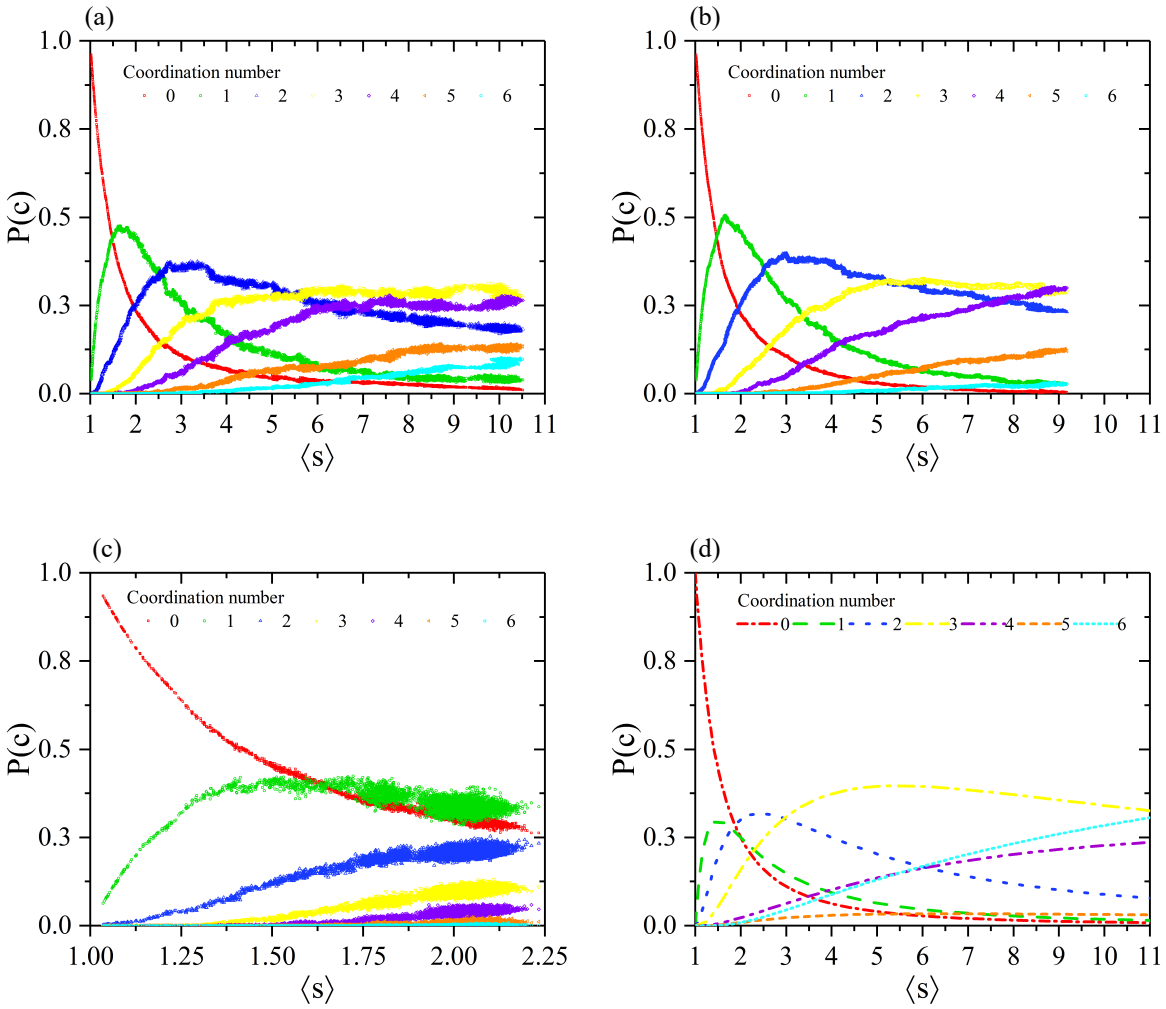


Figure 5.8: Experimental coordination number probability distributions for P2 (a), P3 (b) and P1 (c) are plotted as a function of mean cluster size. Results from theoretical calculations using a shell growth model are shown in plot (d).

P3 respectively. Both show a rapid decay in particles with CN of 0 followed by a rapid increase in CN of 1 as the mean cluster size increases. When overlaid (not shown for clarity), coordination number distributions for CN of $0, 1, 2$ and 3 were indistinguishable. However, differences were found between particles with CN of 4 and 5 when considering both systems. A notable increase in the number of particles with a CN of 6 in P2 can be attributed to the disk-like morphology of larger cluster sizes. The equilibrium system of P1 shows a distinct CN distribution. Unlike P2 and P3, the dominant CNs are $0, 1$ and 2. This indicates that independent particles and clusters consisting of pairs and triplets are the dominating clusters and also that these clusters are transient in nature. A maximum coordination number of 5 was found, but with a low probability of occurring. Particles with a CN of 4 are also noted. Figure 5.8 (d) shows the

theoretical results calculated using the shell growth model described in Section 5.2.3. Overall, qualitative agreement is found when comparing these results to the experimental results of P2 and P3. Excellent agreement is found for CN = 0, and close agreement is identified for CN of $2, 3$ and 4. Noticeable deviations are apparent for CN of $1, 5$ and 6 with CN of 1 and 5 being underestimated and 6 being vastly overestimated at large cluster sizes. This simply reflects the asymmetric nature of the larger clusters observed at late times. This is in contrast to the radially symmetric clusters evolved using the shell growth model.

Although both growth and fractal analysis require individual particle coordinates, their insensitivities to cluster geometries is apparent. However, the coordination number analysis reveals small variations between each system and appears to be sensitive to the change in polymer concentration. Therefore, we suggest this method provides greater insight into cluster morphologies and could be used as a fingerprint to distinguish between different growth mechanisms with further development of the accompanying theoretical model.

5.5 Conclusions

In conclusion, the aggregation behaviour for three different polymer concentrations of quasi-2D colloid-polymer systems has been studied. Growth theory and fractal dimensional analysis was applied to study the effects of polymer concentration on cluster growth. As the polymer concentration was increased, a transition from equilibrium to irreversible cluster aggregation was observed. For the two highest polymer concentrations, we found the mean cluster size grew as a power law in time. The experimental growth exponents for these systems were identical and suggestive of an RLCA mechanism, however, for the higher polymer concentration this is clearly not the case and DLCA is the more likely mechanism by which clusters form. A larger fractal dimension was found than either DLCA or RLCA growth theory predicts. We attribute this to the compact nature of clusters formed by the depletion interaction. The experimental growth exponents showed excellent agreement with results from fractal dimensional analysis. Coordination number analysis provided further quantitative evidence for compact cluster morphologies. These same data were compared to a simple theoretical model which showed qualitative agreement with experiments.

Acknowledgements

This work was carried out in collaboration with Colin Reynolds and William Sampson.

Chapter 6

Formation and evolution of networks in quasi-2D colloid-polymer mixtures

ABSTRACT

In this chapter, the formation of networks in quasi-two-dimensional colloid-polymer mixtures is studied using cluster growth theory and fractal dimension analysis. In conjunction with this, a novel application of bond-order orientational and coordination number analysis is applied to investigate the evolution of colloidal networks during and after their formation. In particular, the effects of varying polymer concentration and thus interparticle interaction strength are tested using these analysis techniques. It is found that networks form for both concentrations of polymer, but with different morphologies and evolution behaviours pre- and post-network formation. Rearrangements of clusters and network strands readily occur at the lower polymer concentration, resulting in thicker more crystalline structures. However, at a higher polymer concentration, the same phenomenon is not observed and the individual clusters and overall network morphology differs as a consequence.

6.1 Introduction

The topic of gel formation, ageing and collapse has received much interest and debate over recent decades [48, 49, 141–144]. Gels are defined by their unique properties in comparison to other materials. Their bulk is composed predominately of a fluid, yet they behave much like a solid in the absence of an applied force. However, when stress is applied, they deform and flow much like a liquid. Gels are prolific in biological systems [145, 146] and often found in commercial products too [23, 147]. Particle gels are of particular importance in agrochemical products, as active ingredients are frequently on the order of the colloidal length scale and mixed with gel inducing non-adsorbing polymers to aid in product stabilisation and performance. If gelation can be controlled, new materials could be formed [148, 149].

A hunt for an underlying and unifying theory for the formation and evolution of arrested states continues [150], but coarsening and kinetic arrest of systems is thought to be driven by the process of spinodal decomposition, which to date has been suggested as the most likely universal mechanism [151]. Whilst much progress has been made in understanding the structural [152,153] and mechanical properties of network and gel forming systems, including the nuances which govern their formation, the microstructural processes responsible for coarsening dynamics during and after arrest are still poorly understood [154–159].

Although the formation of three-dimensional (3D) gels has been widely studied [151, 160–163], surprisingly little work has been conducted on their two-dimensional (2D) analogous. The little work that does exists has focused on the formation, evolution and structural properties of 2D clusters and networks at either air - water or oil - water interfaces [52,164–169]. Whilst valuable and interesting model systems in their own right, they are thought to exhibit unusual and system specific behaviours due to a combination of electrostatic, hydrodynamic and capillary effects [170]. It has been suggested that these particularities contribute to differences between cluster and network properties determined through experimental observations and the predictions made from theory and simulations. The combination of interparticle effects observed in these systems means only part of a larger picture can be formed.

Here, we present a promising alternative quasi-two-dimensional model system to the complex and dynamic interfacial systems already reported. Our system provides the ability to fine

tune both the long range repulsive and short range attractive interparticle interactions, but does not suffer from the aforementioned capillary effects. By using a combination of superparamagnetic particles and xanthan gum, we are able to study the formation of particle networks caused by depletion on a substrate rather than at an interface. The incorporation of superparamagnetic particles into the system design allows networks to be formed and then redispersed at will. It also raises the possibility of controlling the rate and structural bias of cluster and network formation through the application of a constant magnetic field during the aggregation process. The colloidal system can be directly manipulated using optical tweezers, the surface chemistry of particles used can be easily altered and finally the strength of interparticle interactions can be quantified using the techniques described in Chapter 4. However, in this chapter, we focus on the changes which arise due to altering the strength of the short range, depletion induced, interparticle interactions and study the effect this has on 2D network formation and evolution. This model system is an extension of the cluster systems already discussed in Chapter 5, Section 5.3.

In this chapter, the growth, formation and evolution of quasi-two-dimensional networks in colloid-polymer mixtures is investigated at two different polymer concentrations. Firstly, the cluster growth behaviour at both polymer concentrations is characterised using growth theory and fractal dimension analysis. Analysis is applied both pre- and post-percolation. The results of each system are then compared and discussed. Secondly, bond-order-orientational and coordination number analysis is used to further understand the unique characteristics and traits of this colloid-polymer system as it evolves with time. The local orientation of each particle with respect to its nearest neighbours is calculated using the hexagonal local bond-orientational order parameter. This is then used to determine structural rearrangements at the global and local levels. Finally, this information is used to characterise the cluster and network morphologies as each system evolves and, in the case of a high polymer concentration, completely arrests.

6.2 Experimental method

6.2.1 Sample preparation

Two samples with polymer concentrations of 0.067 $g\ dm^{-3}$ and 0.239 $g\ dm^{-3}$ were prepared using the methods described in Section 2.2.1 and Section 5.3 using superparamagnetic particles (Dynabeads®) of diameter $\sigma = 3.0\ \mu m$. These systems are referred to as P1 and P2 respectively. To form a 2D particle gel, an appropriate increase in particle area fraction was achieved by increasing the proportion of particle dispersion added to the colloid-polymer mixture before injection into the sample cell (Hellma Cell©). The area fractions for P1 and P2 were 0.38 and 0.36 respectively. Imaging of each sample was performed according to the methods described in Section 2.2.2. Images were captured using a UCPlanFLN 40× magnification 0.70 infinity/0-1.6/FN22 Olympus objective mounted on an Olympus CKX41 inverted microscope at intervals of 1 frame per second. Particle coordinates were extracted using the method described in Section 2.2.2. To check for pinned particles, all early time frames were superimposed on top of one another. Using this method, pinned particles could be identified as bright spots. Particles undergoing Brownian motion were not shown due to the time averaging of their intensity profiles over Euclidean space, bound by the field of view. Prior to each run, samples were placed in an applied magnetic field to disperse any cluster that had formed, once sedimentation onto the glass surface of the cell had occurred. Each sample was then removed from the field and imaged immediately. Due to the experimental limitations caused by drift at long times, the results of P1 covered a shorter time span than those of P2.

6.2.2 Cluster growth and network formation analysis

First, we define the point at which percolation first occurs by identifying the first frame where a single cluster spans the entire field of view (FOV). This point in time is defined as t_p and is a significant stage in the systems evolution. It defines the time at which arrest first occurs and the system's dynamics alter dramatically. Next, the moment at which the first cluster is detected with a radius of gyration equal to half the length of the FOV is determined. We denote this as t_{Rg}. This is the first point in time where cluster analysis can no longer be considered a reliable quantification of the growth dynamics, due to the similarities in length scale between the cluster

sizes and imaging FOV. Following this, we analyse the preceding frames of each stage, t_{Rg} and t_p, using the techniques described in Section 5.2 in order to measure the growth exponent and characterise the fractal properties of each system. As several large clusters which do not fill the FOV persist and continue to grow post-percolation, the same analysis is also applied to the entire data set from the experiment start time, t_0, until the last recoded frame, t_f. Finally, coordination number (Section 5.3.2) and bond-orientational order analysis is performed on all frames of data to investigate and characterise the dynamics at each polymer concentration, before and after percolation.

6.2.3 Bond-orientational order analysis

In order to investigate the formation and evolution of each system pre- and post-percolation, we use cluster based bond-orientational order analysis to quantify particle rearrangements once clusters and subsequent networks have formed. The local crystallinity of compact clusters can be quantified using the local bond-orientational order parameter [171]

$$\psi_6\left(\vec{r}_j, t\right) = \frac{1}{N_j(t)} \sum_{k=1}^{N_j(t)} e^{i6\Delta\theta_{jk}(t)}. \tag{6.1}$$

Here, particle j is located at position r_j and $\Delta\theta_{jk}$ is the angle between the reference vector x and bond vector connecting particle j to one of its N_j nearest neighbours, k. Local orientation of particle j is given by the argument of $\psi_6\left(\vec{r}_j, t\right)$ such that

$$\theta_6\left(\vec{r}_j, t\right) = \frac{1}{6}\arg(\psi_6(\vec{r}_j, t)). \tag{6.2}$$

Due to the inherent symmetry of a 2D-hexagonal lattice, the $\theta_6\left(\vec{r}_j, t\right)$ varies from 0 to 60°. An example of this analysis applied to a small cluster is provided in Figure 6.1. A custom algorithm was produced by further developing the cluster code described in Section 5.3.2, to enable each particle's $\theta_6\left(\vec{r}_j, t\right)$ to be determined and the cluster to which each particle belonged.

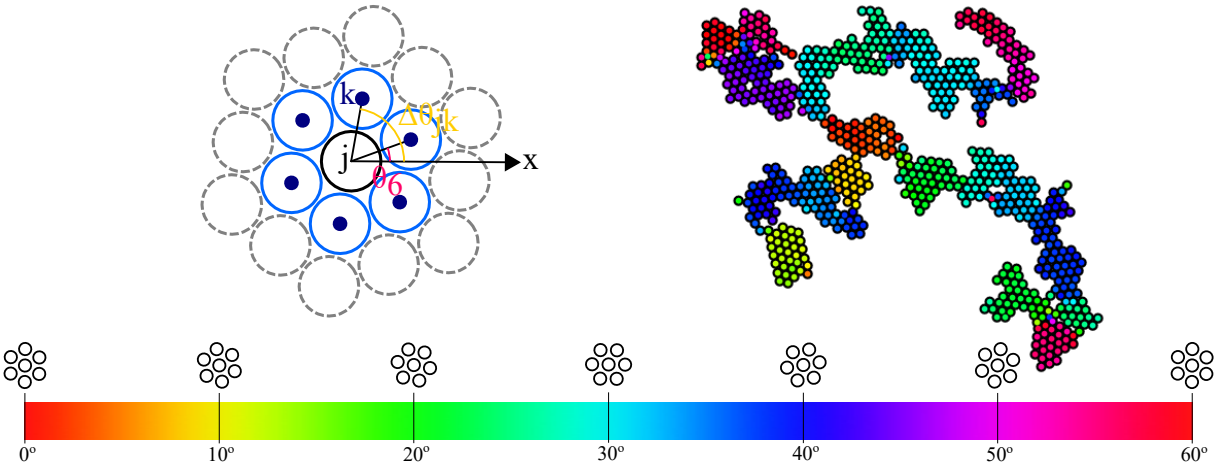


Figure 6.1: An example of bond-orientational order analysis applied to a single cluster (right). The schematic (left) shows the angle, $\Delta\theta_{jk}$, between the reference orientation, x, and particles of interest, j and k. This is subsequently used to determine the local bond orientation, θ_6, for each particle. Each particle in the cluster is assigned a colour using this value, in accordance with the colour bar shown.

6.3 Results and discussion

This section is split into two parts. In part one, the cluster growth and network formation is characterised by tracking the number and weighted mean cluster size as a function of time. The same fractal dimension analysis as described in Section 5.2.2 is applied to measure the fractal dimensions of both systems as a function time. The time averaged fractal dimension is also considered. Using these data and the post image analysis microscopy data from which they are derived (see Figure 6.2), two key stages in network growth are identified (see Section 6.2.2). The first is the point at which a single cluster is detected with a $R_g = l/2$, where l is the width of the microscopy field of view (FOV). The second is the point at which percolation is first observed. Here, we define percolation as the point at which a single network strand is found to span the entire FOV. Part two focuses on the bond-orientational-order, θ_6, within the clusters and networks as a function of time. The coordination number distributions are also considered and compared to these results. Here, the change in the standard deviation, $\sigma_{\theta 6}$, of $\theta_6\left(\vec{r}_j, t\right)$ is studied as a function of time at both the global, the entire system within the FOV, and at the single cluster level.

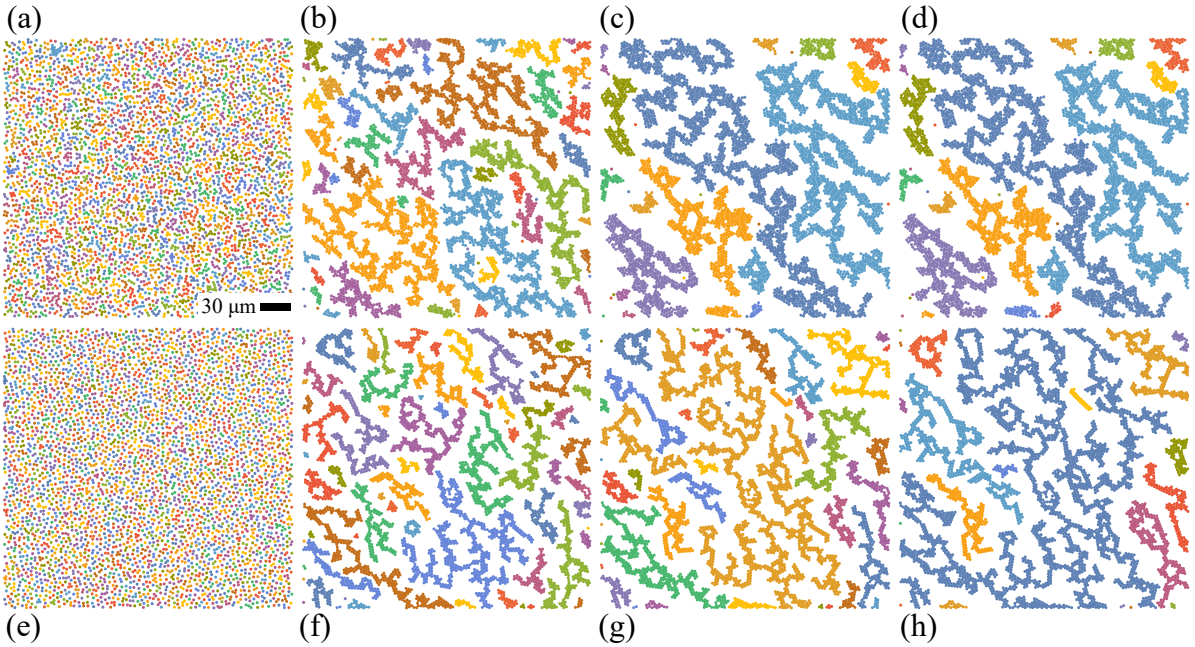


Figure 6.2: Snapshots of the image processing results used to determine the cluster size distributions for P1 (top row) and P2 (bottom row). Colours are randomly assigned to differentiate between clusters. Images illustrate 4 key steps in each system's evolution. These correspond to; initial configuration (a)(e), point at which $R_g = l/2$, denoted t_{Rg} (b)(f), percolation time, t_p, (c)(d) and the final configuration, t_f, (d)(h).

6.3.1 Cluster growth and network formation analysis

Cluster and network growth

First, the evolution of P1 and P2, with xanthan concentrations of 0.067 $g\ dm^{-3}$ and 0.239 $g\ dm^{-3}$ respectively, are summarised in Figure 6.2. The corresponding particle area fractions are 0.38 for P1 and 0.36 for P2. The top and bottom row show four key steps in the evolution of P1 and P2, respectively. These are the initial configuration, t_0, (a)(e), the point at which the first cluster reaches a $R_g = l/2$ denoted t_{Rg} (b)(f), the first time at which percolation is observed, t_p, (c)(d), and the final configuration, t_f, (d)(h) for both systems. Even at early stages, differences between each system are apparent and become more pronounced with time. For instance, the average strand thickness at t_f (Figure 6.2 (d)(h)) was found to be 4 particles for P1 and 2 particles for P2. By inspection, a difference in strand thickness was noted at early times, at approximately t_{Rg}.

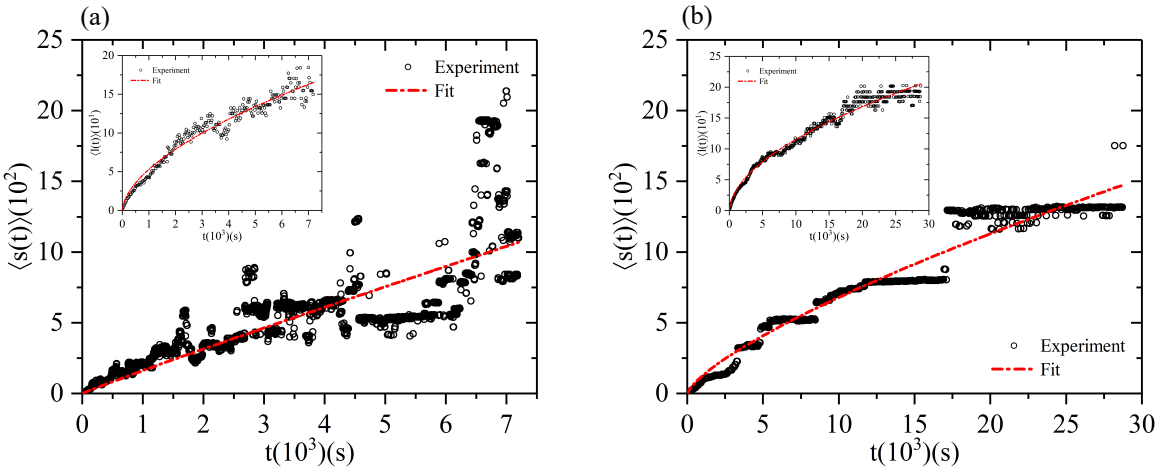


Figure 6.3: (a) and (b) show the weighted average cluster size (open circles) and number average cluster size (open circles inset plots) as a function of time for P1 and P2, respectively. The fits shown (red dashed lines) to the weighted and number average cluster size using Equation 5.2 are for all times.

Figure 6.3 shows the change in weighted mean cluster size

$$\langle s(t)\rangle \;=\; \frac{\sum s^2 n_s(t)}{\sum s n_s(t)}, \tag{6.3}$$

where s is the cluster size and n_s the number of clusters of size s, and the number mean cluster size (insets)

$$\langle s_n(t)\rangle \;=\; \frac{\sum s n_s(t)}{\sum n_s(t)}, \tag{6.4}$$

as a function of time. Plots (a) and (b) show the evolution of P1 and P2 respectively. Open symbols are results from experiment and dashed red lines are fits to both $\langle s(t)\rangle$ and $\langle s_n(t)\rangle$ using Equation 5.3. The experimental results from t_0 to t_f are shown in each plot as are the corresponding fits. However, subsequent fits were performed from t_0 to t_{Rg} and from t_0 to t_p. These results are summarised in Table 6.1.

Table 6.1 shows the growth exponents for both systems over all three time domains. The overall trend is one of a larger growth exponent, z, than for those found in the cluster forming systems discussed in Chapter 5. This is consistent with the comparatively higher particle area fractions necessitated in P1 and P2 in order to achieve network formation and percolation. There are also clear differences between the exponents determined using the weighted mean

	$P1$			$P2$		
	$t(\tau_B)$	$z_{\langle s(t)\rangle}$	$z_{\langle s_n(t)\rangle}$	$t(\tau_B)$	$z_{\langle s(t)\rangle}$	$z_{\langle s_n(t)\rangle}$
t_{Rg}	20.40	0.78	0.69	19.67	0.66	0.65
t_p	92.95	0.82	0.72	55.14	0.89	0.57
t_f	92.98	0.82	0.72	185.74	0.73	0.54

Table 6.1: Summary of the growth exponents found using fits to the number mean cluster size ($z_{\langle s_n(t)\rangle}$) and weighted mean cluster size ($z_{\langle s(t)\rangle}$) as a function of time over the domains t_{Rg}, t_p and t_f and the point at which they occurred in scaled time.

cluster size in comparison to the number mean cluster size. The latter method resulted in consistently smaller values. This is also not surprising due the reduction in weighting from larger cluster sizes at later times. However, at earlier times the growth exponents converge, as to be expected, again due to the influence of weighing the mean cluster size. Other than this, no apparent patten is clear when comparing z of P1 and P2. Therefore, the physical significance of these results remains elusive and further investigation is required. However, clear differences between each system's percolation time, t_p, was found.

Due to the area fractions of both P1 and P2, it was not possible to directly measure a Brownian time for either system as clusters formed too quickly and inhibited the amount of time single particles were free to diffuse. Therefore, the temporal scaling has been kept in units of seconds. However, in order to try and compare the temporal evolution of P1 and P2, we estimate the Brownian time by using the results from Chapter 3. By using the result of the fit to these data, we calculate a Brownian time of 77.44 s for P1 and 155.06 s for P2. In order to compare the most significant point in each systems evolution, the point at which they percolate and a network is formed, we scale t_p and t_{rg} by the estimated Brownian time. Subsequently, the two systems appear to initially evolve at the same rate, with respects to cluster size, up until t_{rg}. Indeed, one could reason they would continue to evolve past this point at equivalent rates. However, we find a difference in the percolation time when comparing the two systems (see Table 6.1). Percolation occurs earlier for P2 than for P1. This suggests the greater interaction strength, caused by the higher polymer concentration, resulted in an earlier t_p time due to thinner network strands and more ramified structures.

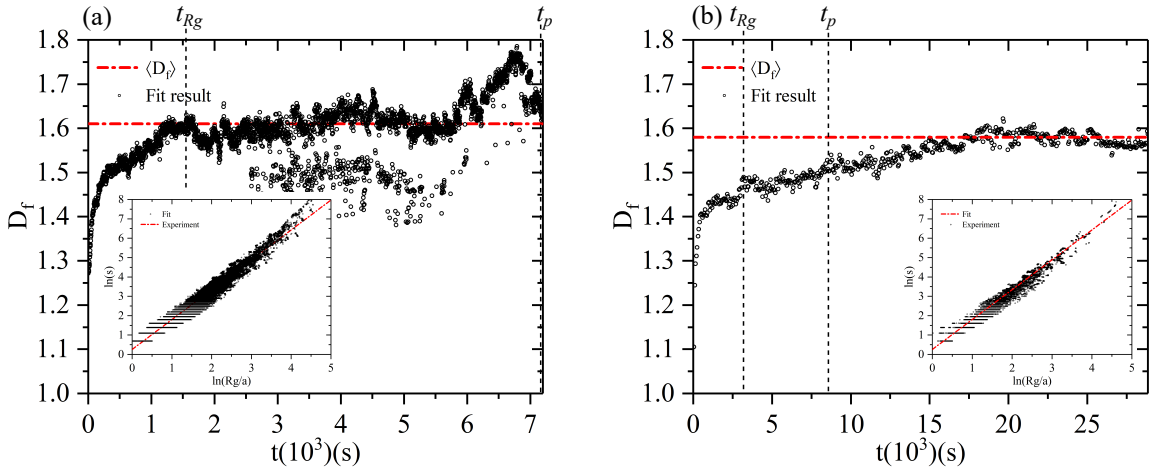


Figure 6.4: (a) and (b) show the fractal dimension, determined using the method described in Section 5.2.2, for P1 and P2 respectively, as a function of time. Symbols are experimental results and lines are represent the mean D_f using data from each plateau region. Insets show the experimentally (symbols) determined relationship between cluster size and radius of gyration for all frames. Lines represent linear fits to these data.

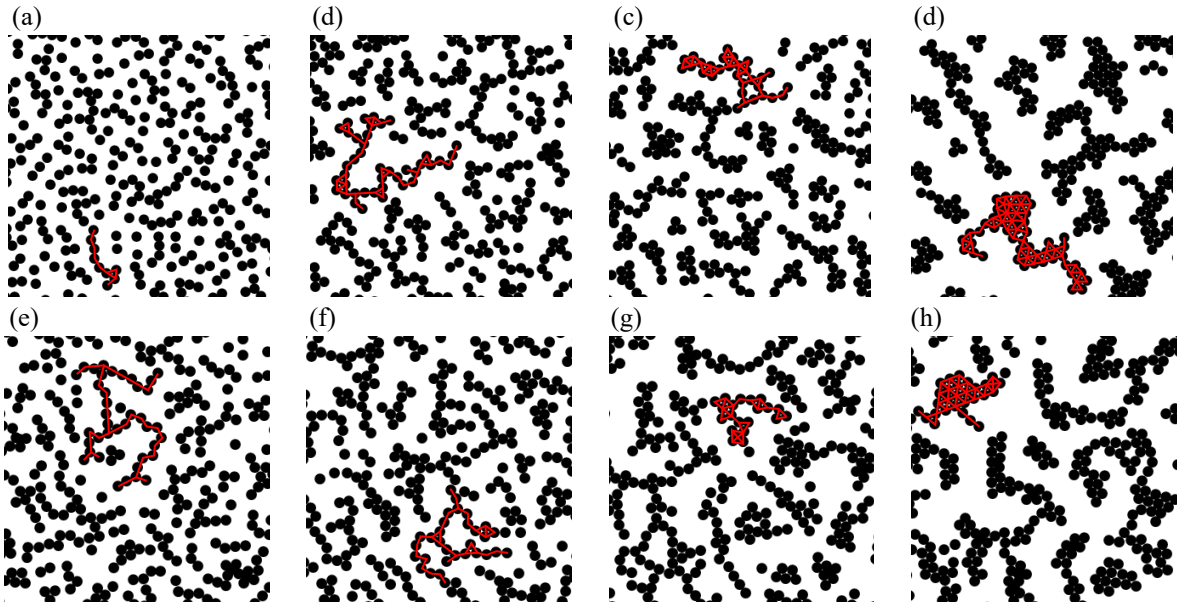


Figure 6.5: Snapshots of the cluster morphologies observed in P1 (top row) and P2 (bottom row) as a function of time from left to right. Red highlights emphasise the change from open clusters at early times to close packed structures at later times.

Cluster and network fractal dimensions

Next, we examine the fractal properties of each system by time dependent and time average methods. Plots (a) and (b) Figure 6.4 show the fractal dimension analysis results for systems

P1 and P2, respectively. The main plots show the fractal dimension for each frame determined using the methods described in Section 5.2.2. Experimental results are represented as open circles and red dashed lines are overlays of the mean D_f calculated using the data corresponding to the plateau regions at later times P1 and P2. As before (Section 5.4.2), D_f was found to vary as a function of time in both systems. However, the rate of change is shown to be more gradual in P2 than P1. At early times in both systems, it was found to be close to 1.45, but at later times a value of 1.6 was found.

The observed increase in fractal dimension in both systems appears to correspond to a shift in cluster morphologies from open chainlike structures at early times to compact close packed structures at later times. Figure 6.5 highlights these observations. The positions of individual particles are shown in black and example cluster morphologies, illustrating the change in cluster morphologies, are highlighted in red.

The average D_f for P1 over a time domain of 1200 - 7200 s was found to be 1.61. This represents an average taken over the time where the D_f remains constant. The same procedure was applied to the D_f results of P2. In this case, a time domain of 17500 - 28800 s was considered. A mean D_f of 1.58 was found. Although these measurements cannot be directly related to the growth exponents reported in Table 6.1, they do reflect the differences in cluster morphologies shown in Figure 6.2. In P1, clusters were more compact at later times, but in P2 they were more open at later times.

For completeness, we compare these results to those of the time averaged analysis shown in Figure 6.4 as insets. Here, we find a $D_f = 1.62$ and a $D_f = 1.54$ for P1 and P2, respectively. As expected, the time averaged results are in good agreement with time dependent results. However, the measured D_f of P2 was found to be smaller using the time averaged method than the results of P2 using the time dependent approach. This is attributed to the observed steady rise in D_f during P2's evolution.

6.3.2 Coordination number analysis

Figure 6.6 (a) and (b) show the coordination distributions for P1 and P2 respectively, as a function of time. The inset of plot (b) shows the CN distribution of P2 for the entire experiment. Both systems show a rapid decline in the number of particles with CN of 0 and 1, as expected

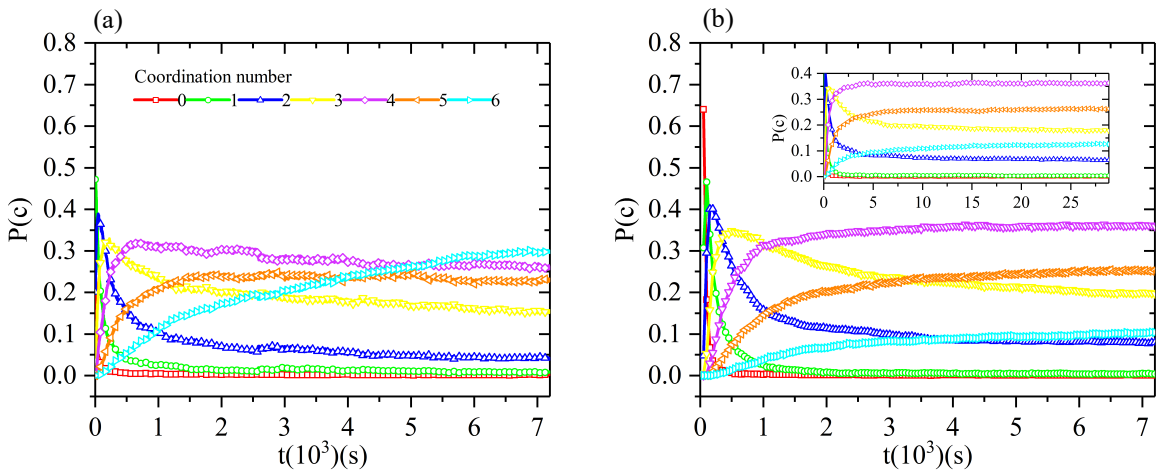


Figure 6.6: (a) and (b) show the coordination number distributions of P1 and P2 respectively, as a function of time. Plot (b) inset shows the CN distribution of P2 at long times.

for a densely packed system undergoing particle aggregation. However, differences between CN of 2 and 4 were apparent. In P1 the probability of finding a particle with a CN of 2 dropped to a $P(c) = 0.05$ at long times, lower than that of P2, which remained constant at $P(c) = 0.08$. Particles with a CN of 4 reduced as a function of time in P1, but increased in P2 and remained constant even at long times.

Finally, particles with a CN of 6 showed the most significant differences between both systems. In P1, a steady increase was observed for both short and long times, eventually becoming the CN with highest probability of occurring. However, in P2 the rate of change was smaller at early times and started to level off at approximately 3000 s, almost becoming constant at longer times. However, a small increase was evident at extreme long times shown in the inset of plot (b). These results suggest morphological differences between the clusters which initially form and the resulting networks.

The larger contribution of particles with a CN of 6 in P1 suggests denser clusters form, resulting in thicker strands at lower polymer concentrations. It also provides evidence that the lower polymer concentration system continues to evolve past the point at which percolation was first observed. In comparison, the CN distribution for the higher polymer concentration system (P2) indicates that once a space spanning network has formed, the system effectively arrests and the probability of further structural re-arrangement is greatly reduced. The lower probability of finding a particle with a CN of 6, where $P(c) = 0.1$ at later times, is evidence of significantly

thinner strand morphologies. This is in comparison to P1 where a CN of 6 has a $P(c) = 0.3$ at later times.

6.3.3 Bond-order orientational cluster analysis

By studying the argument of bond-order orientational parameter, $\theta_6(\vec{r}_j, t)$ (Equation 6.2), further insight into the aggregation behaviour and structural evolution of P1 and P2 can be found. Here, we investigate single particle and cluster rearrangements as a function of time. Initially, a global measurement of mean standard deviation of $\theta_6(\vec{r}_j, t)$ is considered for both systems. Subsequently, the same approach is performed on a single cluster by studying the time dependence of the standard deviation of $\theta_6(\vec{r}_j, t)$.

Global analysis

First, image analysis results using the custom algorithm referred to in Section 6.2.3 are shown. Figure 6.7 (a) - (f) shows the evolution of P1 as a function of time at intervals of 1, 10, 100, 1000, 2000, 7200 s respectively. Individual particles are coloured in by their $\theta_6(\vec{r}_j, t)$ value according to the legend shown in Figure 6.7. The coloured shadows surrounding groups of particles signify the cluster to which they belong. The colours of these clusters are randomly assigned and are only used to differentiate between the different clusters identified by the image analysis algorithm. Particles with a coordination number of 0 are coloured in black, as these do not contribute the $\theta_6(\vec{r}_j, t)$ distributions calculated for each system. Figure 6.7 shows the formation of chains at early times (a). As the system evolves, these aggregate, forming predominately single chain branched structures (b). However, at later times (c) these structures change into close packed, dense clusters (d - e) which ultimately aggregate together, forming large clusters and subsequently thick strands of the final network (f). As expected, the distribution of $\theta_6(\vec{r}_j, t)$ at early and late times seems to be random and evenly distributed across the FOV. A similar pattern is seen in P2, Figure 6.8 (a) - (f), as a function of time. However, the clusters formed at later times (d - e) seem to consist of fewer members and are more elongated, eventually forming a network consisting of thinner stands than those seen in P1. By inspection alone, it is difficult to determine noticeable differences between the distributions of $\theta_6(\vec{r}_j, t)$ at early and late times when compared to the observations made with respect to P1.

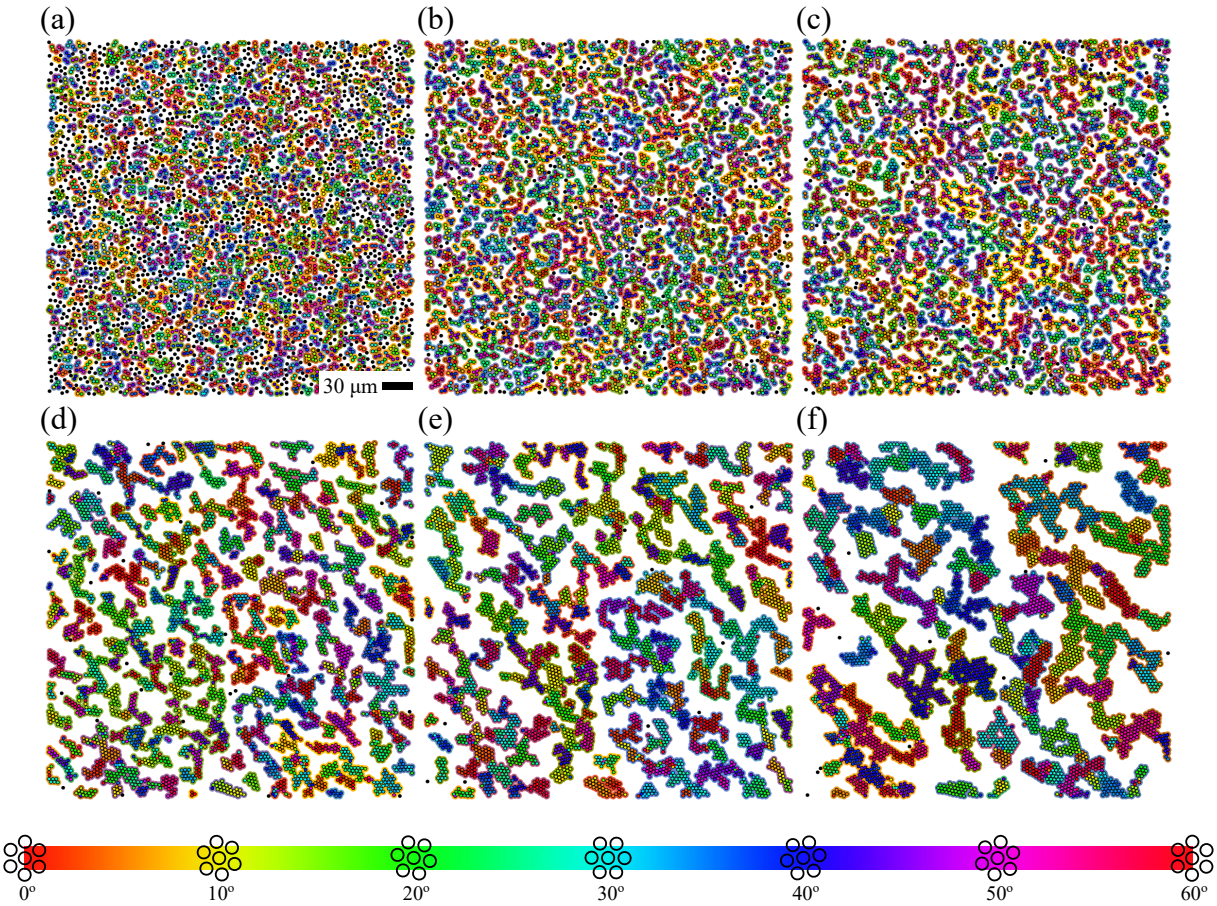


Figure 6.7: (a) - (f) shows cluster growth for P1 as a function of time. Images are taken at intervals of 1, 10, 100, 1000, 2000, and 7200 s respectively. Each particle is coloured according to its $\theta_6(\vec{r}_j, t)$ value. Individual clusters to which these particles belong are shown with shadows of differing colour.

From these data, the mean $\theta_6(\vec{r}_j, t)$ denoted $\langle\theta_{6cl}\rangle$, and the corresponding standard deviation denoted σ_{cl}, were calculated for each cluster. Figure 6.9 (a) and (b) show the number of clusters (blue line with triangle symbols) and the averaged standard deviation of $\theta_6(\vec{r}_j, t)$, for each cluster in the FOV, $\langle\sigma_{cl}\rangle$, (circles with solid red lines) as a function of time. This provides a global measure of order in the clusters and subsequent network. The cluster count in Figure 6.9 plot (a) shows the rapid formation of clusters in P1 at early times from $0 - 200$ s, until the rate of change in the number of clusters slowed dramatically from $200 - 7200$ s. Whilst the system did not completely arrest, a system spanning network was observed. This suggests a complete network, however weak, would have formed if the experimental time scale had been extended. Unfortunately, due to the gradual increase in cluster mass associated with cluster size, drift occurred in experiments which ran for longer times than those presented here. Therefore, these extreme long times have not been probed. Next, the cluster count is compared to

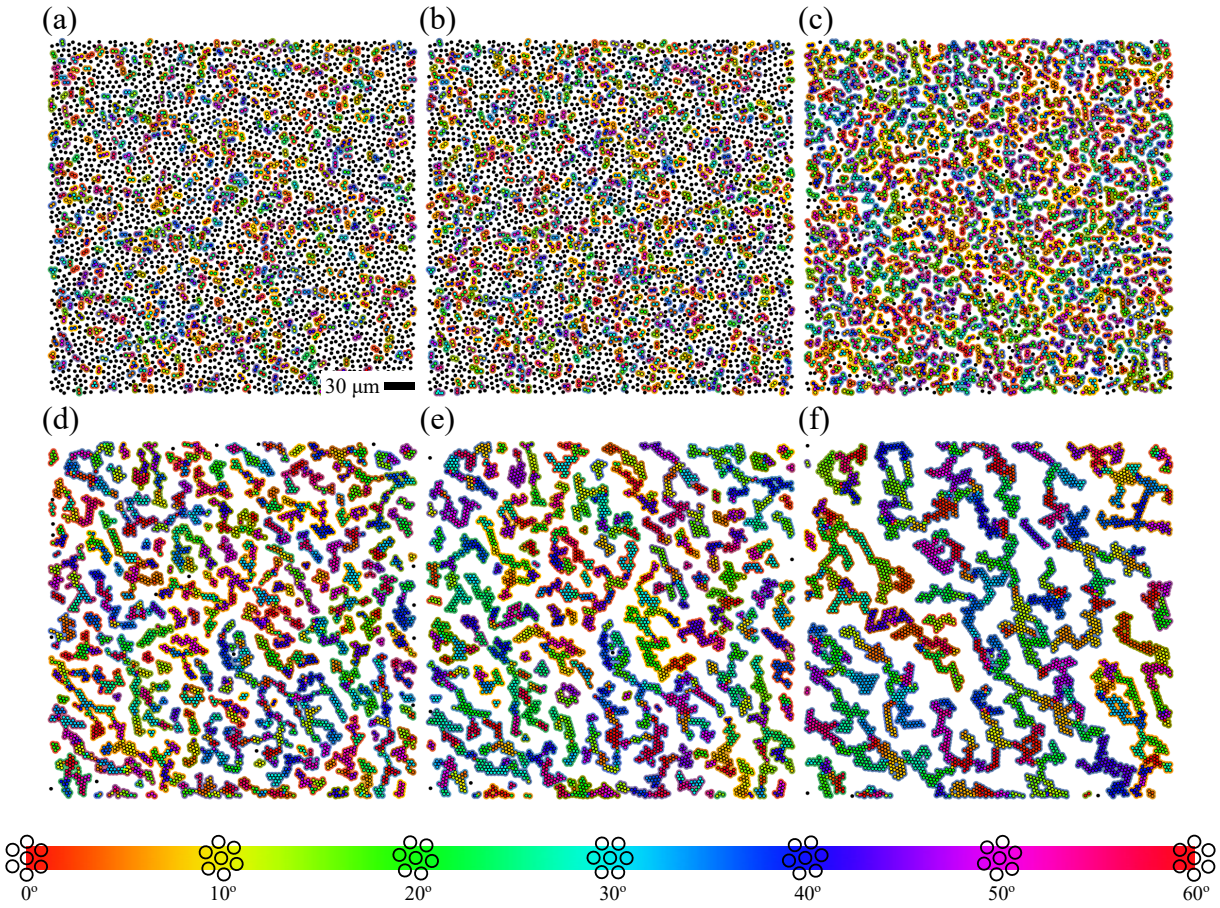


Figure 6.8: (a) - (f) shows cluster growth for P2 as a function of time. Images are taken at intervals of 1, 10, 100, 1000, 2000, and 28800 s respectively. Each particle is coloured according to its $\theta_6(\vec{r}_j, t)$ value. Individual clusters to which these particles belong are shown with shadows of differing colour. The colours of these clusters are randomly assigned and are only used to differentiate between the different clusters identified by the image analysis algorithm.

the $\langle \sigma_{cl} \rangle$ for P1 (Figure 6.9 (a)), as a function of time. A steady but shallow decrease in $\langle \sigma_{cl} \rangle$ was observed as the system evolved. These data indicate the rearrangement of particles within clusters as clusters aggregate, in order to maximise individual particle coordination numbers. This correlates with the results shown in Figure 6.6.

In the case of P2, Figure 6.9 (b), the same rapid formation of clusters at early times from 0 - 4000 s was observed. However, a second regime of slower growth appears to exist from 4000 - 20000 s. Finally, the system appears to completely arrest at 20000 s. In comparison to P1, the $\langle \sigma_{cl} \rangle$ of P2 increases as a function of time. In the case of P2, this is rationalised by the aggregation of fixed cluster geometries which do not rearrange as readily as those in P1 once new clusters have formed. This can be attributed to the increase in attractive interaction strength between particles. However, at late times the growth of $\langle \sigma_{cl} \rangle$ stops and a downward

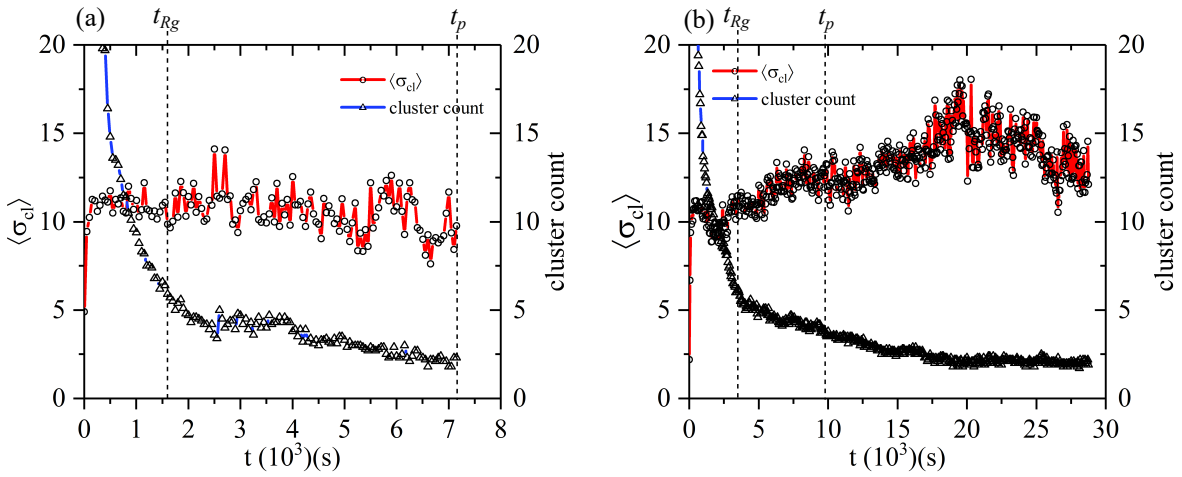


Figure 6.9: (a) and (b) show experimental results for P1 and P2 respectively. Open circles with solid red lines represent the mean standard deviation of θ_6 as a function of time. Open triangles with solid blue lines represents the number of clusters as a function of time. Cluster counts have been rescaled by a factor of 10^{-1}.

trend is once again observed. This coincides with the beginning of a constant region apparent in the cluster count, suggesting a global relaxation of the network once its formation has occurred.

The results from both systems suggest two competing processes are occurring in P1, which are absent in P2, at early times during the formation of clusters and the subsequent network. As clusters aggregate, $\langle\sigma_{cl}\rangle$ should increase, however rearrangements within the clusters cause it to decrease. However, the latter is to an extent masked by the former. This explains why the decease in $\langle\sigma_{cl}\rangle$ is not as pronounced as one would perhaps naively expect. To test this possibility further, the evolution of a single cluster in P1 was studied as a function of time.

Single cluster analysis

In order to confirm our findings, here we track and analysis the evolution of a single cluster taken from P1. The same analysis as before was applied, but with the effects of any cluster aggregation removed. Figure 6.10 (a) - (c) shows the evolution of a single cluster, selected from P1 starting at a time of 3400 s, as a function of time. A range of 2500 s was considered. The plots (d) - (f) show the corresponding $\theta_6(\vec{r}_j, t)$ distributions for each instant in time (a) - (c). From these data a change in the distribution of $\theta_6(\vec{r}_j, t)$ is apparent with a noticeable peak at $\theta_6(\vec{r}_j, t) = 60°$ appearing at late times (f). As the overall cluster orientation is the same, this

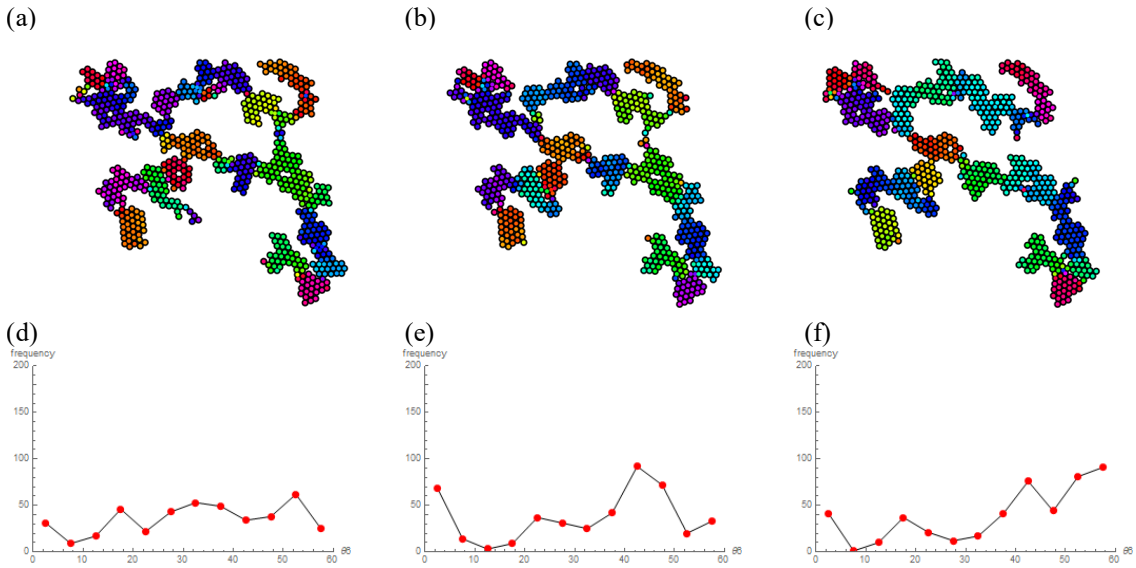


Figure 6.10: (a)(d), (b)(e) and (c)(f) shows the position of each particle in a single cluster coloured by its measured θ_6 value along with the corresponding histograms of θ_6 with bin widths 5° for a single cluster, tracked from P1 as a function of time.

suggests internal rearrangements of the cluster occur as a function of time. In order to provide a more robust measure of this observation, the change in σ_{cl} is plotted as a function of time Figure 6.11.

Figure 6.11 shows the change in σ_{cl} (red triangles and line) plotted with the cluster size (black circles and line), as a function of time. The cluster is tracked over a time period of 2500 s. Importantly, the cluster size remains constant over the length of time considered. The σ_{cl} for the selected cluster shows a steady decrease with time. This provides strong evidence that structural rearrangements, also present in P2 but appearing more pronounced in P1, are caused by the lower strength of interparticle attraction which results in more compact clusters that readily undergo conformational rearranges during and after network formation.

6.4 Conclusions

In conclusion, we have presented and characterised the growth of a novel 2D colloid-polymer system and the effects of interparticle interaction strength on cluster and network formation. The growth exponent for each system has been determined and shown to vary as a function of the system's evolution towards percolation. A time dependent relationship with regards to each

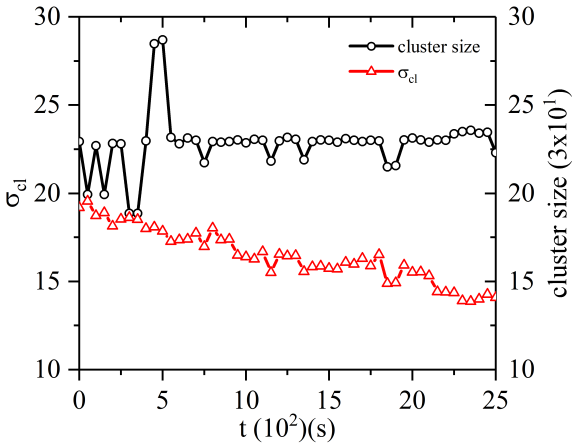


Figure 6.11: Plot showing the single cluster size (black circles and line) and change in σ_{cl} (red triangles and line) as a function of time.

system's fractal dimension has been found. Both ensemble average and time averaged approaches showed good agreement. Coordination number analysis showed an almost complete arrest of the network structure and minimal rearrangements once percolation was reached in the case of the higher polymer concentration system. However, the coordination number distributions of the lower polymer concentration system showed evidence of strand coarsening, with a continued increase in the number of particles with a coordination number of 6. This coarsening behaviour was investigated further by measuring the mean standard deviation of $\theta_6(\vec{r}_j, t)$ as a function of time, both globally and at a single cluster level. It has been shown that continued cluster and structural rearrangements occurred in the lower polymer concentration system, which were absent in the higher polymer concentration system, during network formation. Finally, this work suggests that a change in interparticle interaction strength has a significant effect on the growth, formation and structural evolution of the 2D colloid-polymer systems presented here. This system has the potential to be further developed and affords interesting opportunities to evaluate the effects of further changes to the overall system, for example the addition of larger particles at differing ratios.

Bibliography

[1] Simcha Lev-Yadun, Avi Gopher, and Shahal Abbo. The cradle of agriculture. *Science*, 288(5471):1602–1603, 2000.

[2] Alfred W Crosby. *The Columbian exchange: biological and cultural consequences of 1492*, volume 2. Greenwood Publishing Group, 2003.

[3] Keith Griffin. *The political economy of agrarian change: An essay on the Green Revolution*. Springer, 1979.

[4] Robert E Evenson and Douglas Gollin. Assessing the impact of the green revolution, 1960 to 2000. *science*, 300(5620):758–762, 2003.

[5] Prabhu L Pingali. Green revolution: impacts, limits, and the path ahead. *Proceedings of the National Academy of Sciences*, 109(31):12302–12308, 2012.

[6] Norman Ernest Borlaug. *Wheat breeding and its impact on world food supply*. CIMMYT, 1968.

[7] Norman E Borlaug. Contributions of conventional plant breeding to food production. *Science*, 219(4585):689–693, 1983.

[8] Vaclav Smil. *Enriching the earth: Fritz Haber, Carl Bosch, and the transformation of world food production*. MIT press, 2004.

[9] Lester R Brown. Nobel peace prize: developer of high-yield wheat receives award. *Science*, 170(3957):518–519, 1970.

[10] United States Environmental Protection Agency. MS Windows 10 kernel description, 2018.

[11] E-C Oerke and H-W Dehne. Safeguarding production—losses in major crops and the role of crop protection. *Crop protection*, 23(4):275–285, 2004.

[12] E-C Oerke. Crop losses to pests. *The Journal of Agricultural Science*, 144(1):31–43, 2006.

[13] Tomek De Ponti, Bert Rijk, and Martin K Van Ittersum. The crop yield gap between organic and conventional agriculture. *Agricultural systems*, 108:1–9, 2012.

[14] Laure Hossard, A Philibert, Michel Bertrand, Caroline Colnenne-David, Philippe Debaeke, N Munier-Jolain, Marie-Helene Jeuffroy, Guy Richard, and David Makowski. Effects of halving pesticide use on wheat production. *Scientific reports*, 4:4405, 2014.

[15] József Popp, Károly Pető, and János Nagy. Pesticide productivity and food security. a review. *Agronomy for sustainable development*, 33(1):243–255, 2013.

[16] D Fennell Evans and Håkan Wennerström. The colloidal domain: where physics, chemistry, biology, and technology meet. 1999.

[17] Malcolm A Faers, Tahsin H Choudhury, Bobby Lau, Kevin McAllister, and Paul F Luckham. Syneresis and rheology of weak colloidal particle gels. *Colloids and Surfaces A: Physicochemical and Engineering Aspects*, 288(1-3):170–179, 2006.

[18] Barbara Katzbauer. Properties and applications of xanthan gum. *Polymer degradation and Stability*, 59(1-3):81–84, 1998.

[19] F Garcıa-Ochoa, VE Santos, JA Casas, and E Gomez. Xanthan gum: production, recovery, and properties. *Biotechnology advances*, 18(7):549–579, 2000.

[20] George R Sanderson. Applications of xanthan gum. *British polymer journal*, 13(2):71–75, 1981.

[21] R Buscall, JW Goodwin, RH Ottewill, and Th F Tadros. The settling of particles through newtonian and non-newtonian media. *Journal of Colloid and Interface Science*, 85(1):78–86, 1982.

[22] Alberto Fernandez-Nieves, Hans Wyss, Johan Mattsson, and David A Weitz. *Microgel suspensions: fundamentals and applications*. John Wiley & Sons, 2011.

[23] Dipjyoti Saha and Suvendu Bhattacharya. Hydrocolloids as thickening and gelling agents in food: a critical review. *Journal of food science and technology*, 47(6):587–597, 2010.

[24] JO Carnali. A dispersed anisotropic phase as the origin of the weak-gel properties of aqueous xanthan gum. *Journal of Applied Polymer Science*, 43(5):929–941, 1991.

[25] SB Ross-Murphy and KP Shatwell. Polysaccharide strong and weak gels. *Biorheology*, 30(3-4):217–227, 1993.

[26] Elke Arendt and Fabio Dal Bello. *Gluten-free cereal products and beverages*. Elsevier, 2011.

[27] Henk NW Lekkerkerker and Remco Tuinier. *Colloids and the depletion interaction*, volume 833. Springer, 2011.

[28] William Bailey Russel, WB Russel, Dudley A Saville, and William Raymond Schowalter. *Colloidal dispersions*. Cambridge university press, 1991.

[29] Albert Einstein. Über die von der molekularkinetischen theorie der wärme geforderte bewegung von in ruhenden flüssigkeiten suspendierten teilchen. *Annalen der physik*, 322(8):549–560, 1905.

[30] Jean Perrin. Mouvement brownien et réalité moléculaire. In *Annales de Chimie et de Physique*, volume 18, pages 5–104, 1909.

[31] Patrick M Johnson, Carlos M van Kats, and Alfons van Blaaderen. Synthesis of colloidal silica dumbbells. *Langmuir*, 21(24):11510–11517, 2005.

[32] Youshen Wu, Yan Li, Lei Qin, Feilong Yang, and Daocheng Wu. Monodispersed or narrow-dispersed melamine–formaldehyde resin polymer colloidal spheres: preparation, size-control, modification, bioconjugation and particle formation mechanism. *Journal of materials chemistry B*, 1(2):204–212, 2013.

[33] Bo Peng, Ernest van der Wee, Arnout Imhof, and Alfons van Blaaderen. Synthesis of monodisperse, highly cross-linked, fluorescent pmma particles by dispersion polymerization. *Langmuir*, 28(17):6776–6785, 2012.

[34] Werner Stöber, Arthur Fink, and Ernst Bohn. Controlled growth of monodisperse silica spheres in the micron size range. *Journal of colloid and interface science*, 26(1):62–69, 1968.

[35] Tadao Sugimoto, Mohammad M Khan, and Atsushi Muramatsu. Preparation of monodisperse peanut-type α-fe2o3 particles from condensed ferric hydroxide gel. *Colloids and Surfaces A: Physicochemical and Engineering Aspects*, 70(2):167–169, 1993.

[36] Yong Wang, Xiaowen Su, Panshuang Ding, Shan Lu, and Huaping Yu. Shape-controlled synthesis of hollow silica colloids. *Langmuir*, 29(37):11575–11581, 2013.

[37] Laura Rossi, Stefano Sacanna, William TM Irvine, Paul M Chaikin, David J Pine, and Albert P Philipse. Cubic crystals from cubic colloids. *Soft Matter*, 7(9):4139–4142, 2011.

[38] Anke Kuijk, Alfons van Blaaderen, and Arnout Imhof. Synthesis of monodisperse, rodlike silica colloids with tunable aspect ratio. *Journal of the American Chemical Society*, 133(8):2346–2349, 2011.

[39] Stefano Sacanna, WTM Irvine, Paul M Chaikin, and David J Pine. Lock and key colloids. *Nature*, 464(7288):575, 2010.

[40] Amar B Pawar and Ilona Kretzschmar. Fabrication, assembly, and application of patchy particles. *Macromolecular rapid communications*, 31(2):150–168, 2010.

[41] Qian Chen, Sung Chul Bae, and Steve Granick. Directed self-assembly of a colloidal kagome lattice. *Nature*, 469(7330):381, 2011.

[42] Sharon C Glotzer and Michael J Solomon. Anisotropy of building blocks and their assembly into complex structures. *Nature materials*, 6(8):557, 2007.

[43] Arthur Ashkin. Forces of a single-beam gradient laser trap on a dielectric sphere in the ray optics regime. *Biophysical journal*, 61(2):569–582, 1992.

[44] John P McTague. Magnetoviscosity of magnetic colloids. *The Journal of Chemical Physics*, 51(1):133–136, 1969.

[45] Edward Allen Peterson and David Allen Krueger. Reversible, field induced agglomeration in magnetic colloids. *Journal of Colloid and Interface Science*, 62(1):24–34, 1977.

[46] Jianping Ge, Yongxing Hu, Maurizio Biasini, Ward P Beyermann, and Yadong Yin. Superparamagnetic magnetite colloidal nanocrystal clusters. *Angewandte Chemie International Edition*, 46(23):4342–4345, 2007.

[47] Colin P Reynolds, Kira E Klop, François A Lavergne, Sarah M Morrow, Dirk GAL Aarts, and Roel PA Dullens. Deterministic aggregation kinetics of superparamagnetic colloidal particles. *The Journal of chemical physics*, 143(21):214903, 2015.

[48] Emanuela Zaccarelli. Colloidal gels: equilibrium and non-equilibrium routes. *Journal of Physics: Condensed Matter*, 19(32):323101, 2007.

[49] Peter J Lu and David A Weitz. Colloidal particles: crystals, glasses, and gels. *Annu. Rev. Condens. Matter Phys.*, 4(1):217–233, 2013.

[50] Joseph R Samaniuk and Jan Vermant. Micro and macrorheology at fluid–fluid interfaces. *Soft matter*, 10(36):7023–7033, 2014.

[51] David F Williams and John C Berg. The aggregation of colloidal particles at the air—water interface. *Journal of colloid and interface science*, 152(1):218–229, 1992.

[52] Sven Reynaert, Paula Moldenaers, and Jan Vermant. Control over colloidal aggregation in monolayers of latex particles at the oil- water interface. *Langmuir*, 22(11):4936–4945, 2006.

[53] Ryan McGorty, Jerome Fung, David Kaz, and Vinothan N Manoharan. Colloidal self-assembly at an interface. *Materials Today*, 13(6):34–42, 2010.

[54] Eric R Weeks. Soft jammed materials. *Statistical physics of complex fluids, Eds S Maruyama, M Tokuyama, pag*, 2(1):87, 2007.

[55] B. V. Derjaguin, L. Landau, et al. Theory of the stability of strongly charged lyophobic sols and of the adhesion of strongly charged particles in solutions of electrolytes. *Acta Physicochimica URSS*, 14(6):633–662, 1941.

[56] E. J. W. Verwey. Theory of the stability of lyophobic colloids. *The Journal of Physical and Colloid Chemistry*, 51(3):631–636, 1947.

[57] J. N. Israelachvili. *Intermolecular and surface forces: revised third edition*. Academic press, 2011.

[58] D. Evans and H. Wennerstrom. *The colloidal domain*. Wiley-Vch, 1999.

[59] David Jeffrey Griffiths. Reed college, introduction to electrodynamics, vol. 3, 1999.

[60] Erhard W Fischer. Elektronenmikroskopische untersuchungen zur stabilität von suspensionen in makromolekularen lösungen. *Colloid & Polymer Science*, 160(2):120–141, 1958.

[61] Sho Asakura and Fumio Oosawa. Interaction between particles suspended in solutions of macromolecules. *Journal of Polymer Science Part A: Polymer Chemistry*, 33(126):183–192, 1958.

[62] A Vrij. Polymers at interfaces and the interactions in colloidal dispersions. *Pure and Applied Chemistry*, 48(4):471–483, 1976.

[63] FKR Li-In-On, B Vincent, and FA Waite. Stability of sterically stabilized dispersions at high polymer concentrations. ACS Publications, 1975.

[64] Lang Feng, Bezia Laderman, Stefano Sacanna, and Paul Chaikin. Re-entrant solidification in polymer–colloid mixtures as a consequence of competing entropic and enthalpic attractions. *Nature materials*, 14(1):61–65, 2015.

[65] Alice L Thorneywork, Joshua L Abbott, Dirk GAL Aarts, and Roel PA Dullens. Two-dimensional melting of colloidal hard spheres. *Physical Review Letters*, 118(15):158001, 2017.

[66] Wilson Poon. Colloids as big atoms. *Science*, 304(5672):830–831, 2004.

[67] Geir Fonnum, Christer Johansson, Astrid Molteberg, Steen Mørup, and Elin Aksnes. Characterisation of dynabeads® by magnetization measurements and mössbauer spectroscopy. *Journal of Magnetism and Magnetic Materials*, 293(1):41–47, 2005.

[68] A. Ashkin. Acceleration and trapping of particles by radiation pressure. *Physical Review Letters*, 24:156–159, 1970.

[69] A. Ashkin. Forces of a single-beam gradient laser trap on a dielectric sphere in the ray optics regime. *Biophysical Journal*, 61(2):569, 1992.

[70] Arlene A Teraoka and Iwao Teraoka. *Polymer solutions: an introduction to physical properties*. John Wiley & Sons, 2002.

[71] Syed KH Gulrez, Saphwan Al-Assaf, Yapeng Fang, Glyn O Phillips, and A Patrick Gunning. Revisiting the conformation of xanthan and the effect of industrially relevant treatments. *Carbohydrate polymers*, 90(3):1235–1243, 2012.

[72] Cristina-Eliza Brunchi, Simona Morariu, and Maria Bercea. Intrinsic viscosity and conformational parameters of xanthan in aqueous solutions: salt addition effect. *Colloids and Surfaces B: Biointerfaces*, 122:512–519, 2014.

[73] Jeffrey G Southwick, Hoosung Lee, Alexander M Jamieson, and John Blackwell. Self-association of xanthan in aqueous solvent-systems. *Carbohydrate Research*, 84(2):287–295, 1980.

[74] Terri A Camesano and Kevin J Wilkinson. Single molecule study of xanthan conformation using atomic force microscopy. *Biomacromolecules*, 2(4):1184–1191, 2001.

[75] HA Khouryieh, TJ Herald, F Aramouni, and S Alavi. Influence of mixing temperature on xanthan conformation and interaction of xanthan–guar gum in dilute aqueous solutions. *Food Research International*, 39(9):964–973, 2006.

[76] Michel Milas, Wayne F Reed, and Sylvain Printz. Conformations and flexibility of native and re-natured xanthan in aqueous solutions. *International Journal of Biological Macromolecules*, 18(3):211–221, 1996.

[77] Nicholas B Wyatt and Matthew W Liberatore. Rheology and viscosity scaling of the polyelectrolyte xanthan gum. *Journal of Applied Polymer Science*, 114(6):4076–4084, 2009.

[78] Howard A Barnes, John Fletcher Hutton, and Kenneth Walters. *An introduction to rheology*. Elsevier, 1989.

[79] Michael Rubinstein and Ralph H Colby. *Polymer physics*, volume 23. Oxford University Press New York, 2003.

[80] Michael T Johnston and Randy H Ewoldt. Precision rheometry: Surface tension effects on low-torque measurements in rotational rheometers. *Journal of Rheology*, 57(6):1515–1532, 2013.

[81] Eric M Furst and Todd M Squires. *Microrheology*. Oxford University Press, 2017.

[82] Bernhard A Wolf. Polyelectrolytes revisited: reliable determination of intrinsic viscosities. *Macromolecular rapid communications*, 28(2):164–170, 2007.

[83] Maurice L Huggins. The viscosity of dilute solutions of long-chain molecules. iv. dependence on concentration. *Journal of the American Chemical Society*, 64(11):2716–2718, 1942.

[84] Thomas G Fox Jr and Paul J Flory. Second-order transition temperatures and related properties of polystyrene. i. influence of molecular weight. *Journal of Applied Physics*, 21(6):581–591, 1950.

[85] H Mark. der feste korper. *Hirzel, Leipzig*, 103, 1938.

[86] Roelof Houwink. Zusammenhang zwischen viscosimetrisch und osmotisch bestimmten polymerisationsgraden bei hochpolymeren. *Journal für praktische Chemie*, 157(1-3):15–18, 1940.

[87] Minmin Tian and Petr Munk. Characterization of polymer-solvent interactions and their temperature dependence using inverse gas chromatography. *Journal of Chemical and Engineering Data*, 39(4):742–755, 1994.

[88] Tai-Hsi Fan, Bin Xie, and Remco Tuinier. Asymptotic analysis of tracer diffusivity in nonadsorbing polymer solutions. *Physical Review E*, 76(5):051405, 2007.

[89] Gijsberta H Koenderink, Stefano Sacanna, Dirk GAL Aarts, and AP Philipse. Rotational and translational diffusion of fluorocarbon tracer spheres in semidilute xanthan solutions. *Physical Review E*, 69(2):021804, 2004.

[90] R Tuinier, JKG Dhont, and T-H Fan. How depletion affects sphere motion through solutions containing macromolecules. *EPL (Europhysics Letters)*, 75(6):929, 2006.

[91] Ibrahim Sadek Khattab, Farzana Bandarkar, Mohammad Amin Abolghassemi Fakhree, and Abolghasem Jouyban. Density, viscosity, and surface tension of water+ ethanol mixtures from 293 to 323k. *Korean Journal of Chemical Engineering*, 29(6):812–817, 2012.

[92] Jonathan Leach, H Mushfique, S Keen, R Di Leonardo, G Ruocco, JM Cooper, and MJ Padgett. Comparison of faxén's correction for a microsphere translating or rotating near a surface. *Physical Review E*, 79(2):026301, 2009.

[93] Jacob N Israelachvili. *Intermolecular and surface forces*. Academic press, 2011.

[94] Hans-Jürgen Butt, Brunero Cappella, and Michael Kappl. Force measurements with the atomic force microscope: Technique, interpretation and applications. *Surface science reports*, 59(1-6):1–152, 2005.

[95] Dennis C Prieve. Measurement of colloidal forces with tirm. *Advances in Colloid and Interface Science*, 82(1-3):93–125, 1999.

[96] Hans-Hennig von Grünberg, Laurent Helden, Paul Leiderer, and Clemens Bechinger. Measurement of surface charge densities on brownian particles using total internal reflection microscopy. *The Journal of Chemical Physics*, 114(22):10094–10104, 2001.

[97] Eric M Furst. Interactions, structure, and microscopic response: complex fluid rheology using laser tweezers. *Soft Materials*, 1(2):167–185, 2003.

[98] David G Grier. Optical tweezers in colloid and interface science. *Feb*, 5:264–274, 1997.

[99] Justin E Molloy and Miles J Padgett. Lights, action: optical tweezers. *Contemporary physics*, 43(4):241–258, 2002.

[100] Dirk LJ Vossen, Astrid van der Horst, Marileen Dogterom, and Alfons van Blaaderen. Optical tweezers and confocal microscopy for simultaneous three-dimensional manipulation and imaging in concentrated colloidal dispersions. *Review of Scientific Instruments*, 75(9):2960–2970, 2004.

[101] Jörg Baumgartl and Clemens Bechinger. On the limits of digital video microscopy. *EPL (Europhysics Letters)*, 71(3):487, 2005.

[102] Jörg Baumgartl, Jose Luis Arauz-Lara, and Clemens Bechinger. Like-charge attraction in confinement: myth or truth? *Soft Matter*, 2(8):631–635, 2006.

[103] Yilong Han and David G Grier. Confinement-induced colloidal attractions in equilibrium. *Physical review letters*, 91(3):038302, 2003.

[104] Masao Doi. *Soft matter physics*. Oxford University Press, 2013.

[105] James Sethna. *Statistical mechanics: entropy, order parameters, and complexity*, volume 14. Oxford University Press, 2006.

[106] Nicolaas Godfried Van Kampen. *Stochastic processes in physics and chemistry*, volume 1. Elsevier, 1992.

[107] Lennart Sjogren. The kramers problem and first passage times.

[108] Michael PN Juniper, Rut Besseling, Dirk GAL Aarts, and Roel PA Dullens. Acousto-optically generated potential energy landscapes: Potential mapping using colloids under flow. *Optics express*, 20(27):28707–28716, 2012.

[109] Harun Yücel and Nazmi Turan Okumuşoğlu. A new tracking algorithm for multiple colloidal particles close to contact. *Journal of Physics: Condensed Matter*, 29(46):465101, 2017.

[110] Chi Zhang, Georges Brügger, and Frank Scheffold. Tracking of colloids close to contact. *Optics express*, 23(17):22579–22586, 2015.

[111] Ulrike Lohmann and Johann Feichter. Global indirect aerosol effects: a review. *Atmospheric Chemistry and Physics*, 5(3):715–737, 2005.

[112] William G Finnegan and Richard L Pitter. A postulate of electric multipoles in growing ice crystals: Their role in the formation of ice crystal aggregates. *Atmospheric research*, 22(3):235–250, 1988.

[113] Ulrike Lohmann, Peter Spichtinger, Stephanie Jess, Thomas Peter, and Herman Smit. Cirrus cloud formation and ice supersaturated regions in a global climate model. *Environmental research letters*, 3(4):045022, 2008.

[114] Christopher A Ross and Michelle A Poirier. Protein aggregation and neurodegenerative disease. *Nature medicine*, 10(7):S10, 2004.

[115] Edward H Koo, Peter T Lansbury, and Jeffery W Kelly. Amyloid diseases: abnormal protein aggregation in neurodegeneration. *Proceedings of the National Academy of Sciences*, 96(18):9989–9990, 1999.

[116] Jens Tyedmers, Axel Mogk, and Bernd Bukau. Cellular strategies for controlling protein aggregation. *Nature reviews Molecular cell biology*, 11(11):777, 2010.

[117] Ana R Prazeres, Fátima Carvalho, and Javier Rivas. Cheese whey management: A review. *Journal of environmental management*, 110:48–68, 2012.

[118] Alan L Kelly, Thom Huppertz, and Jeremiah J Sheehan. Pre-treatment of cheese milk: principles and developments. *Dairy Science and Technology*, 88(4-5):549–572, 2008.

[119] Mikhail Motornov, Roman Sheparovych, Robert Lupitskyy, Emily MacWilliams, and Sergiy Minko. Responsive colloidal systems: Reversible aggregation and fabrication of superhydrophobic surfaces. *Journal of colloid and interface science*, 310(2):481–488, 2007.

[120] Ravi Prasher, Patrick E Phelan, and Prajesh Bhattacharya. Effect of aggregation kinetics on the thermal conductivity of nanoscale colloidal solutions (nanofluid). *Nano letters*, 6(7):1529–1534, 2006.

[121] Jacques Buffle, Kevin J Wilkinson, Serge Stoll, Montserrat Filella, and Jingwu Zhang. A generalized description of aquatic colloidal interactions: the three-colloidal component approach. *Environmental Science & Technology*, 32(19):2887–2899, 1998.

[122] Valerie J Anderson and Henk NW Lekkerkerker. Insights into phase transition kinetics from colloid science. *Nature*, 416(6883):811–815, 2002.

[123] Anna Stradner, Helen Sedgwick, Frédéric Cardinaux, Wilson CK Poon, Stefan U Egelhaaf, and Peter Schurtenberger. Equilibrium cluster formation in concentrated protein solutions and colloids. *Nature*, 432(7016):492, 2004.

[124] Jie Zhang, Erik Luijten, and Steve Granick. Toward design rules of directional janus colloidal assembly. *Annual review of physical chemistry*, 66:581–600, 2015.

[125] Marina Carpineti and Marzio Giglio. Spinodal-type dynamics in fractal aggregation of colloidal clusters. *Physical review letters*, 68(22):3327, 1992.

[126] MY Lin, HM Lindsay, DA Weitz, RCBR Klein, RC Ball, and Paul Meakin. Universal diffusion-limited colloid aggregation. *Journal of Physics: Condensed Matter*, 2(13):3093, 1990.

[127] DA Weitz, JS Huang, MY Lin, and J Sung. Limits of the fractal dimension for irreversible kinetic aggregation of gold colloids. *Physical review letters*, 54(13):1416, 1985.

[128] MY Lin, H_M Lindsay, DA Weitz, RC Ball, R Klein, and P Meakin. Universality in colloid aggregation. *Nature*, 339(6223):360, 1989.

[129] Paul Meakin. Formation of fractal clusters and networks by irreversible diffusion-limited aggregation. *Physical Review Letters*, 51(13):1119, 1983.

[130] Paul Meakin. Diffusion-limited aggregation on two-dimensional percolation clusters. *Physical Review B*, 29(8):4327, 1984.

[131] M Kolb. Unified description of static and dynamic scaling for kinetic cluster formation. *Physical review letters*, 53(17):1653, 1984.

[132] Rebecca W Perry, Miranda C Holmes-Cerfon, Michael P Brenner, and Vinothan N Manoharan. Two-dimensional clusters of colloidal spheres: ground states, excited states, and structural rearrangements. *Physical review letters*, 114(22):228301, 2015.

[133] M Von Smoluchowski. Mv smoluchowski, phys. z. 17, 557 (1916). *Phys. Z.*, 17:557, 1916.

[134] Joanne HE Promislow, Alice P Gast, and Marc Fermigier. Aggregation kinetics of paramagnetic colloidal particles. *The Journal of chemical physics*, 102(13):5492–5498, 1995.

[135] Tamás Vicsek and Fereydoon Family. Dynamic scaling for aggregation of clusters. *Physical Review Letters*, 52(19):1669, 1984.

[136] A Moncho-Jordá, G Odriozola, F Martınez-López, A Schmitt, and R Hidalgo-Álvarez. The dlca-rlca transition arising in 2d-aggregation: simulations and mean field theory. *The European Physical Journal E*, 5(4):471–480, 2001.

[137] Ofer Malcai, Daniel A Lidar, Ofer Biham, and David Avnir. Scaling range and cutoffs in empirical fractals. *Physical Review E*, 56(3):2817, 1997.

[138] TA Witten Jr and Leonard M Sander. Diffusion-limited aggregation, a kinetic critical phenomenon. *Physical review letters*, 47(19):1400, 1981.

[139] Colin P Reynolds, David Robinson, Dirk GAL Aarts, Mark Wilson, William W Sampson, and Roel PA Dullens. Coordination number statistics of cluster formation. *EPL (Europhysics Letters)*, 116(2):28001, 2016.

[140] Fei Wang, Zhaomin Li, Hailong Chen, and Xibin Zhang. Establishment and application of a structure evolution model for aqueous foam based on fractal theory. *RSC Advances*, 7(7):3650–3659, 2017.

[141] JE Martin and D Adolf. The sol-gel transition in chemical gels. *Annual review of physical chemistry*, 42(1):311–339, 1991.

[142] VERONIQUE Trappe, V Prasad, Luca Cipelletti, PN Segre, and DAVID A Weitz. Jamming phase diagram for attractive particles. *Nature*, 411(6839):772, 2001.

[143] Suliana Manley, JM Skotheim, L Mahadevan, and DAVID A Weitz. Gravitational collapse of colloidal gels. *Physical review letters*, 94(21):218302, 2005.

[144] CK Wilson et al. Gelation in colloid–polymer mixtures. *Faraday Discussions*, 101:65–76, 1995.

[145] Michael C Jarvis. Structure and properties of pectin gels in plant cell walls. *Plant, Cell & Environment*, 7(3):153–164, 1984.

[146] Gerald F Elliott and Stuart A Hodson. Cornea, and the swelling of polyelectrolyte gels of biological interest. *Reports on Progress in Physics*, 61(10):1325, 1998.

[147] Enrica Caló and Vitaliy V Khutoryanskiy. Biomedical applications of hydrogels: A review of patents and commercial products. *European Polymer Journal*, 65:252–267, 2015.

[148] Huiling Jiang, Victor Pan, Skanda Vivek, Eric R Weeks, and Yonggang Ke. Programmable dna hydrogels assembled from multidomain dna strands. *ChemBioChem*, 17(12):1156–1162, 2016.

[149] Qun Wang, Limin Wang, Michael S Detamore, and Cory Berkland. Biodegradable colloidal gels as moldable tissue engineering scaffolds. *Advanced Materials*, 20(2):236–239, 2008.

[150] Veronique Trappe and Peter Sandkühler. Colloidal gels—low-density disordered solid-like states. *Current opinion in colloid & interface science*, 8(6):494–500, 2004.

[151] Peter J Lu, Emanuela Zaccarelli, Fabio Ciulla, Andrew B Schofield, Francesco Sciortino, and David A Weitz. Gelation of particles with short-range attraction. *Nature*, 453(7194):499, 2008.

[152] K Kroy, ME Cates, and WCK Poon. Cluster mode-coupling approach to weak gelation in attractive colloids. *Physical review letters*, 92(14):148302, 2004.

[153] Wilson CK Poon and MD Haw. Mesoscopic structure formation in colloidal aggregation and gelation. *Advances in Colloid and Interface Science*, 73:71–126, 1997.

[154] Hugo Bissig, Sara Romer, Luca Cipelletti, Veronique Trappe, and Peter Schurtenberger. Intermittent dynamics and hyper-aging in dense colloidal gels. *PhysChemComm*, 6(5):21–23, 2003.

[155] Peter Mayer, Hugo Bissig, Ludovic Berthier, Luca Cipelletti, Juan P Garrahan, Peter Sollich, and Véronique Trappe. Heterogeneous dynamics of coarsening systems. *Physical review letters*, 93(11):115701, 2004.

[156] Luca Cipelletti, Suliana Manley, RC Ball, and DA Weitz. Universal aging features in the restructuring of fractal colloidal gels. *Physical review letters*, 84(10):2275, 2000.

[157] Laura Starrs, WCK Poon, DJ Hibberd, and MM Robins. Collapse of transient gels in colloid-polymer mixtures. *Journal of Physics: Condensed Matter*, 14(10):2485, 2002.

[158] Paul Bartlett, Lisa J Teece, and Malcolm A Faers. Sudden collapse of a colloidal gel. *Physical Review E*, 85(2):021404, 2012.

[159] PN Pusey, AD Pirie, and WCK Poon. Dynamics of colloid-polymer mixtures. *Physica A: Statistical Mechanics and its Applications*, 201(1-3):322–331, 1993.

[160] JC Conrad, HM Wyss, Véronique Trappe, Suliana Manley, K Miyazaki, LJ Kaufman, AB Schofield, DR Reichman, and DA Weitz. Arrested fluid-fluid phase separation in

depletion systems: Implications of the characteristic length on gel formation and rheology. *Journal of Rheology*, 54(2):421–438, 2010.

[161] Thomas Gisler, Robin C Ball, and David A Weitz. Strain hardening of fractal colloidal gels. *Physical review letters*, 82(5):1064, 1999.

[162] AD Dinsmore and DA Weitz. Direct imaging of three-dimensional structure and topology of colloidal gels. *Journal of Physics: Condensed Matter*, 14(33):7581, 2002.

[163] Nynke AM Verhaegh, Daniela Asnaghi, and Henk NW Lekkerkerker. Transient gels in colloid–polymer mixtures studied with fluorescence confocal scanning laser microscopy. *Physica A: Statistical Mechanics and its Applications*, 264(1-2):64–74, 1999.

[164] DJ Robinson and JC Earnshaw. Experimental study of colloidal aggregation in two dimensions. i. structural aspects. *Physical Review A*, 46(4):2045, 1992.

[165] DJ Robinson and JC Earnshaw. Experimental study of colloidal aggregation in two dimensions. ii. kinetic aspects. *Physical Review A*, 46(4):2055, 1992.

[166] DJ Robinson and JC Earnshaw. Experimental study of colloidal aggregation in two dimensions. iii. structural dynamics. *Physical Review A*, 46(4):2065, 1992.

[167] H Hoekstra, Jan Vermant, Joannes Mewis, and GG Fuller. Flow-induced anisotropy and reversible aggregation in two-dimensional suspensions. *Langmuir*, 19(22):9134–9141, 2003.

[168] Sven Reynaert, Paula Moldenaers, and Jan Vermant. Interfacial rheology of stable and weakly aggregated two-dimensional suspensions. *Physical Chemistry Chemical Physics*, 9(48):6463–6475, 2007.

[169] Kasper Masschaele, Jan Fransaer, and Jan Vermant. Flow-induced structure in colloidal gels: Direct visualization of model 2d suspensions. *Soft Matter*, 7(17):7717–7726, 2011.

[170] Kasper Masschaele, Jan Fransaer, and Jan Vermant. Direct visualization of yielding in model two-dimensional colloidal gels subjected to shear flow. *Journal of rheology*, 53(6):1437–1460, 2009.

[171] David R Nelson. *Defects and geometry in condensed matter physics*. Cambridge University Press, 2002.

Acknowledgements

First, I would like to thank my supervisors Dirk and Roel for their unwavering guidance and support. Second, our industrial sponsors for their keen interest and endless enthusiasm towards our research. It has been a pleasure to work with you. I would also like to thank every member of the Oxford Colloid Group, past and present. The group contains, without a doubt, some of the smartest people I have been fortunate enough to work alongside. I hope you all go on to do fulfilling and interesting things with your time. A special thanks to my partner. You are undoubtedly one of the most ethically sound, intelligent and passionate people I know. Without your devotion and support, this would not have been possible. What is more impressive, you managed all this whilst simultaneously excelling at your own challenges and pursuits. As always, I would like to thank my family for being the good people that they are. Knowing you are there makes these adventures possible and without you they are most definitely not. I am lucky enough to have parents who never give up on protecting and supporting their young, and for that, I am eternally grateful. Importantly, thank you friends, near and far, for always being there in times of need, even if after initial consolation, ridicule and sharp wit is never far behind. I cherish and love every one of you and would expect nothing less from you all. You are a truly wonderful bunch of people that the world would be far more dull without. And finally, when I first started this journey, I had an innate passion for science and total bewilderment at the seemingly boundless achievements of human endeavour. This experience has done nothing less than authenticate and magnify that cogitation. Only now do I appreciated the shear breadth and depth of the knowledge we have gained as a species and how little each one of us as an individual knows. This knowledge is more precious than time itself. At the time of writing, this country is at a precipice. As individuals we are inherently limited, but as a collective, we are most certainly not and the work you are all engaged in provides the evidence thereof. Be kind, be supportive and be open with one another. To quote Dr. K. Edmond who I think sums up how we all feel from time to time “I’m confused”.